

Operability of WTG Blade Installation on a Semi-submersible FOWT

Master Thesis
Menno Hoogeslag

Delft University of Technology



Norwegian University of
Science and Technology



Operability of WTG Blade Installation on a Semi-submersible FOWT

by

Menno Hoogeslag

Student Name	Student Number
Menno Hoogeslag	4955013 (TU Delft) 103221 (NTNU)

Thesis committee:	Ir. J.S. Hoving, Dr. Ir. B.C. Ummels, Prof. M. Greco, Ir. R. de Bruijn, January, 2024 - August, 2024	chairman supervisor TU Delft supervisor NTNU supervisor GustoMSC
Faculty:	Civil Engineering and Geosciences, Delft Department of Marine Technology, Trondheim	

Cover: Render of floating wind turbine installation site with GustoMSC
Tri-Floaters and quayside crane, by GustoMSC.

Preface

The thesis that will be presented in this report is part of the European Wind Energy Master (EWEM). It is the final report to obtain a Delft University of Technology (TU Delft) degree in Offshore and Dredging Engineering, and a Norwegian University of Science and Technology (NTNU) degree in Technology - Wind Energy. This thesis' subject was proposed by GustoMSC, to investigate how a wind turbine could be installed on the Tri-Floater, and what the operability of such an installation is. This thesis is written in cooperation with GustoMSC.

The proposed research was aimed at floating wind energy, a subject that I found really interesting, immediately. The development of this technology and the large growth of the offshore wind energy sector appeal to me. Currently, there are only a few floating wind turbines in operation, which shows that there is enough room for improvement. As more and more floating wind turbines are expected to become operational in the future, the installation of these turbines plays a crucial role. The concept that is presented in this thesis, where a large quayside crane will be used to perform the installation, is a promising strategy. The wind and wave conditions are generally calmer in a harbour than at an offshore site, so this could be beneficial over installing turbines offshore. It would be interesting if and how this strategy will be deployed in the future.

I would like to thank all my supervisors for helping, supporting, advising, and believing in me throughout my whole thesis. Marilena Greco from NTNU, thank you for the support from the first day onwards before I even started with the thesis. First in Trondheim, and thereafter continuing with online meetings. Bart Ummels from TU Delft, thank you for giving me useful insights into combining the theory with methods applied in practice. Rogier de Bruijn from GustoMSC, thank you for your dedication to this project and your help in heading in the right direction during this study.

I would also like to thank Jeroen Hoving from TU Delft for your helpful feedback during the progress meetings. Your feedback helped me in fine-tuning the direction of the thesis. And Yuna Zhao, I am grateful that you gave helpful feedback and tips during the final stages of this thesis. Special thanks are also due to GustoMSC, for giving me the opportunity to cooperate on this thesis. I got all the support and tools that I needed.

Finally, I want to thank my family for their constant support and encouragement, which have been the foundation of my studies. Their belief in me has been my greatest motivation in completing this adventure.

I consider myself fortunate to have collaborated with such dedicated and insightful professionals, and I am really grateful for the things I learned throughout this journey.

*Menno Hoogeslag
Amersfoort, August 2024*

Abstract

The global concern over climate change has accelerated the shift towards renewable energy sources, in which floating offshore wind energy is expected to play an important role. A floating wind turbine could be installed in a harbour using a quayside crane. Various types of floating foundations are available, where a semi-submersible floater has the advantage of versatility in different water depths due to its small draft. However, the continuous upscaling of wind turbine sizes introduces new challenges for the installation process. Installing these larger turbines requires the use of the world's largest cranes and large quaysides. The operability of the wind turbine generator (WTG) installation has a significant impact on the planning and feasibility of a floating wind farm project. Therefore, this research is aimed at studying and understanding the factors that influence the operability of the WTG blade installation on a semi-submersible floating wind foundation using a quayside crane.

To investigate how the dynamics of the floater and blade are affected by wind and wind conditions, a numerical model is developed. This is done in frequency domain which allows for fast calculations to gain insight into a variety of parameters. The floater model includes a 3D wave diffraction-radiation analysis, as well as a procedure for including viscous damping. Moreover, a response-based approach is applied to obtain the characteristic displacement and velocity of the turbine hub, which correspond to specific sea states. The blade is modelled as a pendulum with two degrees of freedom in axial and radial directions. Taglines are modelled as spring dampers that reduce the blade motions. A similar response-based method is used to obtain the characteristic motions that correspond to specific wind speeds and directions. During the critical alignment and mating phases, the relative displacement and velocity between the blade root and turbine hub are the limiting factors for installation. These relative motions, that follow from the floater and blade model, are then used to calculate the allowable environmental conditions for the wind turbine blade installation. There after, these allowable conditions are combined with metocean data to obtain the operability.

The model is used to study the sensitivities of parameters for the blade and floater motions. Aligning the blade with the wind is the most effective way to reduce blade motions because the motions in the axial direction are significantly lower compared to the radial direction. The influence of the distance between the quayside and the floater is also studied. For specific sea states, there are beneficial distances. However, when considering a large range of sea states, there is no significant advantage for certain distances. An important parameter affecting the relative motions between the blade and hub is the nacelle and blade heading. Optimising this orientation significantly increases the allowable environmental conditions. For low wind speeds, the optimal relative nacelle heading with respect to the wind and wave directions is dependent on these directions. For high wind speeds, above approximately 6.5 m/s , the blade should be aligned with the wind. Additionally, the lowest motions occur when the nacelle is rotated inward, closer to the floater's centre of gravity.

Five different blade installation strategies are studied to identify one that yields the highest operability. A method where the nacelle and blade heading is adjusted to the optimal position for each change in environmental conditions yields the highest theoretical operability. However, in practice, a better solution is to select a single nacelle heading that is optimised for high wind speeds from a dominating wind direction. Utilising this strategy, it was found that a yearly operability of approximately 65% and 45% could be achieved for installing the turbine blade in a sheltered and exposed harbour, respectively. During the summer months, this operability increases to approximately 80% and 58%, respectively. The operability is mainly driven by wind-induced motions, so a location where wind speeds are low is favourable for achieving high operability.

In conclusion, this research contributes to the understanding of the critical factors that influence the operability of wind turbine blade installation on floating foundations, which is a crucial step in the upscaling of floating offshore wind technology.

Contents

Preface	i
Abstract	ii
Nomenclature	ix
1 Introduction	1
1.1 Floating Offshore Wind Energy	1
1.1.1 Floating Wind Foundations	2
1.1.2 FOWT Installation Methods	4
1.1.3 WTG Lifting Methods	4
1.2 Blade Installation Procedure	5
1.2.1 Critical Installation Phases	6
1.3 Operability	7
1.4 Problem Description	8
1.5 Research Objective & Approach	9
1.5.1 Modelling Scope	9
1.5.2 Approach	10
1.6 Report Outline	11
2 Theoretical Framework	12
2.1 Waves Floater Model	12
2.1.1 Wave Spectrum	13
2.1.2 Wave Reflections	14
2.2 Hydrodynamic Damping	15
2.2.1 Heave Plate Damping	15
2.2.2 Heave Plate Experimental Results	17
2.3 Wind Blade Model	17
2.3.1 Kaimal Wind Spectrum	18
2.4 Single-Blade Installation Limit Criteria	19
2.5 Software	21
2.5.1 Rhino	21
2.5.2 WAMIT	21
2.5.3 pyCalmot	22
3 Modelling Strategy & Model Input	23
3.1 Model Assumptions	23
3.2 Modelling Strategy	25
3.3 Coordinate Systems	26
3.3.1 Relative Wind Directions	28
3.4 Model Input	28
3.4.1 Semi-Submersible Floater	28
3.4.2 Turbine & Blade	30
3.4.3 Crane	31
3.4.4 Yoke & Taglines	32
3.5 Metocean Data	33
4 Dynamic Model	36
4.1 Wave Diffraction-Radiation Analysis	36
4.1.1 3D Panel Model	36
4.1.2 3D Diffraction-Radiation Model	37

4.1.3	Mesh Convergence Study	37
4.2	Floater Motions	39
4.2.1	Solve Floater EOM	39
4.2.2	Shallow Water Effect	42
4.2.3	Heave Plate Viscous Damping	43
4.2.4	Braces Viscous Damping	45
4.2.5	Added Mass Effect	46
4.3	Characteristic Hub Motions	46
4.3.1	Hub Motion Response Spectra	47
4.3.2	Characteristic Hub Motions Calculation	47
4.4	Characteristic Blade Motions	48
4.4.1	Solve Blade EOM	49
4.4.2	Calculate Motion Response Spectra	50
4.5	Allowable Environmental Conditions	51
4.5.1	Hub Motion Limits	52
4.5.2	Calculate Allowable Environmental conditions	52
4.6	Operability	52
5	Results	54
5.1	Blade Motions	54
5.1.1	Suspension Length Sensitivity	54
5.1.2	Tagline Diameter Sensitivity	55
5.1.3	Blade Orientation Sensitivity	56
5.2	Floater Motions	57
5.2.1	Quayside Distance Sensitivity	57
5.2.2	Critical Hub Motions	63
5.3	Relative Motions	64
5.3.1	Nacelle Heading Sensitivity	64
5.3.2	Optimal Blade & Nacelle Heading	68
5.4	Operability	69
5.4.1	Strategy 1: Fixed Nacelle Heading 0°	69
5.4.2	Strategy 2: Fixed Nacelle Heading -90°	70
5.4.3	Strategy 3: Fixed Nacelle Heading Optimised for Low Wind Speeds	70
5.4.4	Strategy 4: Fixed Nacelle Heading Optimised for High Wind Speeds	71
5.4.5	Strategy 5: Alternating Nacelle Heading	71
5.4.6	Installation Strategy Comparison	72
5.4.7	Effect Quayside Distance on Operability	73
5.4.8	Wind & Waves Importance	74
6	Conclusions & Recommendations	76
6.1	Conclusions	76
6.2	Recommendations	77
	References	79
A	Irregular Frequencies	82
B	Floater Meshes	83
B.1	Triangular & Quad Mesh Elements	83
B.2	Mesh Convergence Study	83
C	Heave Plate Experiments	86
D	Blade Properties	89
E	Blade Equations Of Motion	92
F	Results	95
F.1	Suspension Length	95
F.2	Tagline Diameter	95
F.3	Blade Orientation	96

F.4	Quayside Distance	96
F.5	Limiting Floater Motions	101
F.6	Nacelle Rotation	102

List of Figures

1.1	World average leveled cost of wind energy	2
1.2	Floating foundations	3
1.3	Number of assembly lifts	5
1.4	Three single blade installation orientations	6
1.5	Lifting, alignment, and mating phase	7
1.6	Operation periods for marine operations	8
1.7	Standard situation layout	10
1.8	Research approach	11
2.1	Wave spectrum transformation	14
2.2	Diamond pattern wave reflections	15
2.3	Kaimal wind spectrum	19
2.4	Safety boundary in radial and axial planes.	20
2.5	Blade impact in radial and axial planes.	21
3.1	Flow diagram modelling strategy	26
3.2	Coordinate systems and wave directions	27
3.3	Relative wind & wave directions for blade & nacelle headings	28
3.4	Tri-Floater impression	30
3.5	Installation site dimensions & tagline configuration	33
3.6	Map of locations in port of Rotterdam	33
3.7	Wave and wind conditions sheltered location	34
3.8	Wave and wind conditions exposed location	35
4.1	Modelling strategy wave diffraction-radiation analysis.	36
4.2	Tri-Floater mesh model with detail	37
4.3	Added mass for seven meshes	38
4.4	Maximum relative error added mass	39
4.5	Modelling strategy floater motions.	39
4.6	Displacement RAO at COG for three wave directions	40
4.7	Displacement RAOs at hub for in radial direction	41
4.8	Displacement RAOs for deep and shallow water	42
4.9	First order wave force RAOs for deep and shallow water	43
4.10	Iterative heave motion RAO	44
4.11	Comparison between literature and pyCalmot software	45
4.12	Heave motion RAO including braces	46
4.13	Modelling strategy characteristic hub motions.	47
4.14	Modelling strategy characteristic blade motions.	48
4.15	Blade radial displacement and velocity response spectra	51
4.16	Modelling strategy allowable environmental conditions	51
4.17	Modelling strategy operability.	53
5.1	Suspension length effect on radial blade motions	55
5.2	Tagline stiffness effect on radial blade motions	56
5.3	Blade orientation effect on displacement	57
5.4	Quayside distance dependent displacement RAOs for surge, sway, and heave	58
5.5	Quayside distance dependent characteristic radial displacement vs. peak period	59
5.6	Quayside distance dependent characteristic axial displacement vs. peak period	60
5.7	Quayside distance dependent allowable H_s vs. peak period	61

5.8	Allowable H_s vs. wave direction for different peak periods and quayside distances . . .	62
5.9	Quayside distance dependent minimum allowable H_s vs. peak period	63
5.10	Limiting floater motions for different wave directions and peak periods	64
5.11	Limiting floater motions vs. relative nacelle heading for multiple directions	65
5.12	Relative nacelle heading dependent allowable H_s for different T_s and environmental di- rections at $V_w = 2$ m/s	66
5.13	Relative nacelle heading dependent allowable H_s for different T_s and environmental di- rections at $V_w = 8$ m/s	67
5.14	Optimal nacelle heading vs. T_p for different wind speeds	67
5.15	Optimal nacelle heading vs. V_w for different wind/wave directions	68
5.16	High wind speed blade installation heading for optimum β_{relative}	69
5.17	Operability & top view installation strategy 1	70
5.18	Operability & top view installation strategy 2	70
5.19	Operability & top view installation strategy 3	71
5.20	Operability & top view installation strategy 4	71
5.21	Operability installation strategy with rotating nacelle heading	72
5.22	Comparison of operability for five strategies at the sheltered site	72
5.23	Comparison of operability for five strategies at the exposed site	73
5.24	Comparison of operability for five quayside distances at the exposed site	74
5.25	Sensitivity of operability to environmental conditions	75
A.1	Irregular frequency effect	82
B.1	Added mass for triangular and quad meshes	83
B.2	Different Tri-Floater mesh sizes	84
B.3	Added mass for seven meshes	84
B.4	Potential damping for seven meshes	85
B.5	Wave force RAO for seven meshes	85
C.1	Added mass and damping for different KC numbers and diameter ratios	87
C.2	Plate submergence effect on damping	88
C.3	Plate submergence effect on added mass	88
D.1	Drag coefficient of wedges and cones vs. half-vertex angle	91
F.1	Suspension length effect on axial blade motions	95
F.2	Tagline stiffness effect on axial blade motions	96
F.3	Blade orientation effect on velocity	96
F.4	Quayside distance dependent displacement RAOs for roll, pitch, and yaw	97
F.5	Quayside distance dependent characteristic radial velocity vs. peak period	98
F.6	Quayside distance dependent characteristic axial velocity vs. peak period	99
F.7	Quayside distance dependent allowable H_s vs. peak period	100
F.8	Limiting floater motions for thirteen different wave directions and peak periods	101
F.9	Relative nacelle heading dependent allowable H_s for different T_s and environmental di- rections at $V_w = 2$ m/s	102
F.10	Relative nacelle heading dependent allowable H_s for different T_s and environmental di- rections at $V_w = 8$ m/s	103
F.11	Optimal nacelle heading vs. T_p for different wind speeds and directions	104

List of Tables

2.1	Critical Events and Limiting Parameters	21
2.2	Overview of used software	21
3.1	Motion components of floater	28
3.2	GustoMSC Tri-Floater dimensions	29
3.3	Tri-Floater loading conditions	29
3.4	IEA Wind 15 MW turbine parameters	31
3.5	Crane properties	31
3.6	Yoke & tagline properties	32
3.7	Environmental conditions	34
5.1	Suspension length sensitivity	55
5.2	Tagline stiffness sensitivity	56
5.3	Comparison of yearly operability for five strategies	73
C.1	Oscillation amplitudes and frequencies used in experiments	86
D.1	Airfoils with drag coefficient along blade span	89
D.2	Blade dimensions and drag coefficients	90

Nomenclature

Abbreviations

Abbreviation	Definition
FOWT	Floating Offshore Wind Turbine
WTG	Wind Turbine Generator
COP	Conference Of the Parties
TLP	Tension Leg Platform
EOM	Equation Of Motion
COG	Centre Of Gravity
RAO	Response Amplitude Operator
LCOE	Levelized Costs of Energy
AOA	Angle Of Attack
MBL	Minimum Breaking Load
KC	Keulegan Carpenter

Introduction

Climate change, fueled by human activities like burning fossil fuels and deforestation, is becoming a severe threat to the planet. It leads to rising temperatures, extreme weather events and ecosystem disruptions. In response to climate change, 'The Paris Agreement' (UNFCCC 2024) was established during COP21 (Conference of the Parties) in 2015. It demonstrates a global commitment to limiting temperature increases to well below 2 degrees Celsius, with an aim of keeping the rise to 1.5 degrees Celsius. Each participating nation outlines its specific targets and measures, emphasizing collective action to combat climate change and promote a sustainable, low-carbon future.

This global concern over climate change has accelerated the shift towards renewable energy sources. Wind energy is a crucial player in this energy transition. Unlike traditional fossil fuels, wind energy offers electricity generation without greenhouse gas emissions or air pollution. Technological advancements have improved the efficiency and reduced the costs of wind turbines. These developments make wind energy increasingly competitive and attractive to governments, businesses, and investors. Countries worldwide seek to meet their commitments under the Paris Agreement. Wind energy can be a key contributor to this global effort in mitigating climate change.

In 1887 was the first wind turbine created for electricity generation by Professor James Blyth from Scotland. It marks the initial step in the evolution of wind energy technology. Since then, this innovation has been further developed into a crucial renewable energy source (NES-Fircroft 2022). Initially, the turbines were only used onshore, so located on land. A milestone in 1991 marked the expansion into offshore wind farms. Construction of the first offshore wind farm, with 11 turbines, occurred in Denmark (Ørsted 2024). The installed capacity, which is the maximum output that a wind farm can produce under ideal conditions, of 5 MW was relatively low, compared to today's wind farms. However, this breakthrough can be seen as the foundation for the growth of modern offshore wind farms.

There are multiple reasons for the offshore expansion of wind energy, where the fundamental advantage is the higher wind quality. Generally, wind speeds are higher and more uniform offshore. This increases the energy production and lowers the cycling loading, and therefore the fatigue, on the turbine (Brunel 2021). A drawback is the harsh environment to which the turbines and foundations are exposed at the offshore location.

1.1. Floating Offshore Wind Energy

A relatively new development in the offshore wind industry is the floating offshore wind turbine (FOWT). Currently, most turbine foundations are bottom-fixed where the foundation is directly placed on the seabed (WindEurope 2023). Bottom-fixed foundations are however limited by water depth and therefore deployed in coastal areas. With up to 60 metres of water depth, these fixed foundations are economically feasible. Beyond this depth, the foundations might still be technically possible, but the costs are too high to make sense commercially. For larger water depth FOWTs are an economically attractive solution with large potential. Floating foundations can be deployed in deeper waters where bottom-fixed foundations are not feasible. Another advantage is that floating offshore wind turbines can

be deployed further offshore benefiting from stronger and more consistent wind. On the other hand, the costs are higher compared to a close-to-shore bottom-fixed foundation (PMI-Industries 2016).

Floating offshore wind energy is expected to increase its share of the total wind energy sector. In 2050, there will be a worldwide installed capacity of approximately 270 GW (Veritas 2023). This large expansion will be enabled by a reduction in the Levelized Cost of Energy (LCOE), which measures the average cost per unit of electricity generated over the lifetime of an energy-producing system. In 2023, the LCOE was more than three times as high for floating wind, compared to bottom-fixed wind energy (270USD/MWh over 80USD/MWh). It is projected that the difference between these two technologies will reduce to 30% in 2050, due to the benefits of economies of scale and improved efficiencies in production. The long-term projected trend of the LCOE can be seen in Figure 1.1. This thesis is aimed at enhancing the installation of FOWTs, which contributes to the economy of scale of installing numerous turbines.

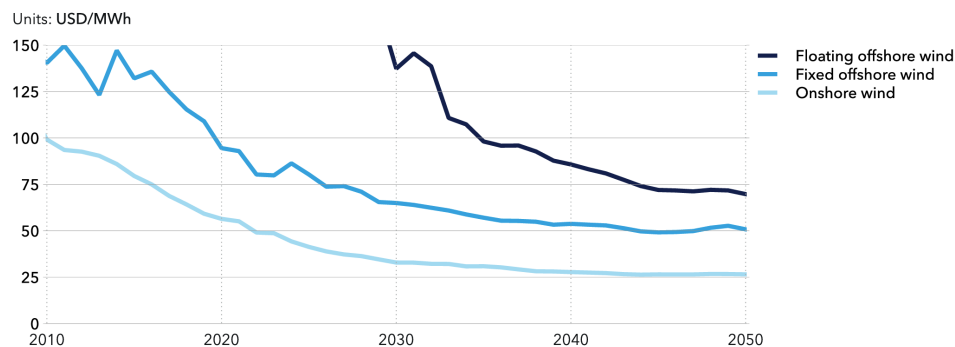


Figure 1.1: World average levelized cost of wind energy.

Source: Veritas 2023

1.1.1. Floating Wind Foundations

An offshore turbine requires a foundation that is able to transfer the loads, which are not transferred into rotor rotation, to the seabed. The combination of the floating structure and mooring system provides the stability and stationkeeping of the FOWT. The optimum mooring system design depends on technical and economical trade-offs for the offshore site and type of floating foundation. FOWTs can be distinguished by how they achieve stability in four categories. An overview of these categories is shown in figure 1.2. These four concepts are briefly discussed below.

Semi-submersible

Semi-submersibles consist of vertical columns that are connected. Typically this connection is formed by horizontal and diagonal braces, but there are other design possibilities. Usually, heave plates are attached at the bottoms of the columns to increase the damping and added mass. Stability is mainly obtained from the buoyancy of the platform (Barooni et al. 2022). A mooring system also contributes to the stability of the structure. Typical mooring systems for semi-submersibles consist of spread catenary, semi-taut, or taut mooring lines. These lines can be made out of chains, spiral strand wires, and synthetic rope components. Due to the catenary shape, there is a horizontal tension that reduces the horizontal motions of the structure induced by environmental loads. At the seabed, the mooring system is commonly anchored with drag embedment or suction pile anchors (Longridge 2023).

An advantage of this floater type is its versatility in different water depths, due to its relatively small draft. Moreover, the operation and maintenance are relatively easy when the turbine is placed at the edge of the floater. Downsides are the substantial amount of material used in the structure, and the relatively complicated fabrication of the floater (Tacx 2019). The most widely used semi-submersible foundation in the industry is the WindFloat, designed by Principle Power. It has been used in the WindFloat Atlantic and Kincardine Offshore Floating Wind Farm projects (Principle-Power 2021). Three 8.4 MW turbines have been installed, 20 km out of the Portuguese coast. At this location, the water depth is 100 metres. The larger Kincardine project consists of five 9.5 MW turbines, located 15 km out of the Scottish coast. The water depth is between 60 and 80 metres.

Spar

A spar consists of a vertical floating cylinder buoy that is connected to the seabed via a mooring system that is comparable to that of the semi-submersible. Typically, the same mooring lines and anchors can be used to provide the horizontal restoring force. The spar's stability is obtained by ballasting the buoy, and therefore lowering the centre of mass with respect to the centre of buoyancy (Barooni et al. 2022). An important advantage of this foundation is the relative ease of fabrication, which makes it possible for mass production. A disadvantage is the large draft, which complicates the installation at the location (Tacx 2019). Eleven spar foundations have been used in the largest floating wind farm to date, Hywind Tampen. This wind farm is located 140 km off the Norwegian coast and has an installed capacity of 88 MW (Equinor 2023). The 8 MW turbines are floating on concrete buoys with a length of 107 metres.

Tension Leg Platform

The Tension Leg Platform (TLP) obtains its stability from excess buoyancy as well as the high tension in the vertical taut tethers. The upward buoyancy force is counterbalanced by the gravitational force and the pre-tension in the tethers anchored to the seabed. This design has a small footprint since the foundation is directly under the floater. This could be beneficial for some locations. Besides, the structure is light, which reduces the material use. A drawback is that the stability completely depends on the tethers and anchors. If there is a failure, the turbine will fall over (Barooni et al. 2022). The technology is currently under development to become commercially available. X1 Wind is scaling up its prototype platform design in its NextFloat project to de-risk future commercial projects. The wind turbine size that will be installed, in the French Mediterranean Sea, is 6 MW. The company's goal is to develop foundations for turbines exceeding 15 MW after 2026 (Wind 2024).

Barge

A barge obtains its stability from distributing the buoyancy over a large water plane area. In the centre is a moonpool, that has the function of reducing the wave loads. Furthermore, the barge is kept in place by a catenary mooring system (Barooni et al. 2022). Barges are used in small-scale projects. In Kitakyushu, Japan, there is a 3 MW prototype FOWT in operation since 2018. The BW Ideol's barge foundation has been installed at a location with 55 metres of water depth. Currently, they are scaling up their design for a project with three 10 MW turbines in the French Mediterranean Sea, 18 km off the coast (Ideol 2024). This small farm is expected to become operational in 2025.

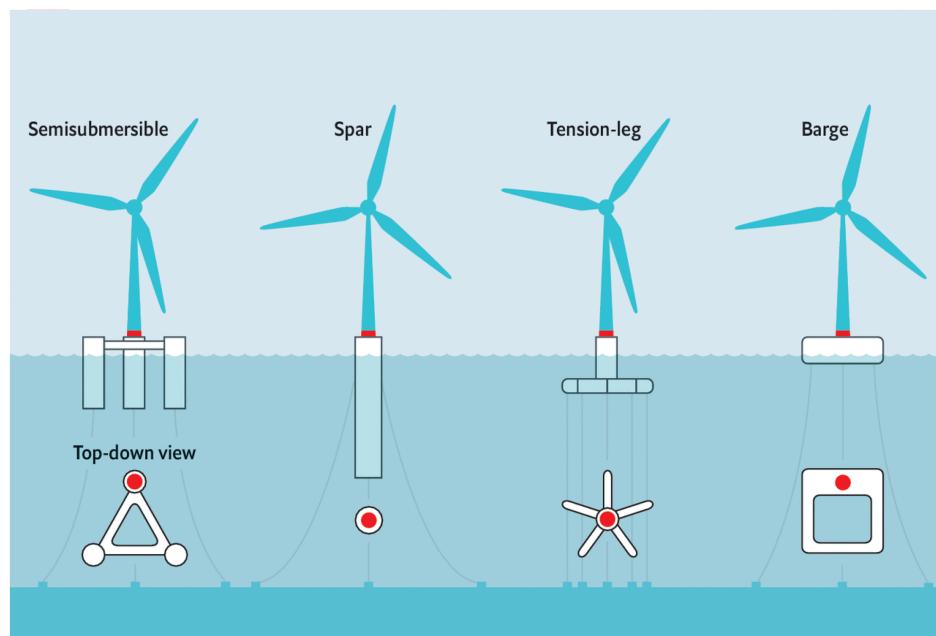


Figure 1.2: Schematic overview of FOWT foundations.

Source: Mei and Xiong 2021

1.1.2. FOWT Installation Methods

Installing FOWTs is a challenging undertaking and generally more complex than its onshore counterpart. Offshore turbines are typically larger and the marine environment is more harsh than onshore. Hence, there is a need for specialized vessels and equipment. Moreover, the larger distance to shore makes the logistics more complex and requires more safety measures.

One option for installing the wind turbine generator (WTG) on its floating foundation is to perform the installation offshore using a floating vessel. This approach allows for the transport of the floater and WTG to the offshore site separately. At the offshore location, the WTG can be installed on the floating foundations. This is advantageous for spar and TLP foundations since these foundations require little space onboard which makes the use of transport vessels more convenient than for larger foundations (Heerema 2022). However, this is not the only installation method, because the installation of the Hywind Tampen turbines was performed in the Gulen Industrial Harbor. This harbour is located in a deep Norwegian fjord, which is necessary for the spar buoys with a large draft. After the installation, the turbines were towed to the offshore location. A drawback of this method is the restriction to suitable installation harbours with only very deep water.

For semi-submersibles, it is common practice to install the wind turbine on its foundation in the harbour, after which the FOWT is towed to the wind farm. At the offshore location, the floater's mooring is deployed and the connection to the electricity grid is made. A potential installation method for installing the WTG on the FOWT is by using a quayside fixed crane that installs the turbine components on the floating semi-submersible (BVG-Associates 2023). The advantage is that the installation can take place in a sheltered area where the environmental conditions are milder compared to the offshore location.

1.1.3. WTG Lifting Methods

Different methods can be used to place a wind turbine on its foundation. The turbine can be installed on the foundation with only one lift, or up to six lifts, as can be seen in figure 1.3. The most beneficial method depends on various factors, such as turbine design, crane lifting capacity, distance to shore, environmental conditions, and logistical capacity (Jiang 2021).

For a single lift installation, the turbine is completely assembled, whereas for two lifts, the lower tower segment is installed separately from the rest of the turbine. These methods have the advantage that there is less time required at the offshore location for the installation. This is mostly relevant for bottom-fixed foundations since they are always installed offshore. A disadvantage of these methods is that the lifting capacity of the crane(s) should be sufficiently large. To mitigate this disadvantage, it is possible to install the turbine in three or four lifts. The 'bunny ear' technique refers to the method where a pre-assembled nacelle, rotor hub, and two blades are lifted in one piece onto the tower. The third blade is installed thereafter. A commonly used technique is the full rotor lift, where the pre-assembled rotor hub and three blades are installed on the nacelle. These methods reduce the necessary lifting capacity and make it possible to use deck space more efficiently. A drawback is the increased complexity of the assembly (Kuijken 2015).

The number of lifts can be further increased to six lifts where the two tower parts, the nacelle, and three blades are installed individually. According to Jiang (2021), the trend in the bottom-fixed industry is to assemble turbines in five or six lifts, because of the growth in turbine sizes. This method requires a lower lift capacity compared to the single-lift method. Although crane capacity might be less critical for a quayside crane than for offshore operations, it can still be beneficial to install the components directly on the floater one by one. This is more time-efficient than assembling the turbine with a similar crane and then lifting it onto the foundation in one piece. Given its common use in bottom-fixed projects and recent floating projects like Kincardine and Hywind Tampen, the single-blade installation will likely be the preferred lifting method.

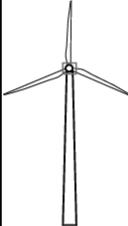
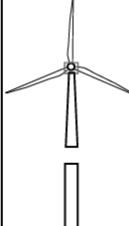

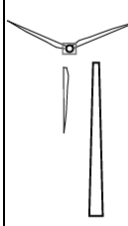
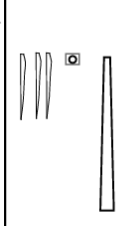
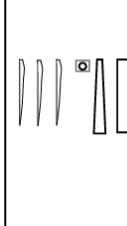
Installation method						
Number of lifts	1	2	3 to 4	3 to 4	5	6

Figure 1.3: Number of lifts for assembly of different OWT components.

Source: Jiang 2021

1.2. Blade Installation Procedure

This research focuses on the single-blade installation with a quayside crane, which consists of three main phases: lifting, alignment, and mating. Sketches of these three phases are presented in Figure 1.5.

Lifting Phase

The blade is loaded into a blade yoke on the quay at the beginning of the lifting phase. The ideal gripping point is at the centre of mass, so the blade does not tend to rotate under its own weight. The yoke is connected to the crane hook by cables. Usually, there are taglines between the crane boom and the yoke to control and reduce the motions of the blade. Thereafter, the blade and yoke will be lifted by the crane to approach the hub at a safe distance, minimising the risk of impact. If it is installed under an angle, then the rotation of the blade takes place during the lifting phase. Figure 1.4 depicts the three possible blade installation orientations: vertical, tilted, and horizontal (Zhao 2019).

An advantage of the vertical orientation is that the required lifting height of the crane can be lower because the yoke grips below hub height. However, the crane height is still determined by the hub height for the installation of the nacelle. Therefore, this orientation has more potential for blade replacement during maintenance. Additionally, the wind downstream the tower is more turbulent which complicates the installation.

Tilted installation eliminates the need for a rotation of the rotor, which is preferable for direct-drive turbines. Without a gearbox, it is harder to rotate the hub, which is necessary for vertical and horizontal installation. A drawback is that the crane should be able to lift above the hub height.

The horizontal orientation is commonly preferred since the crane can be the same size as for the installation of other components. Moreover, blades are usually stored horizontally on the quayside, so it is not required to rotate the blade during the lift. For these reasons, the horizontal single-blade installation will be studied in this thesis work.

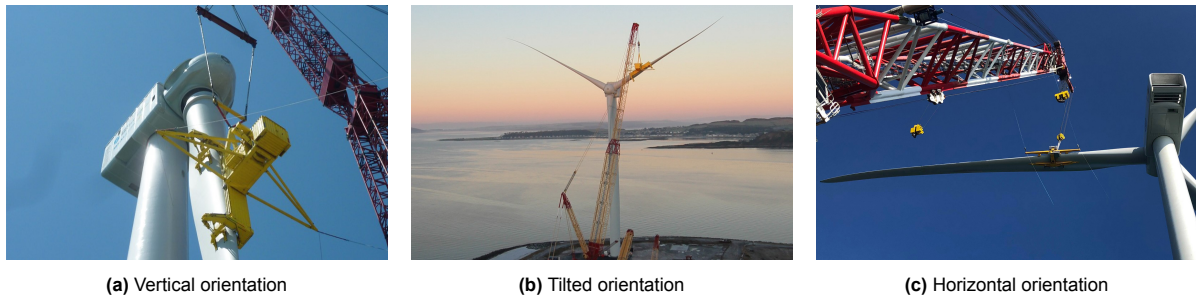


Figure 1.4: Three single blade installation orientations

Source: Liftra 2024

Alignment Phase

Before the connection between the blade and the hub can be made, the blade root must be aligned with the hub. Most turbine blades are designed to form a connection with the hub via T-bolts that are placed uniformly across the circumference of the blade root. When the blade manufacturing is complete, the steel bolts are screwed into barrel nuts that are in the root laminate. The result is a blade root with bolts sticking out that should make a connection with the flange holes in the hub. A few longer bolts are present in addition to the load-carrying bolts. These so-called guiding pins help during the mating phase to make the actual connection with the hub (Verma, Jiang, Vedvik, et al. 2019).

An installation team inside the turbine hub monitors the relative motions between the blade root and the hub. The longer guidance pins help with visually monitoring these motions. When the alignment falls within acceptable limits and is expected to stay within these limits for the required installation time, and the installation team deems the conditions safe, the mating phase can commence.

Mating Phase

Contact between the hub and blade root is made during the mating phase. The crane carefully hoists the blade to the hub's mounting point, where technicians guide the pins into the correct flange holes. Once it is in place, the steel bolts are fastened to secure the blade to the hub. This completes the mating process. Good coordination between the crane operator and the installation team is required during the mating phase to ensure an accurate, secure and safe attachment. For the successful execution of this phase, it is essential that the components do not get damaged. There is a relation between the damage and the impact velocity of the blade root and turbine hub. Hence, this impact velocity should not exceed a predefined limit for the mating phase to succeed.

1.2.1. Critical Installation Phases

Generally, the alignment and mating phases are considered to be critical for blade installation. When the relative motions are too large, the mating phase cannot commence. If the impact velocity and forces are excessive, damage is likely to occur in the guide pins and blade root. If the relative motions or impact velocity is too large during the alignment or mating phase, the installation has failed. This thesis will consider the alignment and mating phases as critical events for the blade installation operability.

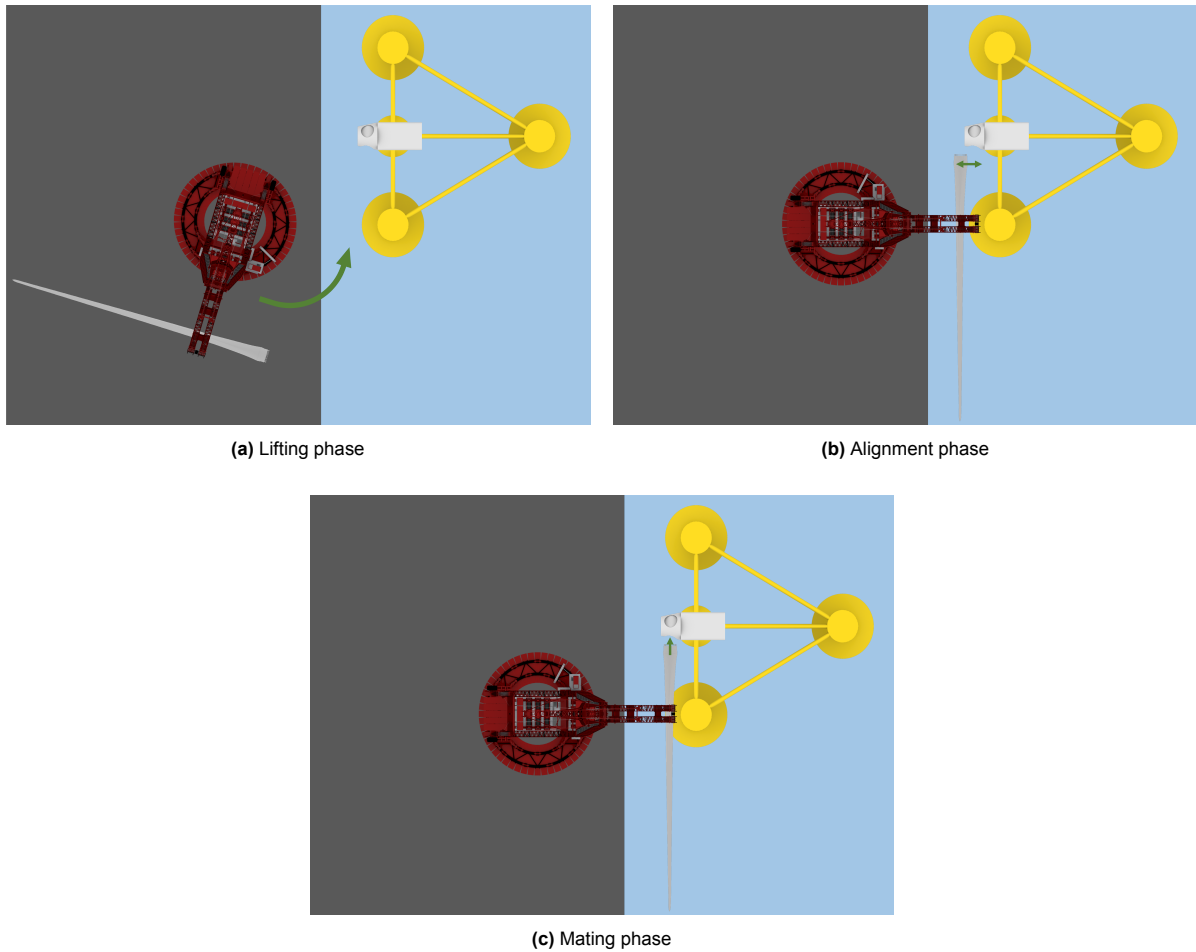


Figure 1.5: Drawings of the three installation phases: lifting, alignment, and mating.

1.3. Operability

A marine operation, like a blade installation, can only be executed under certain conditions. Operability represents the percentage of time during a given reference period (e.g., a year) when the environmental conditions are within the allowable limits for safely executing the marine operation. It is assessed using the operational limits, which are defined by environmental conditions under which the marine operation can be safely executed (Acero et al. 2016). These environmental conditions could be expressed in terms of allowable significant wave height, wave peak period, and mean wind speed.

By comparing the allowable limits to the actual environmental conditions at the installation site, the workable weather windows can be identified. The ratio between the available workable weather windows and the maximum possible number of windows for the lifting operation corresponds to the operability. Assessing the operability during the planning phase provides information for feasibility, selection of equipment, and optimization of the installation process.

The required weather window is defined by the planned operation period (T_{POP}) and an added estimated contingency time (T_C). These two periods combined form the operation reference period (T_R). T_{POP} should be based on a detailed schedule with a conservative estimation of the time required for each task. T_C accounts for general uncertainty in the planned operation time, unproductive time during the operation, and possible contingency situations. If the required time for contingency situations is not assessed in detail, it should be at least as long as T_{POP} (DNVGL-ST-N001 2018). To be able to execute the operation, it shall be planned to be executed within a reliable weather window. This window is defined as the period between the issuance of the last weather forecast and the completion of the operation. An overview of the described operation periods can be seen in figure 1.6.

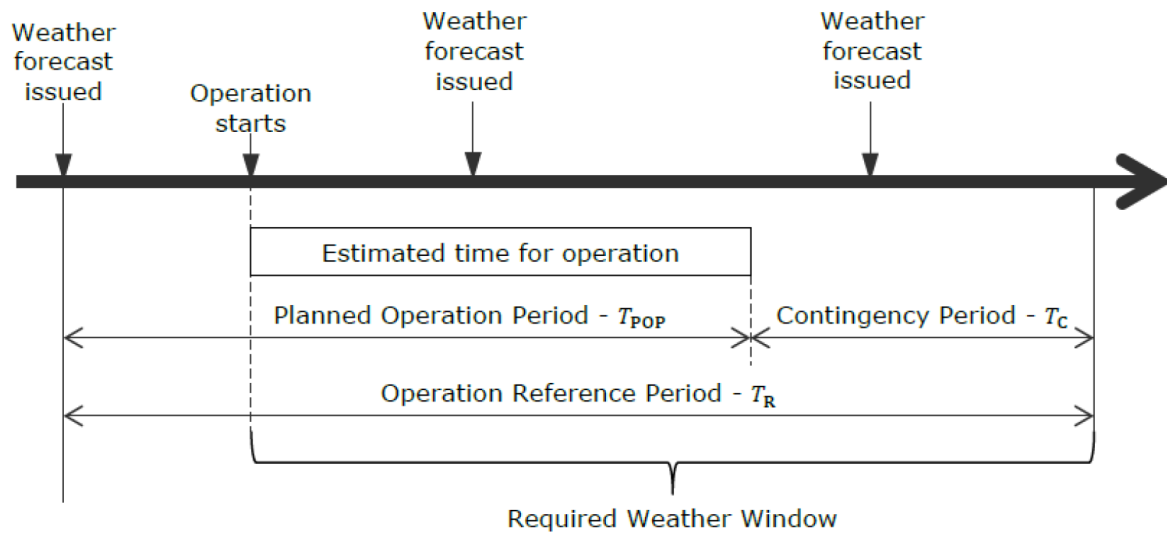


Figure 1.6: Operation periods for marine operations.

Source: DNVGL-ST-N001 2018

1.4. Problem Description

The high demand for sustainable wind energy has led to the development of enlarged turbine sizes and increased-scale wind farm projects. Nowadays, there are small-scale floating wind projects operational where the turbines are relatively small. Larger projects are under development where the turbine size is in the order of 15-20 MW. Increasing the scale is important to reduce the costs of floating wind energy, and make it more competitive with other energy sources. Challenges, related to engineering, production, logistics, installation, and maintenance, arise with increasing the wind turbine size and the scale of floating wind farm projects. One of the challenges is related to the installation of WTG on the floating foundation, especially when performing this installation on a large scale.

This research focuses on the WTG installation on a semi-submersible foundation with a quayside crane. Operations like this have only been executed a few times for relatively small turbines, in the order of 9 MW. This has not been done before for larger turbines. Installation of these larger turbines requires the biggest cranes that are available in the world and large quaysides with sufficient space for logistics.

The operability of the WTG installation has a significant impact on the planning of a floating wind farm project. Floating offshore wind turbines are to be produced and installed on a large scale. Hence, a small inaccuracy in the operation window estimation leads to a large deviation in the project planning and therefore an increased project risk. To optimise the operability of a WTG installation on a floating foundation, it is important to understand the influencing parameters.

The installation of the turbine blade is considered to be critical for the operability of the WTG installation. This is because the relative motions between the blade root and the turbine hub must remain within very small limits due to the delicate connection between these two components. The motions of the blade excited by wind loads and the motions of the hub due to floater motions excited by wind and wave loads, result in relative motions between the blade root and turbine hub. It is important to know what the operability of a wind turbine blade installation on a semi-submersible floating wind foundation next to a quayside is because it contributes to the up-scaling of the floating wind energy sector.

1.5. Research Objective & Approach

The objective of this research is to determine the operability of a wind turbine blade installation on a semi-submersible floating wind foundation using a quayside crane. The methodology for determining this operability will be applied to the GustoMSC Tri-Floater designed for the 15 MW NREL reference turbine (Gaertner et al. 2020) at a typical installation site.

From the research objective, the main research question follows:

‘What is the operability of a wind turbine blade installation for a semi-submersible floating wind foundation using a quayside crane?’

To answer this main research question, the following sub-questions are being considered:

- What are the operational limits, imposed by environmental conditions, during wind turbine blade installation?
- How can the motions of a semi-submersible floating foundation next to a quayside be modelled?
- How can the motions of a wind turbine blade, suspended from a quayside crane, be modelled?
- What are the relative motions between a turbine hub on a semi-submersible floating foundation and a suspended turbine blade?
- How can the impact of environmental conditions be mitigated to improve the operability of a wind turbine blade installation?

1.5.1. Modelling Scope

This research exclusively focuses on the critical alignment and mating phases of single-blade installation, assuming the successful completion of the lifting phase and installation of other WTG components. The scenario studied involves a semi-submersible WTG foundation floating next to a quayside. On the semi-submersible, the turbine tower and nacelle are pre-installed, so only the three blades need to be installed. On the quayside, a ring crane is placed with a horizontally suspended wind turbine blade. This blade is clamped by a blade yoke which is connected to the crane via a crane cable and horizontal taglines. An overview of the installation operation is presented in figure 1.7. This research focuses on the relative motions between the turbine hub and blade root induced by waves and wind, and how these environmental conditions affect the installation operability. The wave-induced motions of the turbine hub are analysed in detail, while a simplified blade motion model is used to understand how wind and waves limit blade installation. Additionally, different installation strategies with a variety of blade headings are explored.

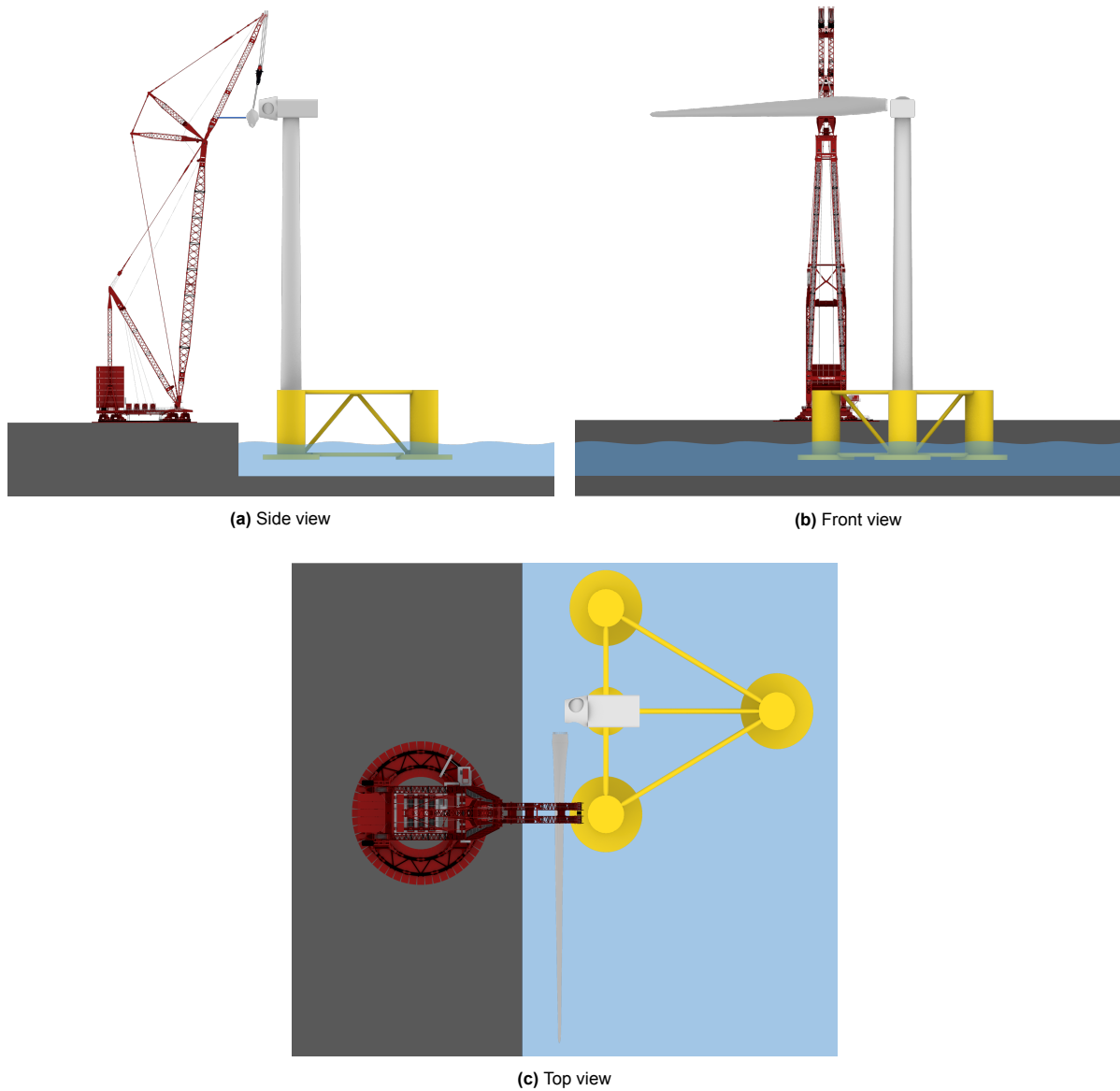


Figure 1.7: Sketches of the standard situation layout.

1.5.2. Approach

A numerical model is made to study the operability of a single-blade installation that is subject to wind and wave loads. The installation is modelled in frequency domain, which has the advantage that the calculation time is significantly lower compared to time domain. This allows for a quick analysis of the bodies dynamics for a range of environmental conditions and installation scenarios. The model includes the floating structure and blade as rigid bodies. Furthermore, taglines are modelled as a spring-damper system that exerts force in tension and compression. The primary external loads considered are hydrodynamic loads on the floater and wind and tagline loads on the suspended blade. The model requires detailed inputs about the semi-submersible foundation, wind turbine, installation equipment, operational limits, and environmental data. The model processes these inputs to provide outputs in terms of allowable environmental conditions under which the installation can be conducted and operability. These outputs are then used to conduct sensitivity studies for the blade and floater motions. Thereafter, the results of the sensitivity studies are used to enable improvements to the installation arrangement and operability. An overview of the modelling approach is presented in Figure 1.8. More details about all these steps will be discussed in chapter 3.

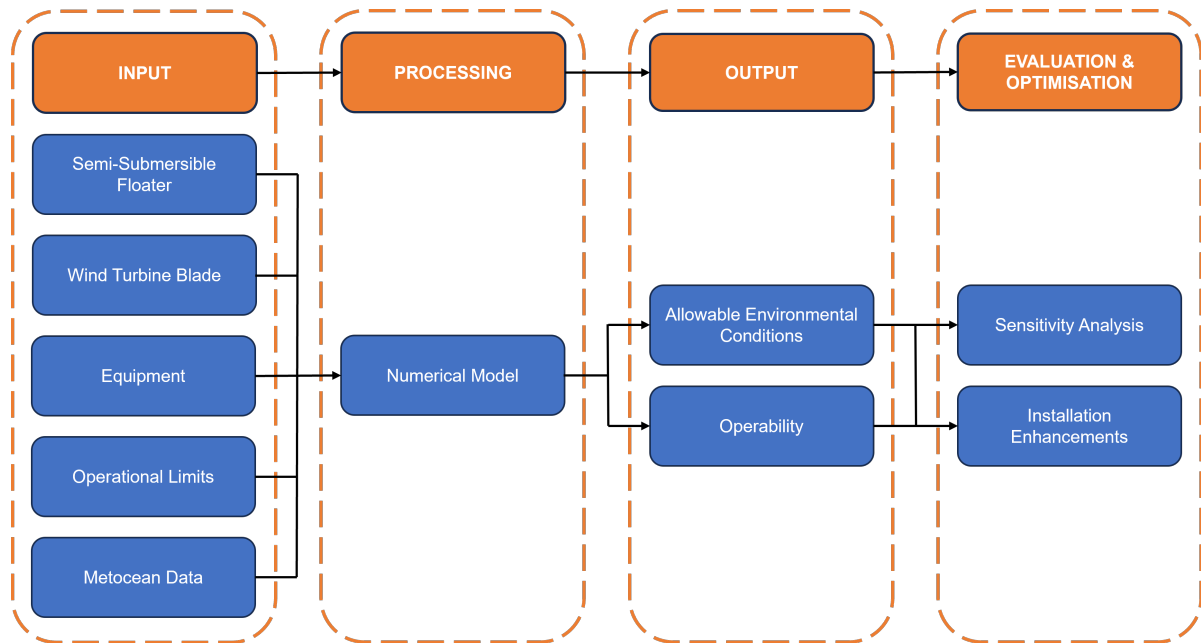


Figure 1.8: Overview of research approach.

1.6. Report Outline

After this introduction, in chapter 2, a theoretical framework is given that covers important background information for the modelling. It considers relevant literature on hydrodynamic damping and the operational limits for a blade installation. In chapter 3 are the modelling assumptions and strategy presented, together with the input for the model. For example, the details of the floater and turbine are discussed. The core of the thesis focuses on the development of the dynamic model, including the 3D wave diffraction-radiation analysis, modelling of floater and blade motions, determination of allowable environmental conditions, and the final operability study. This is described in chapter 4. Thereafter, the results are presented in chapter 5 which includes sensitivity studies on parameters like quayside distance and nacelle heading. It also provides the operability assessment for different installation strategies and locations. Operability improvements are also presented in this chapter. Finally, the conclusion and recommendations for future research are made.

2

Theoretical Framework

Theoretical background information, that is deemed necessary for calculating the operability of the blade installation, is presented in this chapter. Understanding the dynamic behaviour of the considered floating foundation is a critical factor for analysing the installation of a wind turbine blade. For this research, only wave loads are considered for external loads on the floating foundation, hence these are described in more detail. Additionally, the hydrodynamic damping is crucial to understand, as it is likely to have a large contribution to the floater dynamics. For the blade motions, only wind loads are considered as environmental loads. Hence, this is also considered in this chapter. Furthermore, it is important to understand the limiting mechanisms of the blade installation and the corresponding limits. This will also be discussed in this chapter. Finally, the software that will be used during this research will be presented and explained.

2.1. Waves Floater Model

Waves are important to consider for floating structures. These waves induce loads on the body that affect the structure's motions. The diffraction and radiation problem is introduced in this section, as this will be used for the analysis of the floater motions. Furthermore, a shallow water wave spectrum is discussed, as well as wave reflection on a vertical wall.

In regular waves, the hydrodynamic problem can be divided into a diffraction and a radiation problem. The diffraction problem considers the wave excitation loads on a body that is fixed in regular waves. While the radiation problem considers the forces that arise from forced oscillations of a body without incident waves. These loads are composed of added mass, damping and restoring terms (O. Faltinsen 1993).

In the diffraction problem, the wave excitation forces result from the interaction between a floating structure and the surrounding waves. These waves exert dynamic pressure on the structure, which can lead to a response of the structure. The wave excitation loads consist of two components: Froude-Kriloff forces and diffraction forces.

Froude-Kriloff forces arise due to the direct wave pressure on the submerged surface of the floating body. It assumes that the waves are undisturbed by the body. These forces are calculated by integrating the undisturbed wave pressure over the wetted surface of the structure. Furthermore, the diffraction forces, occur when the presence of the structure causes diffraction waves. This recovers the body's impermeability of the Froude-Kriloff forces.

In the radiation problem, there are no incident waves. Only generated waves due to forced body motions are considered. The added mass and wave radiation damping follow from harmonic body motions. Wave radiation damping is related to the ability of a floating body to generate outgoing waves by oscillating. Wave energy is radiated by the generated waves, which leads to an energy loss of the body and thus a damped motion. Oscillation frequency and body geometry are important parameters that determine the ability of the body to generate waves and therefore the damping coefficient. Mathematically,

radiation damping can be determined by calculating the velocity potential of the radiated waves. This velocity potential can be solved analytically for simple geometries, but in general, a numerical approach is more suited.

2.1.1. Wave Spectrum

The type of waves that are considered in this research are wind-generated waves, which are usually irregular. An irregular sea state can be represented as the superposition of multiple regular waves with different frequencies and phases. The distribution of the wave energy over the different wave frequencies can be represented by a wave energy spectrum. A fully developed sea state is described by the Pierson-Moskowitz spectrum, whereas a fetch-limited developing sea state is described by the JONSWAP spectrum. This spectrum is valid for a deep-water location and can be calculated as given in equation 2.1 (Holthuijsen 2007). It considers long-crested waves, so the waves propagate in one direction.

$$S_J(\omega) = A_\gamma \frac{5}{16} \cdot H_s^2 \omega_p^4 \cdot \omega^{-5} \exp \left(-\frac{5}{4} \left(\frac{\omega}{\omega_p} \right)^{-4} \right) \gamma^{\exp \left(-0.5 \left(\frac{\omega - \omega_p}{\sigma \omega_p} \right)^2 \right)} \quad (2.1)$$

Where, A_γ is the normalising factor, $\omega_p = 2\pi/T_p$ is the peak frequency, and σ is the spectral width parameter. The non-dimensional shape parameter γ can be obtained from a combination of significant wave height H_s and peak period T_p following the DNV guideline as in equation 2.2 (DNV-RP-C205 2021).

$$\gamma = \begin{cases} 5 & \text{for } \frac{T_p}{\sqrt{H_s}} \leq 3.6 \\ \exp \left(5.75 - 1.15 \frac{T_p}{\sqrt{H_s}} \right) & \text{for } 3.6 < \frac{T_p}{\sqrt{H_s}} < 5 \\ 1 & \text{for } 5 \leq \frac{T_p}{\sqrt{H_s}} \end{cases} \quad (2.2)$$

For a shallow water area, the JONSWAP spectrum is not applicable, hence a correction should be applied for the finite water depth. This correction results in the TMA spectrum (Holthuijsen 2007):

$$S_{TMA}(\omega) = S_J(\omega) \phi(\omega, d) \quad (2.3)$$

Where $\phi(\omega, d)$ is the transformation based on the ratio n of group velocity over phase velocity, wave number k , and the water depth d .

$$\phi(\omega, d) = \frac{1}{2n} \tanh^2(kd) \quad (2.4)$$

For a significant wave height of $H_s = 2$ m and a peak period of $T_p = 6$ s, the wave spectra and transformation function ϕ are presented in Figure 2.1 as an example of these spectra.

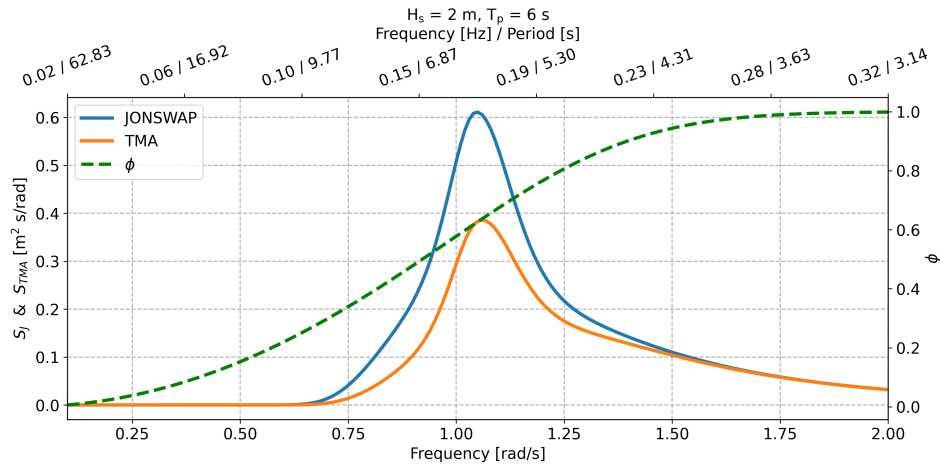


Figure 2.1: Transformation of the deep water JONSWAP spectrum into shallow water TMA spectrum.

It is likely that waves start breaking in shallow water. This is a non-linear process, and hence the results from this present study do not take this into account. The breaking wave height H_b of regular waves in an arbitrary water depth with a plane sea bed is defined as in equation 2.5 (DNV-RP-C205 2021).

$$H_b = \frac{0.892}{k} \tanh(kd) \quad (2.5)$$

An irregular wave field consists of multiple wave components that have different breaking wave heights. As a result, this equation is not applicable to irregular waves, instead, an empirical equation is required to calculate the breaking wave height of irregular waves.

2.1.2. Wave Reflections

When waves interact with a vertical wall in shallow water, they can be fully or partially reflected. This creates a (partially) standing wave pattern, which is the resulting wave profile of the incident and reflective wave. In the case of 100% reflection off the vertical wall, the waves are out of phase at the nodes and in phase at the antinodes. The wave height of the standing wave is minimised at the nodes and the wave particle orbital velocity is always horizontal, whereas it is always vertical in a propagating wave. Under an antinode, the standing wave height is maximised and the orbital velocity is always vertical, while it is horizontal under a propagating wave. Furthermore, the wave amplitude of the standing wave is double the amplitude of the incident wave.

In the more common case of partial reflection, the resulting wave is a combination of the incident propagating wave and partially standing waves. This creates a complex diamond pattern wave field, as can be seen in Figure 2.2. The maximum amplitude occurs at the quasi-antinodes where the incident and reflected waves constructively interfere. At the quasi-nodes, the minimum amplitude occurs because of destructive interference. All these reflections become more complex when there is a structure floating next to a vertical wall. Diffraction and radiation of the structure also have an influence on the wave field.

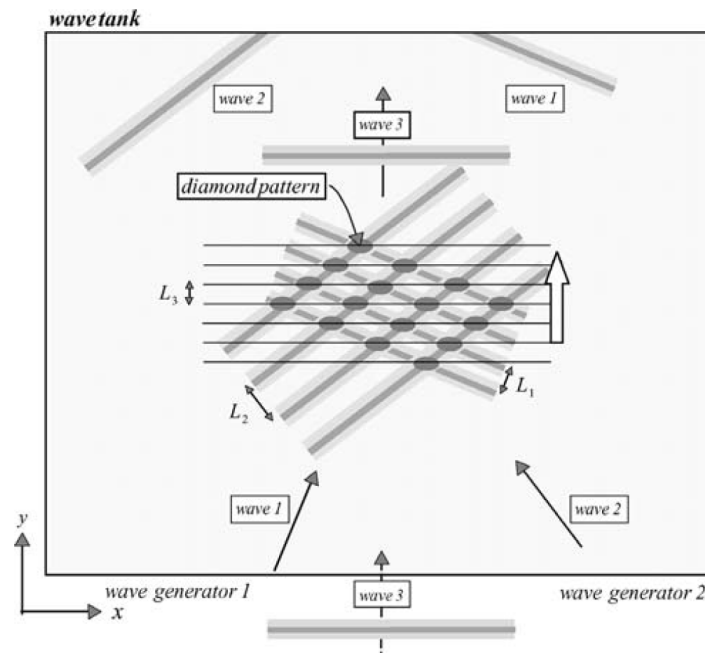


Figure 2.2: Example of diamond pattern for wave reflections.

Source: Holthuijsen 2007

2.2. Hydrodynamic Damping

Understanding damping is crucial in the analysis of floating structure motions, as it directly influences the response and performance of the structure in varying environmental conditions. Damping adds resistance in the direction opposite to the body's velocity. As a consequence, the amplitude of the body's oscillations is reduced. At the resonance frequency, the damping is largest, since the oscillations and body velocities are large. The resonance peak of a damped system is lower compared to an undamped system. Hydrodynamic damping of a freely floating structure arises from two mechanisms, namely wave radiation damping and viscous damping. The heave plates on the semi-submersible floater are designed to increase both the added mass and the overall damping, in particular viscous damping.

Viscous Damping

In the hydrodynamic analysis of viscous flow-body interactions, it is common practice to decompose the drag force on the body into two components: friction and form drag. Friction drag is independent of the Keulegan-Carpenter (KC) number, while form drag is linearly dependent on the KC number for $KC \sim O(1)$ (Tao and K. Thiagarajan 2003). The KC number represents the non-dimensional amplitude of oscillation. The main source for friction damping is the viscous shear stress on the floating structure's side walls that is in phase with the velocity. Form damping arises primarily due to flow separation and vortex shedding at sharp edges.

A commonly used method to attenuate vertical motions of spars and semi-submersibles is to add heave plates to the columns. One or multiple plates can be added to the column, either at the bottom or higher up. The additional heave plates increase the added mass and introduce extra damping. Flow separation and vortex shedding is enhanced due to the additional plates. Therefore, the hydrodynamic properties of the floater change by this extra damping and added mass (Tao and Cai 2004).

2.2.1. Heave Plate Damping

Multiple experimental and numerical studies have been performed to investigate the hydrodynamic behaviour of semi-submersible floaters with heave plates attached to the vertical columns. The effect of a variety of parameters, such as plate thickness and oscillation frequency, have been studied. These studies follow an approach that is commonly applied to investigate the damping and added mass of a

heave plate. This approach for determining the damping in heave with an experimental approach is described below (Zhang et al. 2023).

Obtaining the damping coefficient in heave motion of a cylinder with a disk attached to it, starts by considering a forced heave oscillation. The time series of this hydrodynamic force can be split in an added mass F_A and linearised damping force F_D , as presented in equation 2.6. This linearisation is necessary to include the non-linear drag force in a frequency domain model and remain computationally efficient.

$$M\ddot{z}(t) = -F_A(t) - F_D(t) - \rho g A_w z(t) + F_{33}(t) \quad (2.6)$$

Where,

$$F_A(t) = A_{33}\ddot{z}(t) \quad (2.7) \quad F_D(t) = B_{33}\dot{z}(t) \quad (2.8)$$

In these equations, M is the mass of the body, A_{33} is the heave added mass coefficient, B_{33} is the heave damping coefficient, ρ is the water density, g is the gravitational acceleration, A_w is the water plane area, and F_{33} is the external vertical force. Vertical displacement, velocity and acceleration are indicated by z , \dot{z} , \ddot{z} , respectively. Equation 2.6 contains only two unknowns (A_{33} and B_{33}) when these experiments are conducted, as the external vertical force is known during the experiment.

The equivalent linear damping coefficient has been derived by Sarpkaya et al. (1982) as:

$$B_{33} = \frac{1}{3}\mu\beta D_p C_D KC \quad (2.9)$$

In this equation is μ the dynamic fluid viscosity, D_p the heave plate diameter and β and KC are the non-dimensional frequency parameter and Keulegan Carpenter number, respectively.

$$\beta = \frac{D_p^2 f}{\nu} \quad (2.10) \quad KC = \frac{2\pi A_{osc}}{D_p} \quad (2.11)$$

where f is the frequency of oscillation, ν is the kinematic viscosity of the fluid, and A_{osc} is the amplitude of oscillation.

The heave added mass and damping coefficients can be made non-dimensional according to Lopez-Pavon and Souto-Iglesias (2015) as given in Equations 2.12 and 2.13. By making them non-dimensional, these coefficients can be compared with other heave plates.

$$A'_{33} = \frac{A_{33}}{A_{33,th}} \quad (2.12) \quad B'_{33} = \frac{B_{33}}{\omega A_{33,th}} \quad (2.13)$$

Where $A_{33,th}$ is the theoretical added mass of the heave plate and the column. This can be calculated according to Tao, Molin, et al. (2007) with the diameters of the column (D_c) and heave plate (D_p) as:

$$A_{33,th} = \frac{1}{12}\rho (2D_p^3 + 3\pi D_p^2 z - \pi^3 z^3 - 3\pi D_c^2 z), \quad z = \frac{1}{\pi} \sqrt{D_p^2 - D_c^2} \quad (2.14)$$

These non-dimensional coefficients will be used to derive the damping properties of heave plates based on experimental data from the literature.

2.2.2. Heave Plate Experimental Results

The non-dimensional hydrodynamic coefficients presented above can be used to compare different experimental results systematically with each other. This can be used to perform sensitivity studies of parameters that affect the hydrodynamic coefficients of heave plates. Multiple sensitivities on the effect of the non-dimensional added mass and damping are considered below.

Oscillation Amplitude & Frequency

Vu et al. 2004 studied an isolated heave plate with different KC numbers and oscillation frequencies. It was found that the damping coefficients linearly increase with the KC number. This indicates that higher oscillation amplitudes relative to the heave plate diameter lead to greater damping forces. Zhang et al. 2023 conducted similar experiments and found the same relation between KC number and damping. Additionally, the added mass also follows a linear increasing trend with the KC number. In contrast, it was found that the oscillation frequency has no significant effect on the added mass and damping coefficients. The heave natural period of the floater in this thesis is 17.4 seconds, which falls within the studied range of full-scale oscillation periods between 5.6 and 19.8 seconds. Hence, these experimental results are relevant for the current study.

Plate-Column Diameter Ratio

Zhang et al. (2023) also studied the effect of the diameter ratio between the heave plate and column, D_p/D_c . It was found that the damping coefficient is almost unaffected by the diameter ratio. A possible reason is that the damping is mainly caused by vortex shedding, which is not affected by a change in diameter ratios. The diameter ratio does have an impact on the added mass, where an increase in the diameter ratio results in a lower added mass. This effect becomes weaker as the ratio increases.

Plate Thickness

The impact of heave plate thickness has also been studied by Zhang et al. (2023), where the ratio plate thickness over plate diameter (t_p/D_p) is considered. The added mass is not significantly affected by the thickness ratio for low KC numbers. For larger oscillation amplitudes, a thinner plate has a larger added mass coefficient. The damping coefficient of a thin plate is larger for all KC numbers. However, this effect is small for thicker plates at low KC numbers. In this case, the thickness of the plate is large compared to the oscillation amplitude, and hence the vortices from both edges do not interfere with each other. This lowers the damping compared to a thinner plate where the vortex strength is enhanced (Tao and K. Thiagarajan 2003).

Plate Submergence

Experiments on heave plate submergence level for circular plates have been performed to study the effect (Wadhwa and K. P. Thiagarajan (2009)). A significant effect is noticeable between different drafts for both the added mass and damping. Different relative submergence (S/D_p) levels have been compared and the damping and added mass increase significantly when the plate is closer to the free surface. For the added mass show these experimental results a linear trend with the KC number, as discussed above. However, for the shallower drafts, this linear trend is broken above a certain critical KC number. Above this limit, the results are possibly incorrect and the behaviour is unclear.

Plate Perforation

Perforations (holes) in heave plates do have an effect on the damping generated by the plates. For low KC numbers, the damping is increasing with an increased perforation level (Molin et al. 2007). The optimum perforation density for generating maximum damping is approximately 10%. Above 20% is the damping lower compared to a solid plate. Similar results have been obtained for rectangular plates with perforation densities of 7.9% and 15.9% (An and O. M. Faltinsen (2013)). There is no increase of damping obtained by the higher perforation because the flow separation at the outer plate edges dominates over the flow through the holes. However, the added mass significantly reduces for higher perforation levels. This is caused by the fluid that flows easier through the perforations, instead of accelerating around the solid plate.

2.3. Wind Blade Model

In this section is the relevant theory discussed for the wind loads on the turbine blade. The formation of wind is introduced and the commonly used Kaimal wind spectrum is considered.

Aerodynamic loads on a structure are induced by wind. The wind is formed due to pressure differences in the earth's atmosphere. These pressure differences are caused by uneven heating of the air (Enel-Green-Power 0023). This effect is caused on a global and local scale, which makes wind very dependent on local conditions. Examples of wind-influencing mechanisms that determine the mean global atmospheric circulations are the global heating distribution and the Coriolis effect. These factors influence the dominant north or south wind direction and cause the deflection of wind to the left or right due to the Earth's rotation. On a local scale has the terrain a significant effect on the wind conditions. The heating of air varies over different types of terrain and elevations. Furthermore, the friction between air and the earth's surface affects the wind speed.

2.3.1. Kaimal Wind Spectrum

For engineering purposes, the randomly distributed wind speed and wind direction are the most interesting properties. The probability density function of rapid fluctuations in wind speed, i.e. turbulence, follows a Gaussian distribution. Where the 10 minute average horizontal wind speed is Weibull distributed. For extreme wind conditions, usually the Poisson and Gumbel distributions are used. Wind direction is strongly dependent on local circumstances, hence it does not follow a certain distribution. A circular histogram (wind rose) shows the historic wind orientation, which is useful if wind directions are considered.

A wind spectrum can be used to evaluate the wind conditions at a specific location. It provides insight into the energy distribution over different wind frequencies. The high-frequency part of the spectrum represents turbulence, while fluctuations in the mean wind speed are associated with the low-frequency end. A commonly used spectrum in the industry is the Kaimal wind spectrum, which is presented in equation 2.15 (Somoano et al. 2021).

$$S_{kaimal}(\omega) = \frac{4\sigma_u^2 L_u}{\bar{V} \left(1 + 6 \frac{\omega L_u}{2\pi \bar{V}}\right)^{5/3}} \quad (2.15)$$

Where ω is the frequency in rad/s, σ_u is the mean wind standard deviation, L_u is the integral scale parameter. The mean standard deviation and scale parameter can be estimated, according to the DNV standard (DNV-RP-C205 2021), as follows:

$$\sigma_u = \bar{V} \kappa \sqrt{4.5 - 0.856 \ln(z_0)} \frac{1}{\ln\left(\frac{z}{z_0}\right)} \quad (2.16) \quad L_u = 300 \left(\frac{z}{300}\right)^{0.46+0.074 \ln(z_0)} \quad (2.17)$$

Where z_0 is the terrain roughness and z is the height above the terrain, both in units of metres, and $\kappa = 0.4$ is the dimensionless Von Karman's constant.

$$S_{FwFw} = |H_{Fw} V_w|^2 S_{kaimal} \quad (2.18)$$

Examples of the Kaimal wind spectra for multiple wind speeds are shown in Figure 2.3. For this figure, the hub height of the turbine is used in combination with a roughness length of $z_0 = 0.001$ m, which can be used for coastal areas (DNV-RP-C205 2021).

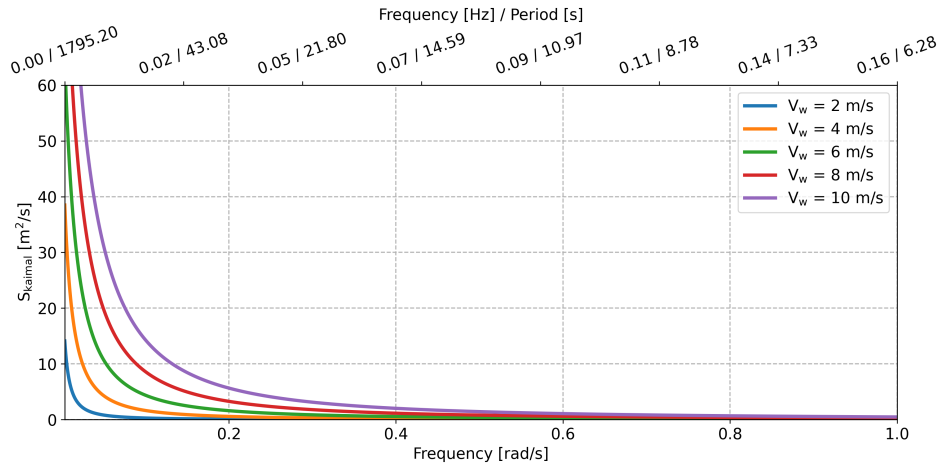


Figure 2.3: Kaimal wind spectrum for different wind speeds.

2.4. Single-Blade Installation Limit Criteria

The alignment and mating phases are considered as the two critical phases, as discussed in section 1.2. There are no standardised criteria that determine whether these critical phases can be executed successfully. It depends on the crew that performs the installation and whether they deem the situation safe for the operation. Since there is not much experience with the single-blade installation on a floating turbine, the environmental conditions should be favourable for the first installations. When a few installations have been executed successfully, the crew will gain confidence to install under slightly harsher conditions. This process of approaching the actual limit without exceeding it will continue to better define the operational boundaries. For the current research, fixed criteria are used to calculate the allowable environmental conditions and the operability. It should be noted that in practice, these criteria might deviate based on real-time assessments. The allowable limits can be used as a reference along with weather forecasts to plan the operation.

Limit Criteria Alignment Phase

During the alignment phase, the relative distance between the blade root and turbine hub should be small enough to start the mating phase. A perfect alignment is challenging because the blade and hub are moving with respect to each other. In practice, there is a cylindrical safety boundary, with radius R_{sb} and length L_{sb} , around the hub. Within this cylindrical boundary, it is possible to manually align the bolts with the flange holes. Figure 2.4 visually represents the cylindrical safety boundary. The distance between the centre of the blade root and turbine hub is represented by d_{hb} . Radial motions refer to the motions where the hub and blade root move parallel to each other (left of Figure 2.4). Axial motions refer to the motions where the hub and blade root move perpendicular to each other (right of Figure 2.4). Multiple exceedances of the safety boundary are allowed during the alignment phase. The limit of these number of exceedances is expressed as a total number of misalignments or a mean misalignment rate (ν^+) during the operation. Leeuw (2019) determined, together with a lifting supervisor, that the safety boundary radius is 0.2 m. Furthermore, the total number of misalignments between the hub and blade during a 30 minute operation is 30. This corresponds to a mean misalignment rate of one per minute, or $\nu^+ = 0.0167$ Hz. Different safety boundary and misalignment values are used in other studies. For instance, a safety boundary of 10% to 20% of the blade root radius has been applied in previous research (Zhao 2019). Additionally, a maximum misalignments rate of 10 per 30 minutes, or $5.6 \cdot 10^{-3}$ Hz has also been used (Jiang 2018).

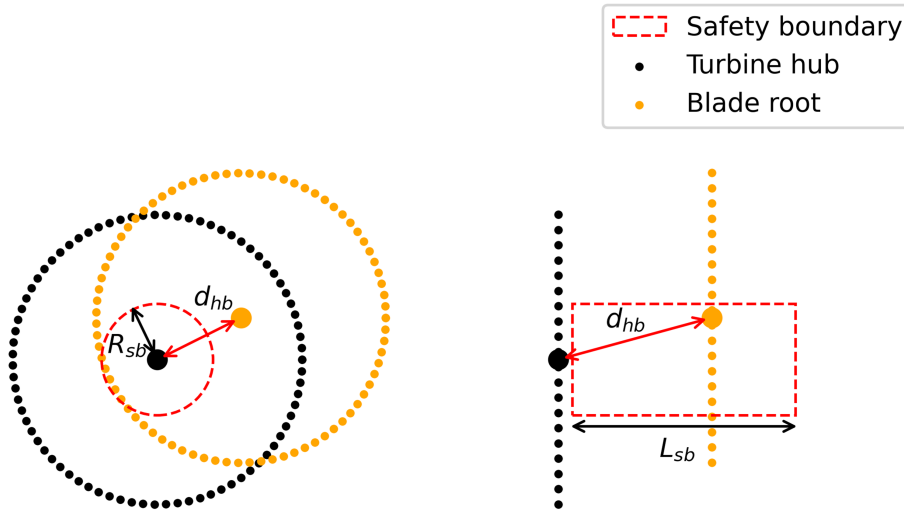


Figure 2.4: Sketch of the safety boundary in radial (left) and axial (right) planes.

Limit Criteria Mating Phase

During the mating phase, the longer guiding pins approach the hub closely. Hence, an accidental impact between the two components is likely to occur. There could be an impact in the axial or radial direction of the pins, as can be seen in Figure 2.5. Bolts are designed to deal with axial loads, so an impact in this direction is not expected to be critical. An impact in the radial direction where a transverse load is exerted on the guide pin is more critical. The bolt and root laminate are not designed to bear these loads. Therefore, a sideways impact will likely damage the bolt and the blade root, which cannot always be visually identified (Verma, Jiang, Vedvik, et al. 2019). The amount of damage is closely correlated with the impact velocity between guide pins and the hub, where plastic bending in the radial direction is more likely to occur than buckling in the axial direction (Verma, Jiang, Ren, et al. 2019). In all cases of damage, it is required to bring the blade back down to replace the damaged guide pins. For a relatively low impact velocity, it is possible to replace the pin and lift the blade for another trial. When the impact velocity is too high, the root laminate may be damaged and will require further investigation to determine if it can be used for another mating trial, needs to be repaired, or must be rejected.

The limiting radial impact velocity between the blade root and hub can be determined with an extensive structural study during the impact. This is out of the scope of this research, so this limit is based on available literature. Different load cases for a 10 MW wind turbine were examined with a non-linear finite element method. A maximum allowable radial impact velocity was found to be around 0.63 m/s (Verma, Jiang, Vedvik, et al. 2019) and 0.76 m/s (Verma, Jiang, Ren, et al. 2019). In the axial direction, the limit is found to be 1.35 m/s by Verma, Jiang, Ren, et al. (2019). At these limits, there is still damage to the guide pins and they need replacement before a new installation attempt can be made. To minimise the occurrence, a probability of 10^{-4} is used, following the probability of structural failure according to the DNV Marine Operations standard (DNV-OS-H101 2011).

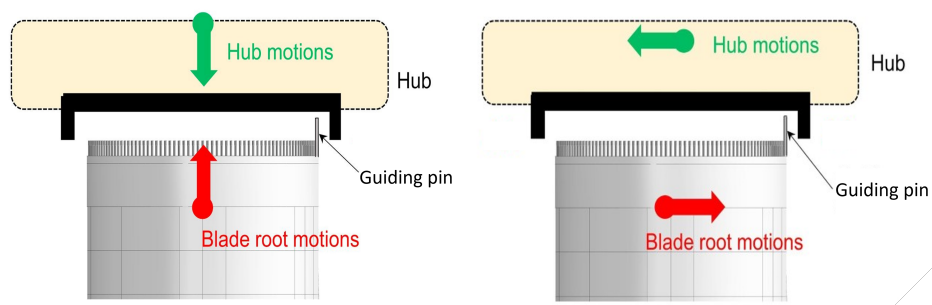


Figure 2.5: Sketch of the impact between hub and blade root in radial and axial planes.

Source: Verma, Jiang, Vedvik, et al. 2019

Table 2.1: Critical Events and Limiting Parameters

Installation phase	Critical event	Limiting parameter	Allowable limits
Alignment phase	Failure of aligning the blade and hub	Relative displacement	$R_{lim} = 0.2 \text{ m}$ $\nu^+ = 0.0167 \text{ Hz}$
Mating phase	Deformation of guide pins	Radial and axial impact velocity	$V_{lim,radial} = 0.76 \text{ m/s}$ $V_{lim,axial} = 1.35 \text{ m/s}$ $\Pr(V > V_{lim}) = 10^{-4}$

2.5. Software

For this research, multiple software programs have been used. An overview is presented in Table 2.2.

Table 2.2: Overview of used software for the research modelling steps

Modelling Step	Software	Version	Developer
3D Mesh	Rhino	8	Robert McNeel & Associates
Radiation & Diffraction Floater	WAMIT	7.5	Massachusetts Institute of Technology
Post-processing Blade motions	pyCalmot python		GustoMSC

2.5.1. Rhino

Rhino is a commercial 3D computer graphics software that is used in various industries, including architecture, industrial design, and engineering. It allows for visually designing 3D structures in a user-friendly interface. For this research, Rhino is mainly used for creating meshes of the Tri-Floater. It supports the WAMIT .gdf file format, which is required for the follow-up steps in the research. Examples of other software packages that could be used for free-form surface modelling are GeniE and SiemensNX. Rhino is selected as the software solution due to its availability within GustoMSC and its reputation for being relatively straightforward to learn.

2.5.2. WAMIT

WAMIT is a radiation/diffraction panel program developed by the Massachusetts Institute of Technology. It can be used for the linear analysis of the interaction between floating and submerged structures and surface waves. This involves solving the boundary value problem of the linear wave theory. It assumes potential flow, no flow separation or lifting effects. Furthermore, the free surface and body boundary conditions are linearised. This allows for the decomposition of the velocity potential into radiation and diffraction components. Which represents wave generation through forced oscillations of the body, and wave scattering due to its presence, respectively. The boundary value problems are solved by

using Green's theorem. It represents the velocity potential at various points on the body boundary and within the fluid as a set of integral equations. This velocity potential is expressed by a distribution of sources around the body surface and normal dipoles (Lee and Newman 2005). The wave-body interaction problem can be solved using this velocity potential. Irregular frequencies that arise because of a numerical issue, are removed by WAMIT throughout this research. More details about irregular frequencies are presented in appendix A. Comparable software packages are OrcaWave and ANSYS-AQWA. WAMIT is used for this study because it is the most compatible with pyCalmot.

2.5.3. pyCalmot

GustoMSC has developed an in-house software program, named pyCalmot. It processes the results obtained from WAMIT and it is used to solve the Equations of Motion (EOM) in the frequency domain and perform spectral analysis. With this software, it is possible to add additional mass, damping, and stiffness to the EOM to solve it with the correct system properties. It is capable of including linearized viscous damping of cylinders and plates based on its dimensions and drag coefficient. This is based on the recommended procedure for calculating roll damping, by the International Towing Tank Conference (ITTC - Recommended Procedures and Guidelines 2011). The software takes the geometry of the structure and the relative velocity between the structure and water particles into account. All in all, this makes pyCalmot a useful tool for analysing the floater motions.

Modelling Strategy & Model Input

This research is aimed at determining the operability of a single-blade installation on a semi-submersible floater. This chapter presents the assumptions used in the analysis, followed by a detailed modelling strategy to obtain the operability. Additionally, the initial input parameters for the operability calculations are provided.

3.1. Model Assumptions

The motions will be modelled in frequency domain, which has the implication that only linear (or linearised) effects can be considered. Furthermore, only steady-state conditions are considered, so there is no time varying behaviour of the system. The other assumptions are divided into operational, floater modelling, and blade modelling assumptions.

Operation Assumptions

The following assumptions have been made for the installation operation:

- Installation of the first blade is considered, so there are no other blades pre-installed on the turbine hub.
- Safety factors for the operational limits are assumed to be one. However, it is essential to include a higher safety factor to account for uncertainties in the modelling and operations in practice.
- The sea state is a stationary random process (DNV-RP-C205 (2021)). The standard time interval is three hours for a sea state to be stationary, this is longer than the blade installation time. So this is a valid assumption.
- Wind conditions are stationary during the operation. According to the DNV standard (DNV-RP-C205 2021), the wind climate can be assumed to be stationary for a ten-minute period. The installation operation will not be executed during extreme wind conditions, hence non-stationary conditions are not likely to occur.
- Wind and waves are uni-directional and are aligned. This is a simplification because, in nature, wind and waves do not always have the same direction.
- The blade and floater move independently from each other. In practice, the wind that flows around these components will affect the other.
- The reference period T_R for the blade installation is 30 minutes.
- Blade installation can not be executed for wind speeds above 10 m/s (Ummels 2024).

Floater Modelling Assumptions

The following assumptions have been made for modelling the floater motions:

- The semi-submersible floater, turbine tower, and nacelle are rigid bodies and rigidly connected. Hence, it can be modelled as one rigid body. It implies that the point of interest at the hub remains at a constant distance from the COG.

- 3D linear potential theory is used to describe the waves.
- Only first-order wave loads on the floater are considered. Mean wave loads are assumed to be counteracted by mooring fenders that are present in practice.
- The floater is freely floating in 6 DOF. Hence, no restoring forces or additional damping from a mooring system is considered.
- A constant water depth of 12 m is used.
- The floater is oriented such that the turbine is closest to the quayside.
- Wind loads acting on the floater, turbine tower, and nacelle are neglected. Therefore, the loads on the floater and blade are separated.
- Current loads acting on the floating foundation are neglected.
- The quay is a long vertical wall that reflects waves perfectly.
- The change of COG due to rotation of the nacelle is small, and hence neglected.

Blade Modelling Assumptions

The following assumptions have been made for modelling the blade motions:

- The crane is assumed to be rigid and fixed, which neglects additional motions induced by oscillations of the crane. Hence, the crane is not considered in the model.
- The yoke grips the blade in an orientation where the chord line is vertical.
- The blade is rigid, which ignores the nonlinear effect that bending of the blade has on the change in wind load.
- The blade is a point mass that follows a simple pendulum motion in two DOF. It follows a pendulum motion in the radial and axial direction of the blade. The blade remains horizontal (no roll) and does not rotate around the vertical axis (no yaw).
- The blade is lifted directly above its COG. This will limit the rotations under its weight. However, the COG does not necessarily coincide with the centre of the aerodynamic load, so rotations due to wind are assumed to be neutralised by the taglines.
- The COG and centre of aerodynamic load coincide, so rotations due to wind are assumed to be negligible. In practice, these points are not likely to coincide.
- A passive tagline is approach is used. Applying pre-tension to the taglines allows them to be modelled as springs that operate in both tension and compression. However, this is a simplification, as the stiffness in the taglines is greater than what can be achieved by the added stiffness from the pre-tension.
- Aerodynamic damping of the blade is included based on the relative velocity.
- The cable between the yoke and the crane tip is massless.
- The drag coefficient in the axial direction is calculated for a cone with a small half-vertex angle. This coefficient is applied to both the blade's root and tip side, even though the root side is more blunt.
- The tagline's properties remain constant for a variation of lifting arrangements. This is a simplification, as in practice the distance between the blade and crane jib changes with the lifting radius. A change in tagline length alters its stiffness.
- The blade root and hub motions are assumed to be always out of phase. This is a conservative approach because the relative motions between these components are largest when they are out of phase.
- Only the horizontal component of the wind speed is considered.

3.2. Modelling Strategy

As described in section 1.3, operational limits are used in combination with on-site environmental conditions to determine the workable weather window and operability. These operational limits are based on critical events and can be expressed in terms of allowable environmental conditions. A response-based approach is used to determine the allowable conditions for a successful installation.

The critical events and corresponding limiting parameters are defined in section 2.4. For the current research, two mechanisms are considered that can cause the installation to fail. The first critical event is the failure to align the hub and blade during the alignment phase. Here, the limiting parameter is the relative displacement between the blade root and the hub in the radial and axial directions. The alignment phase has failed if this relative displacement is too large. The second critical event is the plastic deformation of guide pins in the blade root during the mating phase. Impact velocity and guide pin bending are closely related, hence the limiting parameter is the radial and axial impact velocity between the blade root and hub. With the critical events identified, the modelling strategy is developed to incorporate both events. A schematic overview of the modelling strategy for calculating the operability is presented in Figure 3.1.

Under the assumption that the floater and blade motions are independent of each other, their motions are calculated separately. As a starting point for modelling the floater motions, a 3D panel model of the submerged semi-submersible floater is created in a 3D modelling program. This panel model can thereafter be used as input for the 3D diffraction & radiation model. This results in the frequency-dependent added mass, wave radiation damping, wave excitation force, and hydrostatic stiffness.

In the second modelling step, these intermediate results are implemented in the floater's EOM and solved in frequency domain to obtain the displacement and velocity RAOs. Additional viscous damping is calculated iteratively and then used as input in the EOM to obtain a more accurate representation of the floater's behaviour. Since the motions at hub height are of interest, the RAOs at the COG are translated to obtain the motion RAOs at the hub. The displacement RAO is necessary to calculate the allowable environmental conditions during the alignment phase. While the velocity RAO is used to obtain these allowable conditions during the mating phase.

The third modelling step is aimed at calculating the characteristic hub motions that correspond to specific sea states. For both installation phases, a wave spectrum is used as input in combination with the RAOs from the previous step to obtain a response spectrum of the floater. Thereafter, the characteristic hub motions for the alignment and mating phase can be calculated from these response spectra based on the misalignment rate and the probability of exceedance, as explained in section 2.4.

The fourth modelling step is used to calculate the blade motions. The blade's EOM is solved in frequency domain to obtain the RAOs, using the blade and tagline properties. A blade motion response spectrum is calculated by combining the RAOs with wind spectra, from which the characteristic displacements and velocities can be obtained. Thereafter, these values are used as input for the calculation of allowable environmental conditions.

In the fifth modelling step, the allowable environmental conditions for both critical phases are calculated using the characteristic blade and hub motions from steps three and four. The operational limits in terms of relative displacement and velocity are compared with the blade motions. The difference between them defines the allowable motions for the hub. From these allowable motions follow, for both phases, the allowable environmental conditions in terms of wave peak period, significant wave height, and mean wind speed.

In the final step, the lowest allowable environmental conditions from the alignment and mating installation phases are taken as the overall operational limits. Using site-specific metocean data, suitable installation windows are identified, during which the significant wave height, peak period, and wind speed fall within these allowable conditions. The operability is then calculated based on the number of these possible installation windows.

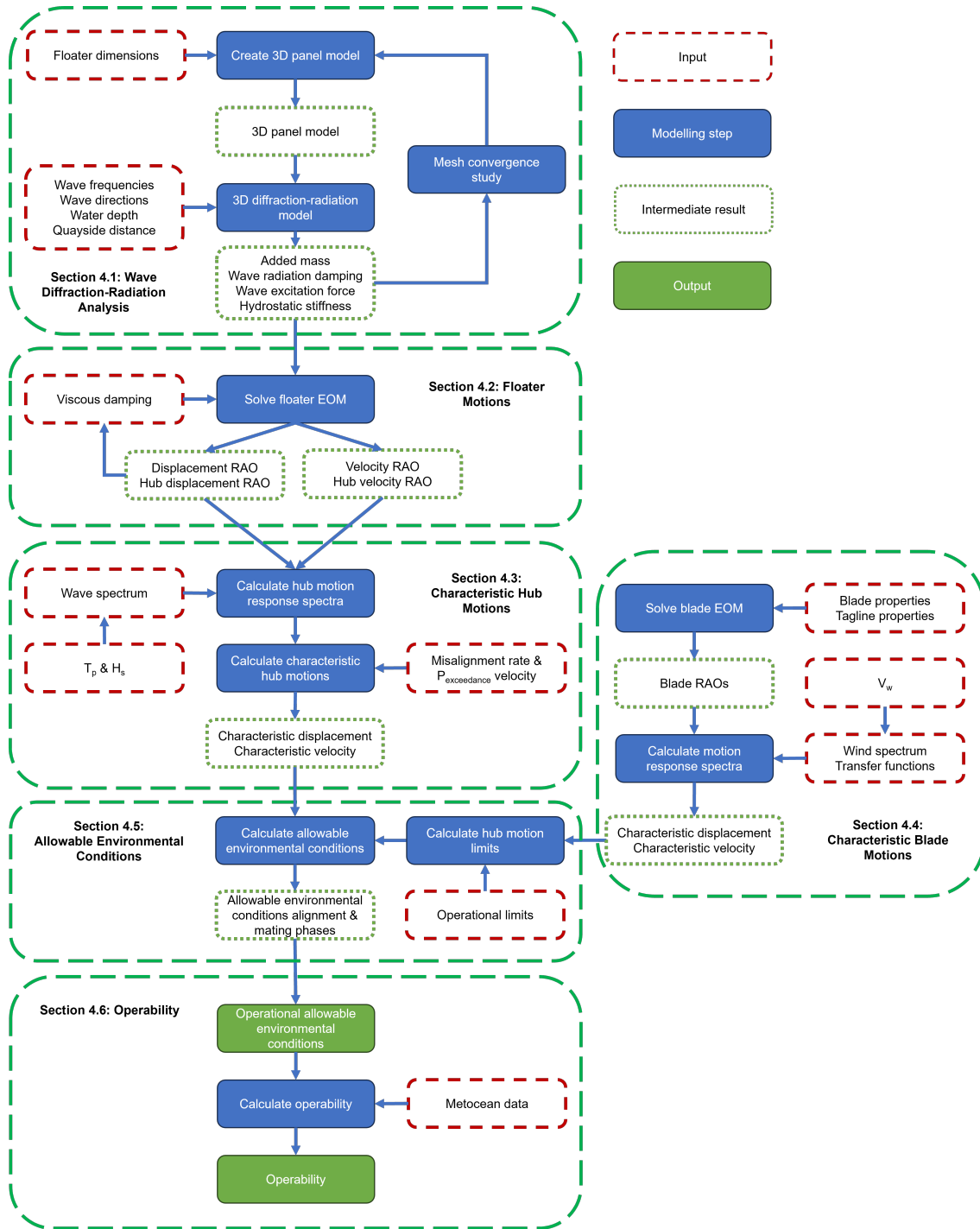


Figure 3.1: Flow diagram of the modelling strategy.

3.3. Coordinate Systems

The floater and blade are modelled separately, hence they are modelled as two distinct structures with six and two degrees of freedom (DOF), respectively. These motion components of the floater are given in Table 3.1 and can be seen in Figure 3.2. In this figure, the subscripts "f" and "b" refer to the floater and blade, respectively. Moreover, the two DOFs of the blade are pendulum motions in the radial and axial direction of the blade. In the axial direction, the motion is described by the angle (θ_{ax}) with the vertical axis in the $y_b z_b$ plane. The motion in the radial direction is described by the angle (θ_{rad}) with the vertical axis in the $x_b z_b$ plane.

The three used coordinate systems are right-handed and inertial reference frames. The global coordinate system has its origin at the quayside, with Z positive in the upward direction. X and Y are defined as perpendicular and parallel to the quayside, respectively. The coordinate system associated with the blade has its origin at the crane tip, which is the point of contact of the pendulum. Here Z_b is positive upwards, X_b is positive in the blade's radial direction, and Y_b is positive in the axial direction towards the blade root. When the blade is installed parallel to the quayside, the global and the blade's coordinate systems are aligned. However, for an altered installation orientation this is not necessarily true. This also applies to the floater-associated coordinate system, wherein the presented layout, the axes X_f , Y_f and Z_f are aligned parallel to the global coordinate system. The origin is located in the mean position of the floating body's COG.

Furthermore, Figure 3.2 also presents the wave and wind directions β , which are assumed to be aligned. These directions are defined by the positive rotation in a right-handed system. Hence, the quayside is limiting the incoming wave directions from 90° to 270° .

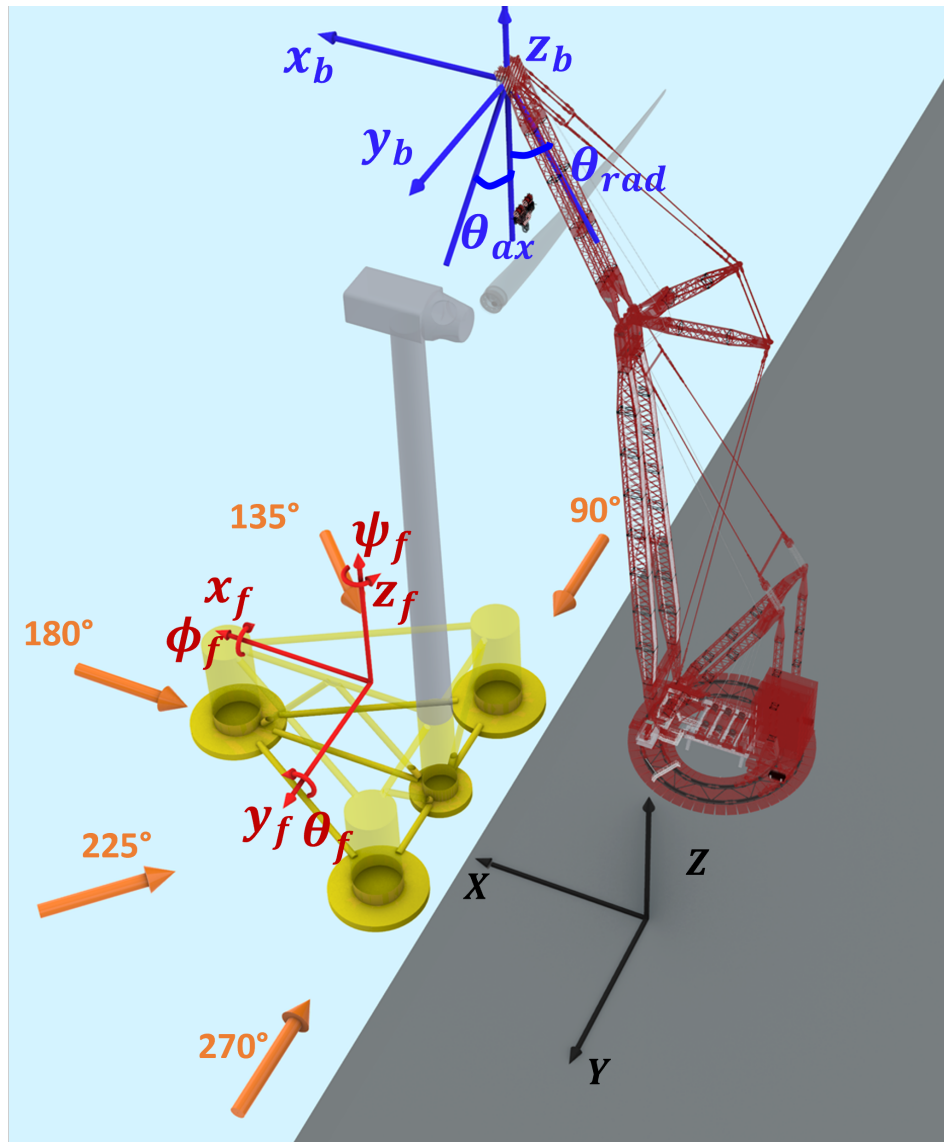


Figure 3.2: Overview of the coordinate systems and the wave directions.

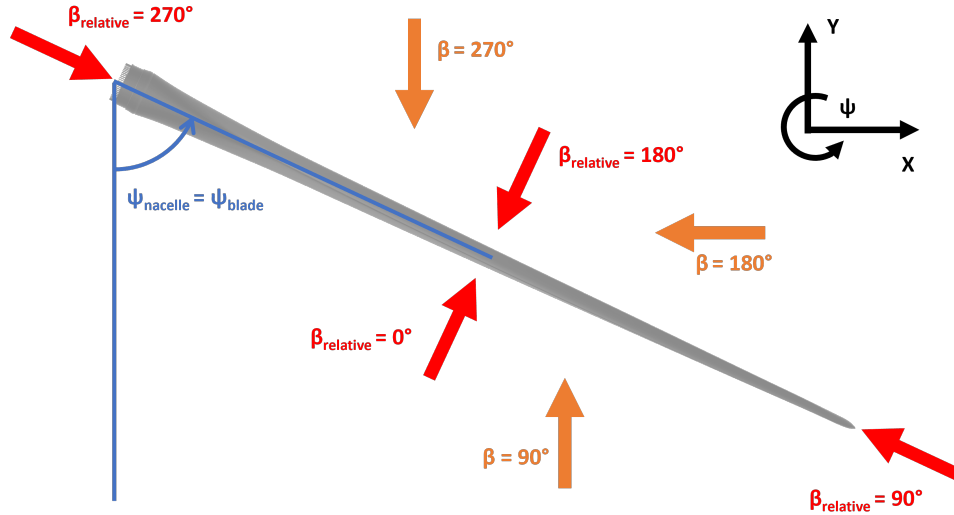
Table 3.1: Motion components of the floater

Description	Name	Symbol
Translation along x-axis	Surge	x_f
Translation along y-axis	Sway	y_f
Translation along z-axis	Heave	z_f
Rotation along x-axis	Roll	ϕ_f
Rotation along y-axis	Pitch	θ_f
Rotation along z-axis	Yaw	ψ_f

3.3.1. Relative Wind Directions

The nacelle on the turbine tower and blade suspended from the crane can be rotated around a vertical axis in the global reference frame with an angle $\psi_{nacelle} = \psi_{blade}$. These headings are the same, as it is assumed that the turbine hub and blade root are always parallel to each other. Figure 3.2 shows a nacelle and blade heading of $\psi_{nacelle} = 0^\circ$.

In chapter 5, different nacelle and blade headings will be studied. A relative wind and wave direction is required for an alternated nacelle heading, which is defined as $\beta_{relative} = \beta - \psi_{nacelle}$. Figure 3.3 shows how the relative wind and wave direction is defined with respect to the blade. Where β is the wind and wave direction.

**Figure 3.3:** Relative wind & wave directions for blade & nacelle headings.

3.4. Model Input

Three primary components are considered in this study: a semi-submersible floater, a wind turbine, and a ring crane. The relevant properties of these components are described below.

3.4.1. Semi-Submersible Floater

The floating foundation that will be considered during this research is the Tri-Floater designed by GustoMSC (GustoMSC 2024). It is a semi-submersible floater with three circular buoyancy columns in a triangular shape with an extra column on one side to support the turbine. In between the vertical columns, horizontal and diagonal cylindrical braces are mounted. Circular heave plates, so-called damper-boxes, are positioned at the base of the columns to dampen the vertical motions. At the offshore location, the Tri-Floater is moored by catenary mooring lines. A rendered picture of the floater can be seen in Figure 3.4 to give an impression of the design when it is at the offshore site. According to GustoMSC the Tri-Floater has several notable characteristics. Firstly, it has a shallow harbour draft, which enables the turbine assembly in more harbours that are closer to wind farm locations. Moreover,

there is a passive ballasting system which reduces the need for monitoring and maintenance compared to active systems. Consequently, both maintenance costs and turbine downtime are reduced.

The main dimensions of the Tri-Floater are shown in Table 3.2. These dimensions are used as input for the 3D model.

Table 3.2: GustoMSC Tri-Floater dimensions

Parameter	Value	Unit
Length	93.8	m
Width	104	m
Column spacing	76	m
Buoyancy column (diameter \times height)	14×34.5	m
Centre column (diameter \times height)	10×34.5	m
Buoyancy column damper-box (diameter \times height)	28×2.5	m
Centre column damper-box (diameter \times height)	18×2.5	m
Braces (diameter)	2	m
Water plane area	556.7	m ²
Operational draft	20	m
Harbour draft	7.2	m

The turbine blade will be installed on the Tri-Floater, turbine tower, and nacelle assembly. Hereafter in this report, this assembly will be referred to as the 'floater assembly' or 'floater', for convenience. The floater assembly is ballasted to ensure it remains in an even-keel position. Assuming no additional blades are present, the loading conditions applicable to this ballasted floater assembly are outlined in Table 3.3.

Table 3.3: Tri-Floater, turbine tower, and nacelle loading conditions

Parameter	Value	Unit
Displacement	8443	t
Harbour draft	7.2	m
VCG	38	m
Radius of gyration for roll (k_{xx})	50	m
Radius of gyration for pitch (k_{yy})	50	m
Radius of gyration for yaw (k_{zz})	30	m
Natural period heave	17.4	s
Natural period roll	38.4	s
Natural period pitch	34.9	s

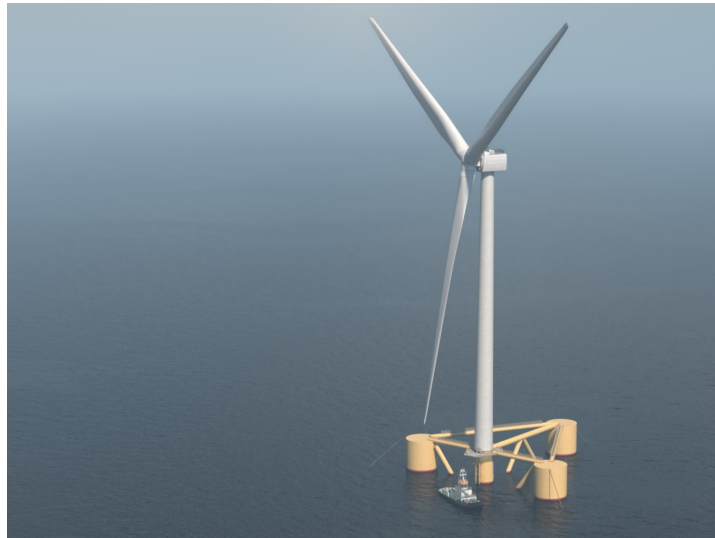


Figure 3.4: Tri-Floater impression.

Source: GustoMSC 2024

3.4.2. Turbine & Blade

In the research, the IEA Wind 15 MW reference turbine is considered. This turbine is designed by NREL, DTU and UMaine. It is developed to create a baseline for studies and it allows collaboration between the industry and researchers (Gaertner et al. 2020). The general parameters of the turbine and blade are presented in Table 3.4, where the blade's COG is given at a distance relative to the blade root.

Furthermore, the blade is constructed from airfoils of the DTU FFA-W3 airfoil family, of which the data is publicly available (Github 2024). Three crucial parameters for estimating the aerodynamic load on the blade are the lift and drag coefficients and the projected area perpendicular to the wind. The blade's geometry and drag coefficients for an angle of attack (AOA) of 90° are provided in appendix D. This corresponds to a wind perpendicular to the blade where the chord line is vertical. The lift coefficient for this AOA equals 0, so only drag is considered for the wind load. The drag coefficient in the radial direction for all the blade segments is estimated by interpolating between the provided airfoils. Combined with the projected area of these segments, the overall drag coefficient and projected area can be obtained. These values are also presented in Table 3.4. It should be noted that the blade's twist angle and pre-bend are not taken into account. This induces a small error in the projected area and AOA.

For the motions in axial direction, a drag coefficient of a cone with a small half-vertex angle is used. The diagram with the drag coefficient as a function of the half-vertex angle is presented in Appendix D.

Table 3.4: IEA Wind 15 MW turbine parameters

Parameter	Value	Unit
Power rating	15	MW
Blade root diameter	5.2	m
Hub height	150	m
Blade length	117	m
Blade mass	65	t
Blade COG	26.7	m
Blade projected area	477.4	m ²
Blade radial drag coefficient $C_{d,rad}$	1.28	—
Blade axial drag coefficient $C_{d,ax}$	0.214	—
Nacelle mass	821	t
Tower mass	860	t

3.4.3. Crane

The selected reference crane that will be used in this research is the Mammoet PTC 140-DS ring crane (Mammoet 2024). The properties of this crane are presented in Table 3.5. A ring crane is a type of crane characterized by a circular track that forms the base of the crane. Unlike most cranes that rotate around a narrow central spindle, the ring crane rotates along this broader circular track. This allows for rotating while carrying extremely heavy loads. Moreover, ring cranes have a large jib reach, which enables working over a larger area. A disadvantage is that this type of crane is rare, and hence expensive to use for projects.

Table 3.5: Crane properties

Property	Value	Unit
Boom length	140	m
Maximum jib length	84	m
Maximum lift capacity	3200	t
Maximum radius	172	m

According to Mammoet, the PTC 140-DS can lift up to 5000 t and has a high operating speed. This crane is selected for this research because of its high lifting capacity over a large radius, which enables the study of different installation arrangements. The crane's maximum lifting radius determines the maximum distance to the quayside for installation. From the crane's perspective, the blade installation is not the critical lift in terms of lift capacity for the WTG installation, since the tower and nacelle are heavier. Moreover, the nacelle has the same lift height as the blades. To avoid the relocation of the floater during the WTG installation, the maximum distance between the floater and the crane is determined by the nacelle and tower installation. Based on data from Mammoet (Mammoet 2024), a crane configuration with a 117 m boom length and a 84 m jib length is selected. A load of 874 t can be lifted at a height of 192 m over a maximum radius of 90 m in this specific configuration. Which is sufficient for the tower and nacelle installation. The blade's weight is significantly lower, hence it could be lifted to a height of 170 m over a radius of 130 m. This capacity is an estimation excluding safety factors, not an extensive calculation of the actual capacity.

Installation Site Arrangements

The selected crane configuration enables a range of possible installation arrangements, which alters the suspension length. Figure 3.5a depicts an overview of the installation site where the minimum and maximum distance between the floater and the quay are considered. These are $D_{quay} = 2$ m and $D_{quay} = 36$ m, respectively. For this variation alternates the suspension length between 50 m and 40 m, approximately. The distance between the crane and quayside ($D_{crane} = 20$ m), quay height ($H_{quay} = 20$

m), water depth ($d = 12$ m), floater draft ($T = 7.2$ m), and tagline length ($L_{\text{tagline}} = 21.5$ m) are kept constant for this study.

3.4.4. Yoke & Taglines

A yoke has the primary function of clamping the blade during the installation. Different types are available, which can hold the blade in different orientations. For the present research, a blade gripper is considered to hold the blade in a position where the chord is in vertical orientation. Furthermore, a weight of 100 t is considered for this yoke (Ummels 2024).

Two taglines are positioned between the yoke and crane boom that fulfil an important role in reducing the pendulum motions of the suspended blade that are induced by turbulent wind loads. They can be applied in a passive and active approach. Ren et al. (2023) studied an active control scheme that adjusts the tension forces on the taglines to stabilize the blade during different phases of the installation process. This study shows that active tagline control significantly reduces the blade motions and improves the installation performance compared to the passive approach. However, this active control scheme is out of this research's scope, so the passive approach is applied. In this approach, the taglines are shortened to induce pre-tension. This allows the potential energy of the blade to be stored in the tagline when it stretches. When the tagline is under compression, the energy is stored as gravitational potential energy. Therefore, a tagline can be modelled as a spring-damper system that is able to store energy in tension and compression.

Each of the two used taglines is made of Dyneema and has a stiffness and damping coefficient of 100 kN/s and 10 kNm/s, respectively. Moreover, the Minimum Breaking Load (MBL) is 24 kN, which equals a maximum elongation of 0.24 metres of the lines. These values are based on the research conducted by Leeuw (2019). The taglines are orientated horizontally and connected to each end of the yoke, to minimise the rotation of the blade around its vertical axis. An overview of the tagline configuration can be seen in Figure 3.5b. As presented in the figure, the taglines are not perpendicular to the blade, so they do have a small axial component which reduces the axial blade motions.

Table 3.6: Yoke & tagline properties

Property	Value	Unit
Yoke mass	100	t
Yoke length	18	m
Tagline material	Dyneema	-
Tagline length	21.5	m
Tagline diameter	16	mm
Tagline MBL	24	kN
Tagline stiffness	100	kN/m
Tagline damping	10	kNm/s

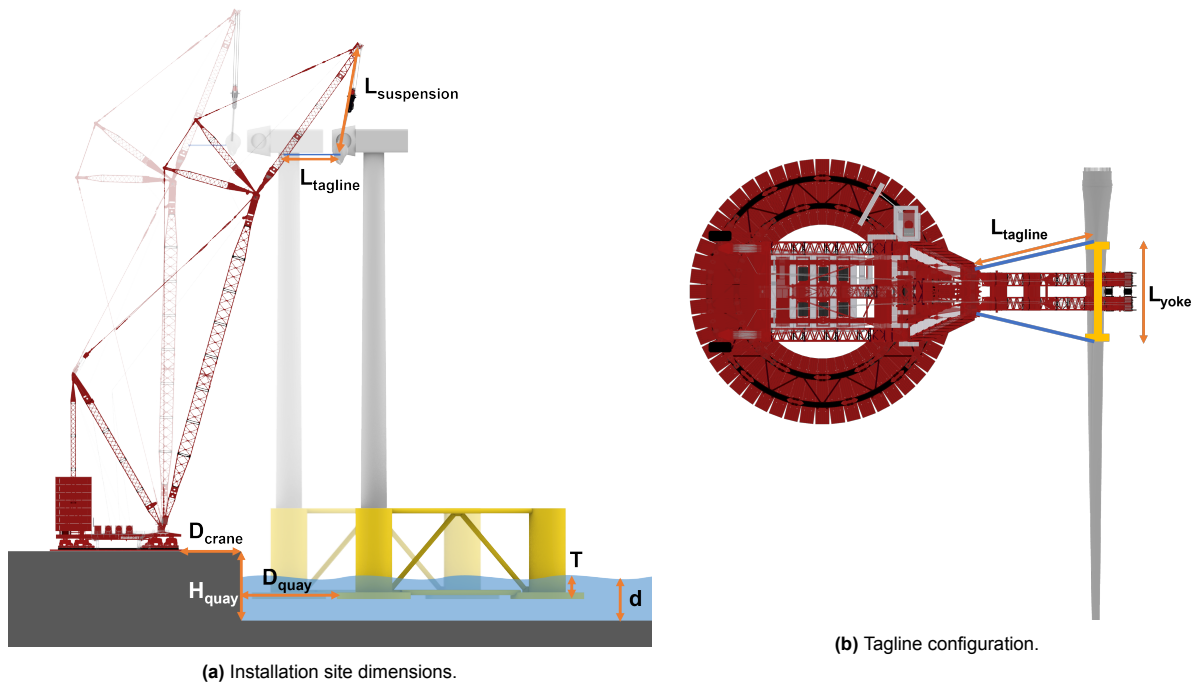


Figure 3.5: Overview of the installation site dimensions and the tagline configuration.

3.5. Metocean Data

Historic metocean data is required for the operability assessment. This data is highly location-sensitive. Historic metocean data is not always publicly available, especially for sheltered harbour environments with shallow water. This limits the possible reference location for this research. Useful data for this research is obtained at a sheltered and an exposed location in the port of Rotterdam. The sheltered location (L_s) is at the 'Hoek van Holland splitsingsdam', and the exposed location (L_e) is at the 'Maasmond' near 'Maasvlakte 2'. These locations can be seen on the map in Figure 3.6. Both locations have a shallow water depth, at L_s it is approximately 15 m (Rijkswaterstaat 2024), at L_e it is estimated to be around 20 m. It should be noted that these are hypothetical harbours for the installation, with the quay assumed to be oriented from north to south, placing the water to the west and the quayside to the east



Figure 3.6: Map with the sheltered and exposed locations in the port of Rotterdam.

Source: Municipality of Rotterdam 2014

For these locations, wave data are obtained from measurements, collected by the Ministry of Infras-

structure and Water Management. The wind data is obtained from the New European Wind Atlas which uses mesoscale modelling to calculate the wind conditions at different locations and heights in Europe (NEWA 2024). The key statistics for both locations are described below.

Table 3.7: Environmental conditions at a sheltered and exposed location

Property	Sheltered (Hoek van Holland)	Exposed (Maasmond)
Mean wind speed [m/s]	8.54	8.48
Std wind speed [m/s]	4.26	4.24
Mean H_s [m]	0.15	1.03
Std H_s [m]	0.09	0.57

Sheltered Location

The historical data of both the waves and wind at the sheltered area are presented in Figure 3.7. These measurements and modelled data are obtained between April 2005 and March 2010, with measurements every 30 minutes. The data shows vertical lines at higher periods because the provided frequency data were provided with only one decimal place. Hence, the significant figures of the period are low. Furthermore, it can be observed that the majority of the wave conditions have a peak period below 10 s and a significant wave height below 0.5 m. Figure 3.7b shows the wind rose that is based on historic data for wind at a height of 150 m. It shows that the dominant wind direction is west to southwest, which also gives the highest wind speeds. This is as expected since wind speed coming from the sea generally encounters fewer obstacles.

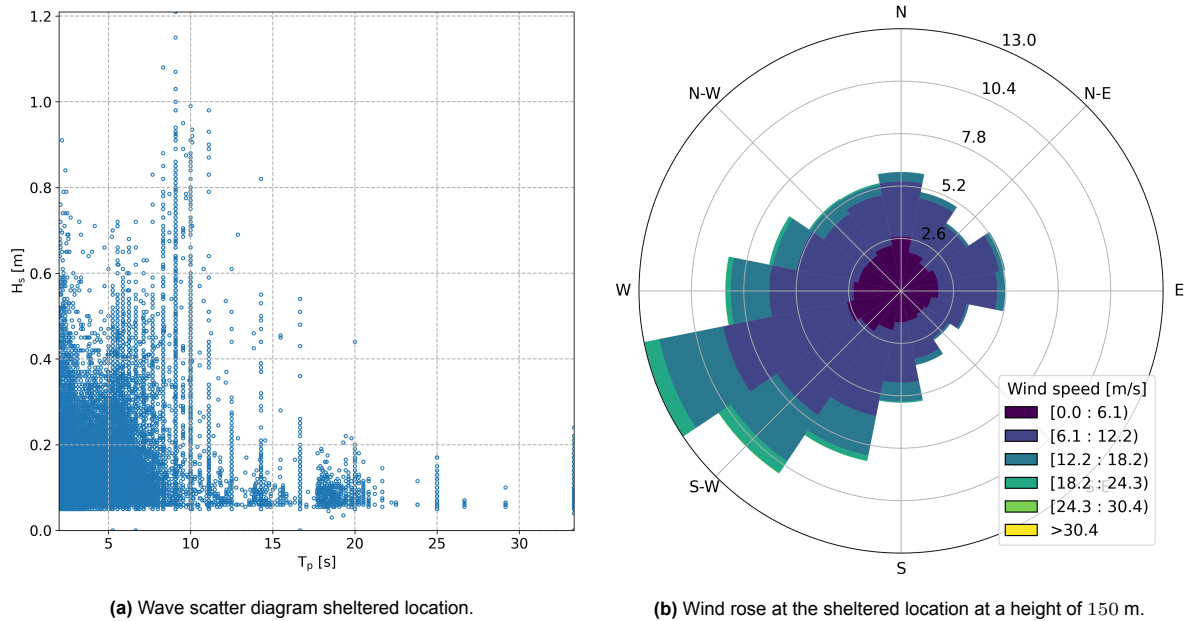


Figure 3.7: Historic wave and wind conditions at sheltered location.

Exposed Location

The measurements for this exposed location took place between January 2005 and December 2013. It can be seen that the significant wave height is higher compared to the sheltered location. On the other hand, there is no significant difference in peak periods. The wind speed conditions are almost the same as at the other location because these locations are close to each other.

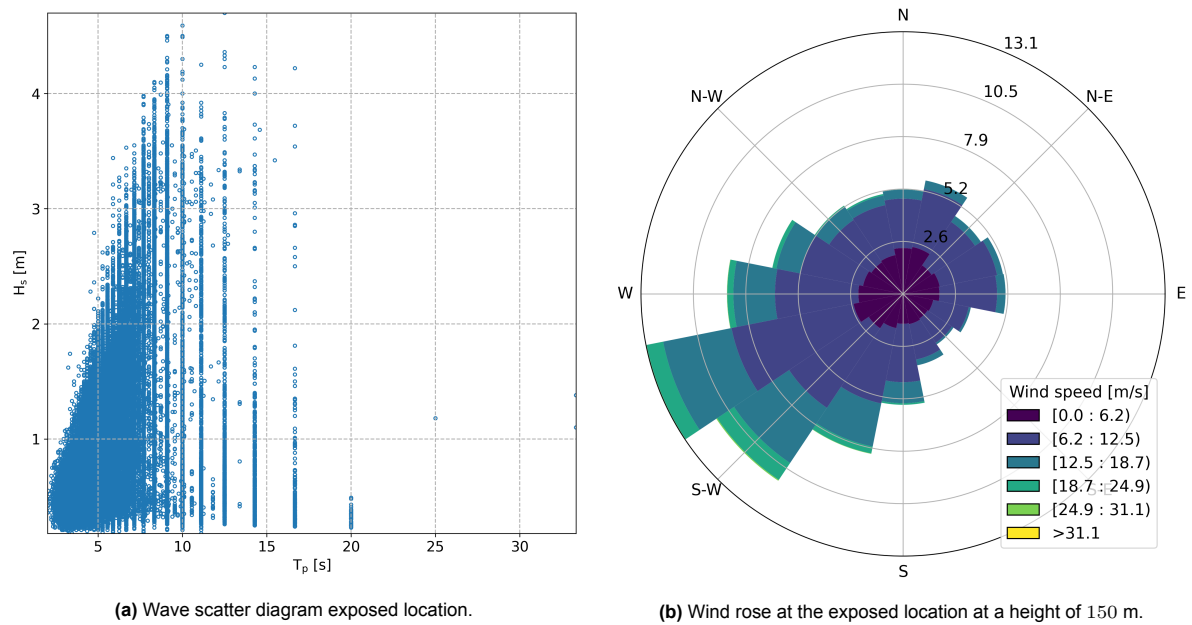


Figure 3.8: Historic wave and wind conditions at exposed location.

4

Dynamic Model

This chapter describes how the floating foundation and turbine blade are modelled to obtain the allowable environmental conditions and operability. The strategy as described in section 3.2 is followed and explained in more detail. The subsets of the complete modelling strategy correspond to the sections in this chapter. First, only the floater and hub motions are obtained in sections 4.1, 4.2, and 4.3. Thereafter, only the blade motions are calculated in section 4.4. Finally, the relative motions between the hub and blade are considered to obtain the allowable environmental conditions and operability in sections 4.5 and 4.6, respectively.

4.1. Wave Diffraction-Radiation Analysis

This modelling step is aimed at obtaining the added mass, wave radiation damping, first-order wave excitation force and the hydrostatic stiffness of the floater. Figure 4.1 shows an overview of this modelling step.

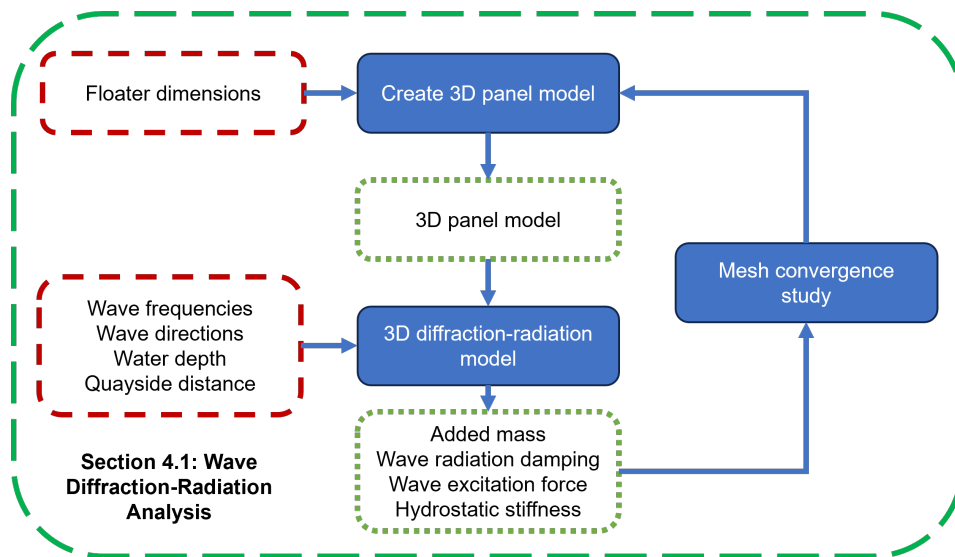
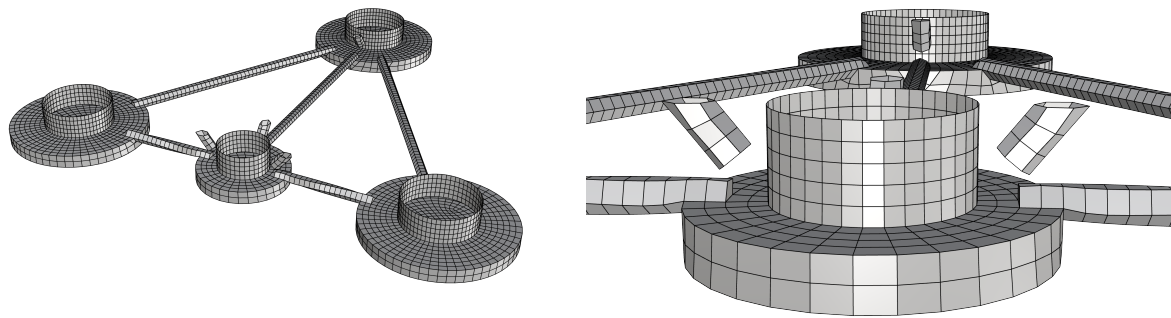


Figure 4.1: Modelling strategy wave diffraction-radiation analysis.

4.1.1. 3D Panel Model

The first modelling step is creating a 3D model of the submerged Tri-Floater in Rhino, where the dimensions presented in Table 3.2 are used as input. Radiation and diffraction software requires a panel (meshed) model of the body, up to the mean free-surface level, as input. Different meshes of the 3D

model have also been created in Rhino, so a mesh convergence study could be performed. An example of a mesh can be seen in Figure 4.2a. The floater design incorporates plates that establish a connection between the braces and columns. These plates are not modelled, since they are hard to capture in a mesh that is not very fine. This induces an error, as it slightly alters the hydrodynamic properties and reduces the wave excitation forces. However, these connections are small compared to the overall structure, hence it is assumed that this induced error is small and can be ignored. Figure 4.2b shows a highlighted part where the connections are missing.



(a) 3D mesh of the submerged Tri-Floater.

(b) Detail of Tri-Floater mesh.

Figure 4.2: Tri-Floater mesh model of its submerged part and mesh detail.

4.1.2. 3D Diffraction-Radiation Model

With the 3D panel model as input, WAMIT is used. Important input settings and parameters are:

- Wave frequencies in the range of $0.1 - 2.0$ rad/s. This is sufficient to capture the whole range of gravity waves.
- The quayside is included as a fixed vertical wall.
- The quayside limits the possible wave directions, hence a range of $90^\circ - 270^\circ$ is used.
- A finite water depth of 12 m is used.
- The distance between the floater and quayside is defined.
- The wave excitation forces are obtained from the diffraction potential (instead of Haskind relations).

The relevant WAMIT output for this research is the added mass, wave radiation damping, first-order wave excitation force RAOs, and hydrostatic stiffness. Based on these intermediate results, a mesh convergence study can be performed.

4.1.3. Mesh Convergence Study

To obtain consistent results, it is important to use a suited mesh size. A mesh with large elements has a low computational time but might give inaccurate results. On the other hand, a mesh with small elements is more accurate but requires more computational capacity and time. For the convergence study, a quayside distance of 4 m is used. This value is based on an educated guess that falls within the limits of the suitable distance and is sufficient for the mesh convergence study. The effect of quayside distance will be studied later. Furthermore, the irregular frequencies between 1.8 rad/s and 1.9 rad/s are ignored, because there is no convergence at this peak, as explained in Appendix A.

A preliminary study into meshes with triangular and quad mesh elements has shown that quad meshes require fewer elements (and calculation time) to obtain the same accuracy (appendix B.1). Hence, seven mesh sizes with a quad structure are used for this study. The meshes are described by the average edge length of all the mesh elements. The used mesh sizes are in the range of 1.8 m to 0.6 m.

m , where the latter represents the highest resolution mesh. These meshes are visualised in appendix B. This mesh size range is based on practical limits: larger elements cannot capture the braces of the floater, while smaller elements would take too long to run.

The added mass, potential damping and wave force RAO are calculated for all the meshes. The largest differences between the meshes are noticeable in heave, roll, and pitch. Figure 4.3 shows the normalised added mass in pitch for the seven different mesh sizes. The added mass in pitch is normalised by the water plane area A_{WP} and the floater's weight displacement ∇ . This weight displacement is calculated as $\nabla = \rho \Delta V$, where ρ and ΔV are the fluid density and the floater's displaced volume.

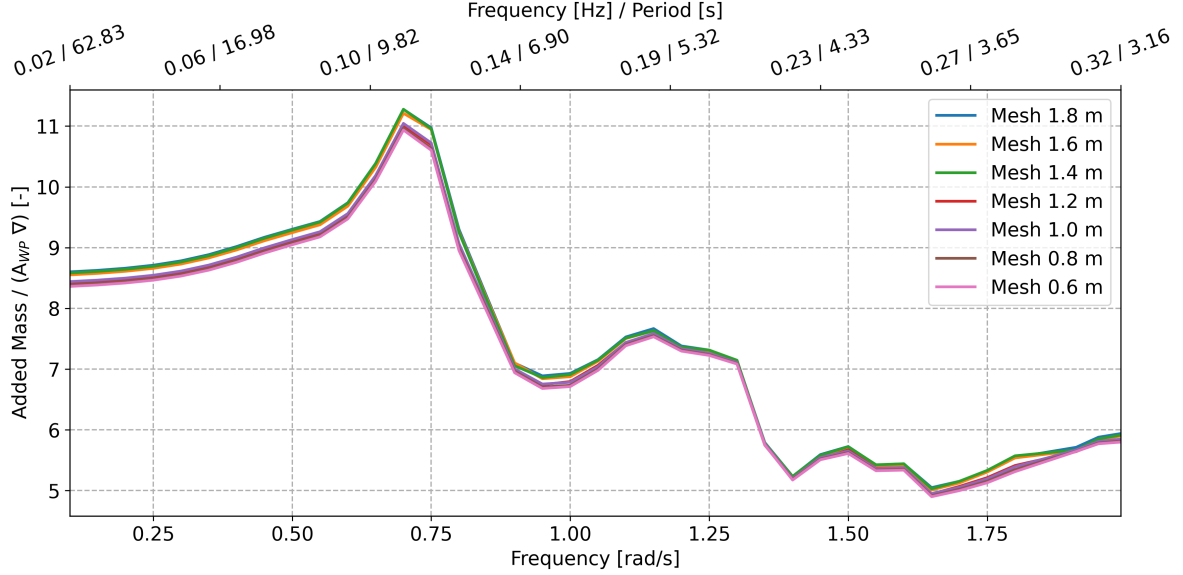


Figure 4.3: Normalised added mass in pitch direction for the seven meshes.

Similar figures for the other DOFs, added mass and wave force RAOs are made and presented in appendix B. The relative error for each mesh is calculated to get more insight into the accuracy of the different meshes. Therefore, it is assumed that the smallest mesh size (0.6 m) is the exact solution, and the other sizes are compared to this solution. With respect to the exact solution is the relative error calculated as follows:

$$\varepsilon_{rel} = \frac{|Y_{i,j} - Y_{0.6,j}|}{|Y_{0.6,j}|} \quad (4.1)$$

where $Y_{i,j}$ are the results for all the mesh lengths ($i = 1.8, 1.6, 1.4, 1.2, 1.0$, and 0.8 m) at every frequency j . The maximum relative error for the different meshes in heave, roll and pitch are depicted in Figure 4.4.

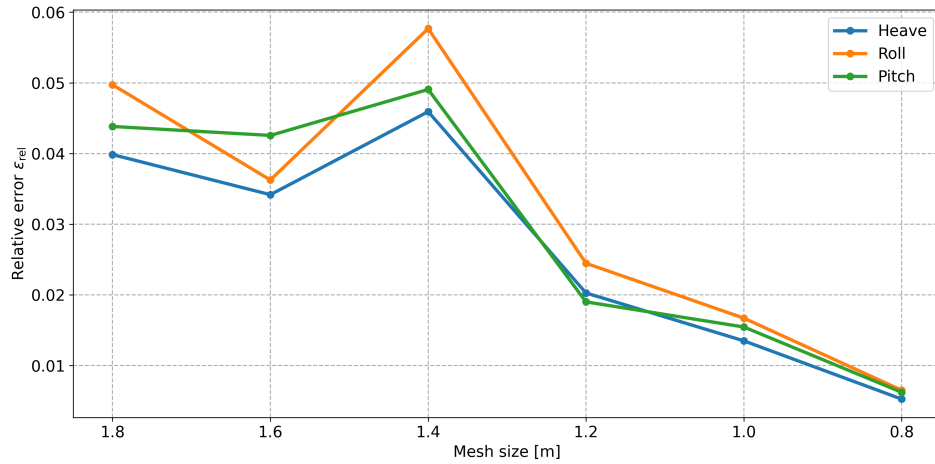


Figure 4.4: Maximum relative error of added mass in heave, roll and pitch for different mesh sizes.

It can be noticed that for larger mesh sizes, the relative error is alternating. This might be caused by the braces that can not be meshed correctly, which gives dents in the structure. The shape for a 1.6 m mesh could be more correct than the 1.4 m mesh, by accident. For smaller mesh sizes are the braces better meshed and the results more accurate, indicated by the decreasing error. The relative error in the three DOFs decreases to below 2% for mesh sizes up to 1.0 m. Based on the maximum relative error plot and the good accordance of the other results in appendix B, the 1.0 m mesh size is used for this research.

4.2. Floater Motions

The added mass, wave radiation damping, first-order wave excitation force, and hydrostatic stiffness results from the previous step are used in the next step to obtain the floater motions. First, the equations of motion are solved. Thereafter, it is possible to calculate the transfer functions from incoming waves to floater displacement and velocity. A translation of these RAOs to the hub is made. This modelling step is schematically presented in Figure 4.5

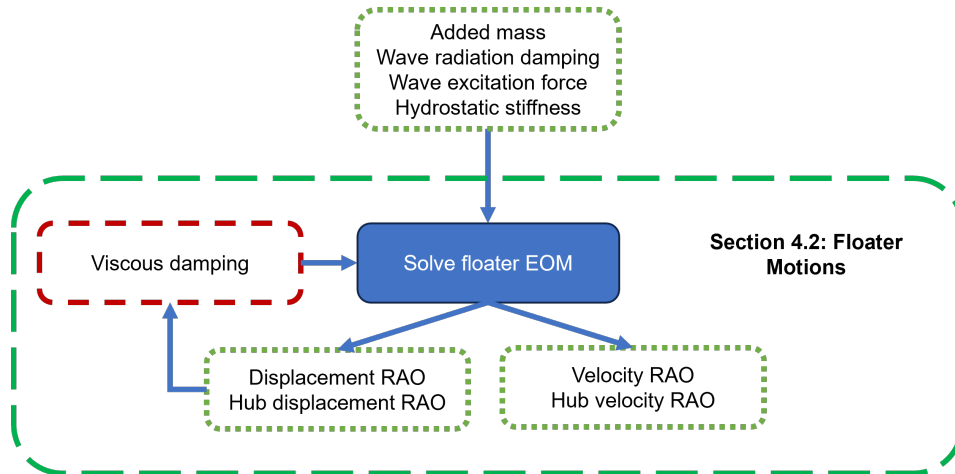


Figure 4.5: Modelling strategy floater motions.

4.2.1. Solve Floater EOM

The equations of motion are given in equation 4.2, where \mathbf{F}^{ext} is the external force matrix. Only the first-order wave excitation forces are considered as the external forces for this research, under the assumption that there are no wind, current, or mooring loads. Furthermore, \mathbf{M} the mass matrix, \mathbf{A} the

added mass matrix, \mathbf{B} the damping matrix, and \mathbf{C} the stiffness matrix. The body's motions, which are wave frequency (ω) and wave direction (β) dependent, are represented by the vector \mathbf{X} .

$$\mathbf{F}^{\text{ext}}(\omega, \beta) = -\omega^2(\mathbf{M} + \mathbf{A}(\omega))\mathbf{X}(\omega, \beta) + i\omega\mathbf{B}(\omega)\mathbf{X}(\omega, \beta) + \mathbf{C}\mathbf{X}(\omega, \beta) \quad (4.2)$$

The added mass, wave radiation damping, and first-order wave excitation force are the result of the wave diffraction-radiation analysis and are inserted in the EOM. Viscous damping effects are considered for the semi-submersible floater, so these are included in the equations. The extra damping is determined in an iterative process where the EOM is solved for every iteration, as described in section 4.2.3. pyCalmot is used as the software tool to solve the EOM.

Floater RAO at COG

Subsequent to solving the EOM, the solution can be used to calculate the Response Amplitude Operator (RAO) as follows:

$$RAO(\omega, \beta) = \mathbf{X}(\omega, \beta) [-\omega^2(\mathbf{M} + \mathbf{A}(\omega)) + i\omega\mathbf{B}(\omega) + \mathbf{C}]^{-1} \quad (4.3)$$

The RAO is a transfer function that gives the amplitude of the floater's response per unit wave amplitude, as well as the phase relative to the incident wave phase. It provides insight into the dynamic behaviour of a floating body in the different DOFs. As can be seen in the equation, the RAO is dependent on the wave direction and wave frequency.

The displacement RAOs for six DOFs are presented in Figure 4.6. Here the distance to the quayside is 4 m, and three wave directions ($\beta = 90^\circ$, $\beta = 135^\circ$, $\beta = 180^\circ$) are considered.

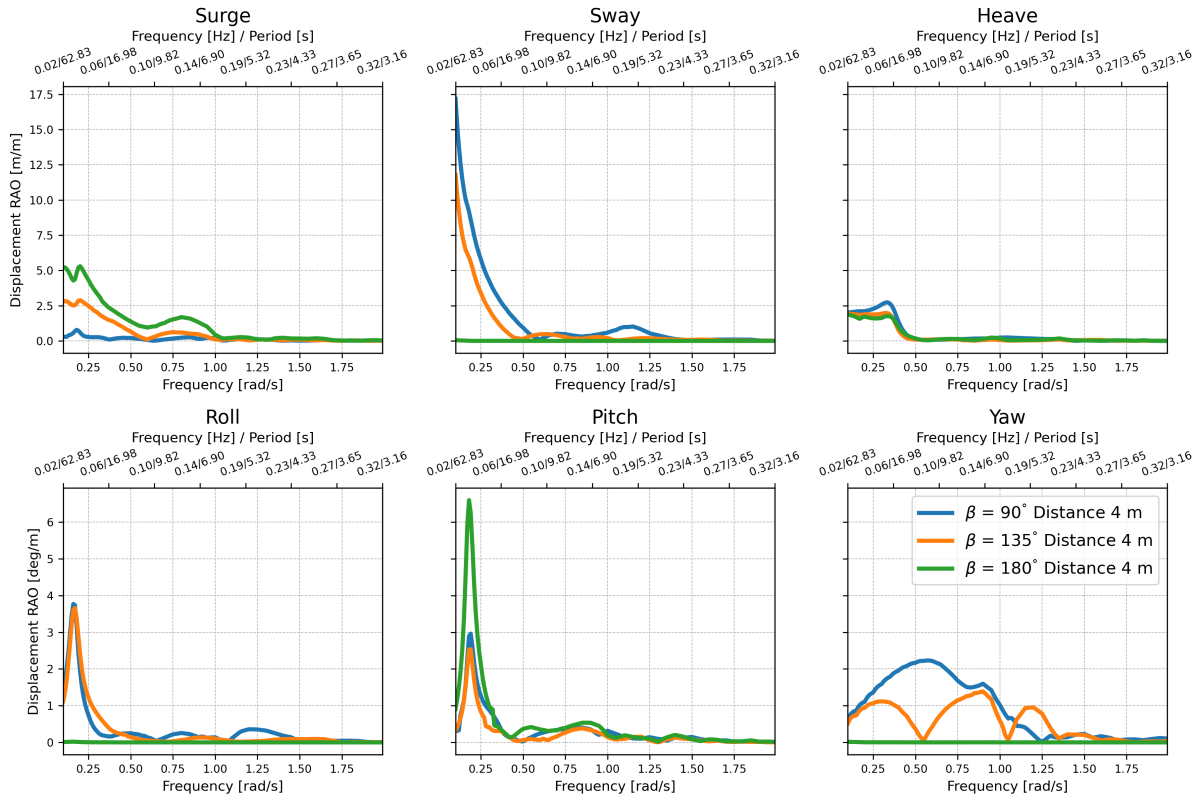


Figure 4.6: Displacement RAOs at COG in six DOF for three wave directions and 4 m quayside distance.

It can be noted that the peak of the RAOs in heave, roll, and pitch corresponds to the natural frequency, which are given in Table 3.3. Furthermore, there is almost no response in sway, roll, and yaw to waves that are perpendicular to the quayside ($\beta = 180^\circ$). This can be attributed to the floater's symmetry in

this direction, causing the motions on each side to cancel each other out. For this direction, the pitch is considerably larger compared to the other wave directions. When the waves are more parallel to the quay, there is a reduction in surge. Moreover, a significant increase in sway, roll, and yaw motions can be observed in this direction.

Floater RAO at Hub

The presented RAOs at COG are used to calculate the motions at any point P on the structure as in equation 4.4. This equation is valid within linear theory and uses translations and rotational effects to obtain the displacements at point P . A similar approach is used for transforming velocities to this point P .

$$\begin{pmatrix} x_P \\ y_P \\ z_P \end{pmatrix} = \begin{pmatrix} 1 & -\psi & \theta \\ \psi & 1 & -\phi \\ -\theta & \phi & 1 \end{pmatrix} \cdot \begin{pmatrix} x_{body} \\ y_{body} \\ z_{body} \end{pmatrix} \quad (4.4)$$

In the equation, the subscript 'body' represents the body's coordinate system with its origin at the COG. The coordinates are defined in section 3.3. The hub motions are relevant, so to calculate the motion response to waves, equation 4.4 is used to shift the RAOs from COG to the hub. The results are RAOs of the hub in X, Y, and Z directions.

Combined RAO at Hub

The hub RAOs, that are described above, give insight into the three directions the hub moves. However, for the blade installation, the relative motions between the blade and hub should stay within a cylindrical safety boundary. Therefore, the motions of the hub should be expressed in a radial and axial direction. The axial motion corresponds to the Y direction. The motions in the radial direction are the combined motions in the X and Z direction. To obtain the RAO in the radial (XZ) plane, the individual RAOs are combined as in equation 4.5. These RAOs should be represented in the complex domain to take the phases and amplitudes into account.

$$RAO_{XZ}(\omega, \beta) = \sqrt{RAO_X^2(\omega, \beta) + RAO_Z^2(\omega, \beta)} \quad (4.5)$$

The individual and combined RAOs at the turbine hub are shown in Figure 4.7 for a wave direction of $\beta = 90^\circ$ and a 4 m quayside distance. The motion in X direction follows from a combination of surge and pitch. In Figure 4.6, it can be seen that pitch has a larger contribution than surge for $\beta = 90^\circ$. Therefore, the peak in the X direction corresponds to the peak of the pitch RAO. The motion in the Z direction is mainly caused by the heave motion at the COG.

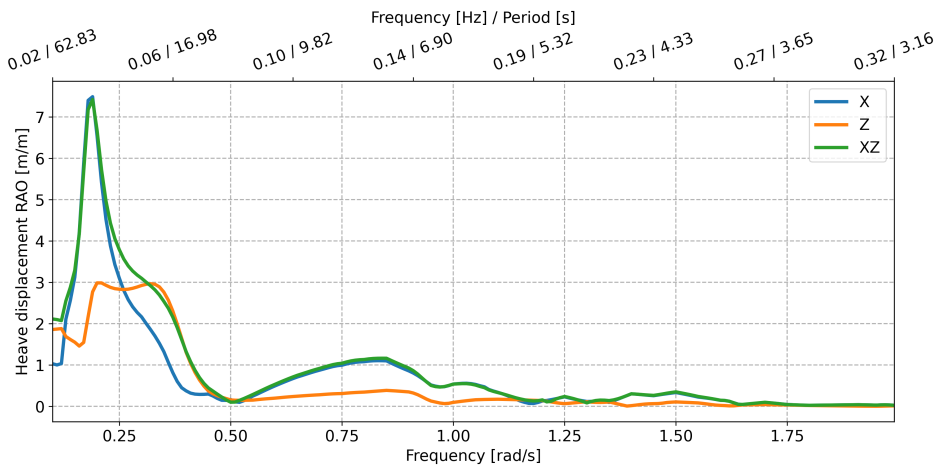


Figure 4.7: Displacement RAOs at hub in radial plane for wave direction $\beta = 90^\circ$ and 4 m quayside distance.

4.2.2. Shallow Water Effect

In this study, the floater is in shallow water, which has a significant effect on its behaviour. As a side note, the effect of the shallow water is evaluated based on first-order wave forces, added mass and displacement RAOs. A comparison is made between 12 m water depth and deep water. There is no quayside considered, and the draft of the floater is the same at 7.2 m. The first-order wave force RAOs and displacement RAOs for a wave direction of 135° are shown in Figure 4.9 and 4.8, respectively. This direction is plotted to see a response in all the DOFs, which gives insight into the effect of the water depth on the floater motions.

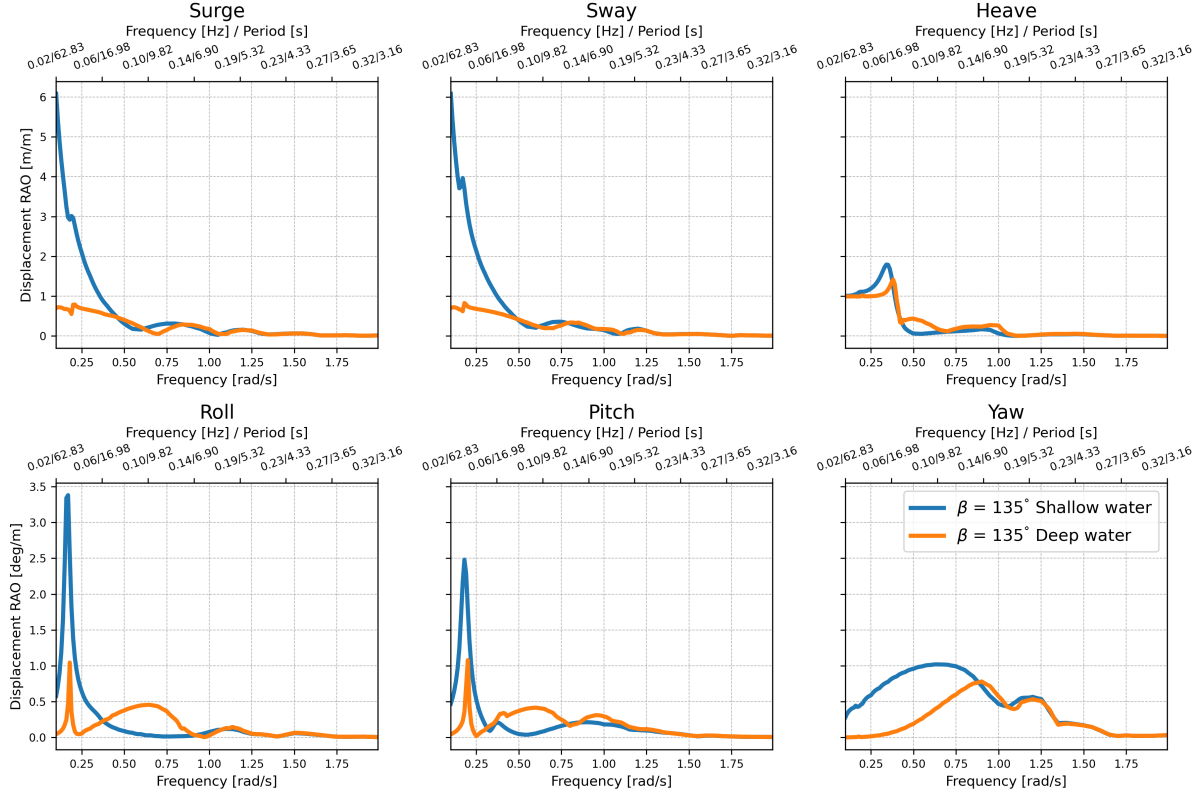


Figure 4.8: Displacement RAOs in six DOFs for deep and shallow water.

It can be seen that the water depth has no effect at higher frequencies because here the waves are short compared to the water depth. At lower frequencies, the waves are long and they ‘feel’ the seabed, which makes the wave-particle orbits more elliptical. This effect is noticeable by an increase in horizontal motions (surge, sway, yaw). Furthermore, the cancellation effect could have an effect on the displacement RAO, as this effect can occur for frequencies higher than the natural frequency. The wave length in shallow water decreases with respect to the deep water waves. The distance between the columns of the floater remains constant, so long waves in deep water with a certain frequency become shorter in shallow water. If these wave lengths are in the same order of magnitude as the floater, cancellation effects could occur. This effect can be seen by the reduced roll and pitch motion for the shallow water case between 0.5 and 1 rad/s. It can be seen in Figure 4.9 that for the same frequencies, the wave excitation force reduces.

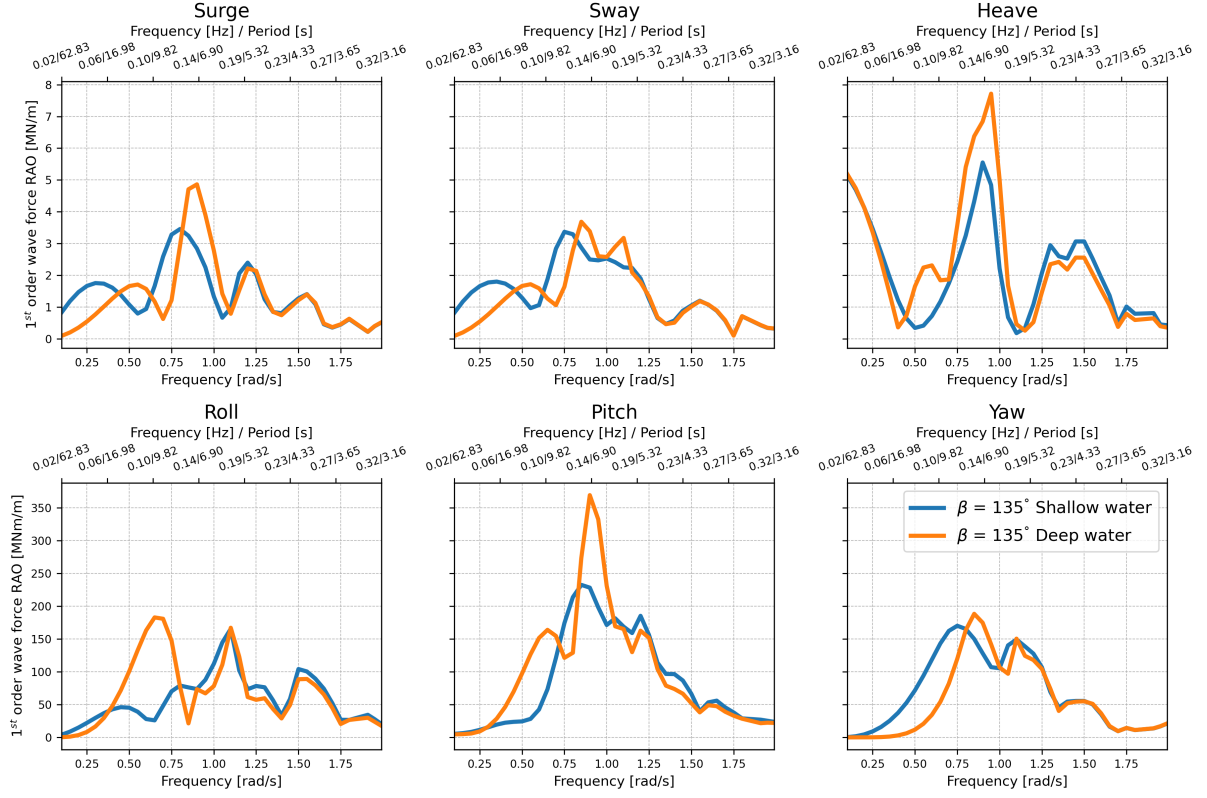


Figure 4.9: First order wave force RAOs in six DOFs for deep and shallow water.

4.2.3. Heave Plate Viscous Damping

Hydrodynamic damping is expected to have a significant influence on the dynamic behaviour of the floater and therefore it is considered in more detail. Initially, only wave radiation damping is evaluated by WAMIT. This is an underestimation of the damping since it does not consider viscous damping. This underestimation results in an overestimation of the floater motions, which is not representative of the floater motions in practice. To account for viscous damping, an extra damping term should be added to the wave radiation damping in the equation of motion. This correction is based on available literature that considers the hydrodynamic properties of a single column with a heave plate, as discussed in section 2.2.2. These experiments are conducted for heave plates without considering a quayside, hence the total damping for the Tri-Floater in shallow water is also determined without a quayside.

The following procedure is applied:

1. An oscillation amplitude of the columns and heave plates A_{osc} is initialised.
2. The KC number is calculated with equation 2.11 for the three corner columns and the centre column.
3. B'_{33} is obtained from studies that performed experiments on oscillating heave plates.
4. At the natural frequency, B_{33} is calculated for all the individual columns with equation 2.13. The total damping of the Tri-Floater is thereafter calculated as $B_{33}^{tot} = 3 \cdot B_{33}^{col} + B_{33}^{cen}$.
5. The damping is added to the hydrodynamic frequency domain model. Since the potential damping B_{33}^{pot} is already included in the model, the total damping excluding the potential damping is added as follows:

$$B_{33} = B_{33}^{tot} - B_{33}^{pot} \quad (4.6)$$

6. With the corrected damping, a new heave motion RAO is calculated and compared with the previous RAO. From this new RAO follows a new oscillation amplitude for the specified wave amplitude: $A_{osc} = \zeta_a \cdot RAO$. The procedure, from step 2 onwards, is repeated until the heave RAO at the natural frequency has converged.

Throughout the iterative process outlined above, the damping varies with the oscillation amplitude, represented by the KC number. As the oscillation amplitude grows, so does the damping, resulting in a damped oscillation. Consequently, this decrease in damping leads to an increase in the oscillation. This recurring pattern continues until an equilibrium is reached between damping and oscillation amplitude. The oscillation amplitude of the floater, and consequently the viscous damping produced by the heave plates, depends on the wave amplitude. Therefore, the iterative procedure was applied to three different wave amplitudes: $\zeta_a = 0.5, 1.0, 1.5$ m.

Non-dimensional Damping Coefficient

In step 3, B'_{33} is obtained by interpolating over the results from the conducted experiments (section 2.2.2), which are presented in appendix C. This interpolation is done for the KC number, oscillation frequency and heave plate submergence. Zhang et al. (2023) conducted experiments that have been executed for a maximum thickness to plate diameter ratio of $1/13 \approx 0.08$. This is larger than the thickness ratios of the Tri-Floater's heave plates, $2.5/28 \approx 0.09$ and $2.5/18 \approx 0.14$ respectively. The results show that for low KC numbers and relatively large thickness ratios, the sensitivity of non-dimensional damping is low. Therefore, it is assumed that the largest experimental thickness ratio can be used for determining the Tri-Floater's damping.

Since the Tri-Floater's heave plates are close to the free surface, this effect should be included in the damping as well. Experiments that are performed by Wadhwa and K. P. Thiagarajan (2009) have been used to include this shallow draft effect in the Tri-Floater's non-dimensional damping. The increase in damping due to this shallow draft effect is included by interpolating the experimental results. The interpolation over all the experimental results is performed for every iteration to obtain the converged linearized damping.

With the obtained non-dimensional damping at every iteration, the motion RAO is calculated, as described in the section 4.2.1. Figure 4.10 shows these motion RAOs for each iteration until it has converged to the final RAO. This Figure gives the iterations for a wave amplitude of $\zeta_a = 0.5$ m. Similar figures can be produced for the other wave amplitudes.

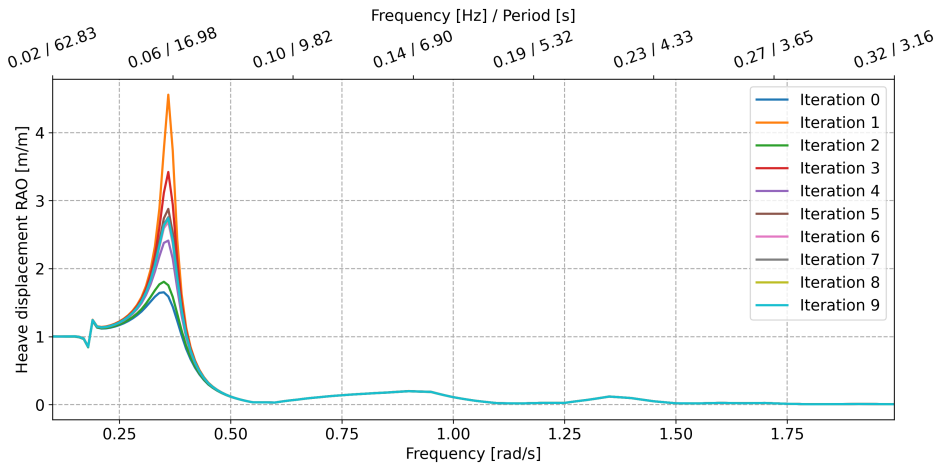


Figure 4.10: Heave motion RAOs at each iteration of the damping for $\zeta_a = 0.5$ m.

The drag coefficients C_D for individual columns and heave plates are determined during the iterations, as in equation 2.9. These values are used in pyCalmot to calculate the drag for all the DOFs. It utilises the damping linearisation procedure recommended by ITTC (ITTC - Recommended Procedures and Guidelines 2011). A comparison is made between the added damping from the iterative procedure, and pyCalmot that uses the drag coefficient, to evaluate how they compare. The experiments in the used literature determine the damping in heave, so the comparison is made for this DOF. This comparison can be seen in Figure 4.11.

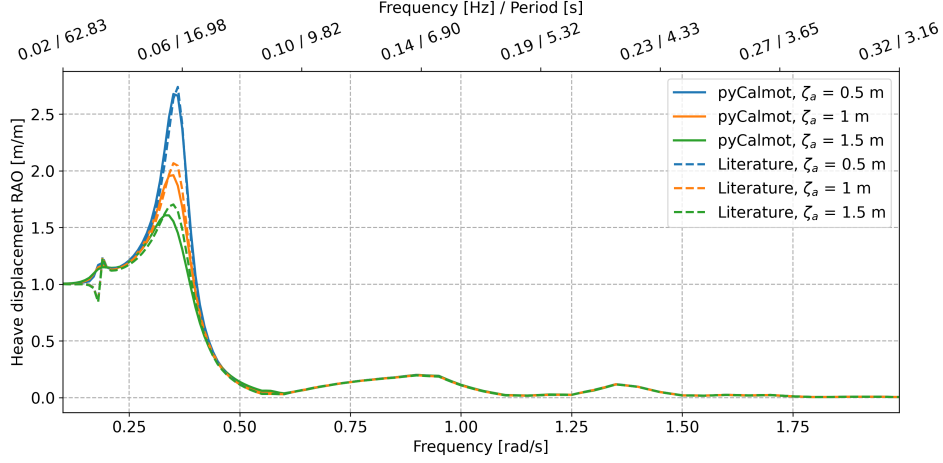


Figure 4.11: Comparison of heave motion RAO from literature procedure and pyCalmot for three wave amplitudes.

pyCalmot shows good accordance with the damping obtained from the literature. Close to the natural frequency, where damping matters the most, there is a small deviation, while for higher frequencies the results are almost exactly the same. Based on this comparison, it is assumed that pyCalmot is sufficiently accurate to be used for this study.

4.2.4. Braces Viscous Damping

So far, only the viscous damping of the heave plates has been considered. To account for the viscous damping that arises from the braces, they are modelled as Morison elements with a drag coefficient $C_{D,brace}$. This coefficient for a circular cylinder depends on the KC number, Reynolds number Re , and roughness Δ (DNV-RP-C205). For oscillatory fluid flow, Re is calculated as the product of the KC number (equation 2.11) and frequency parameter β (equation 2.10):

$$Re = \beta \cdot KC = \frac{\omega A_{osc} D_{brace}}{\nu} \quad (4.7)$$

$$\Delta = \frac{k}{D_{brace}} \quad (4.8)$$

Where k is the roughness height and D_{brace} is the brace diameter. For painted steel, without marine growth or corrosion, this is $5 \cdot 10^{-6}$ m. Hence, the Tri-Floater's braces have a roughness of $\Delta = 2.5 \cdot 10^{-6}$, which is a smooth surface according to DNV-RP-C205 (2021). For the three considered wave amplitudes in the previous section, the Reynolds numbers are in the range of $9.2 \cdot 10^5$ to $1.7 \cdot 10^6$. The DNV standard states that for a high Reynolds number ($Re > 10^6$) and a smooth surface, the drag coefficient can be taken as $C_D = 0.65$. It is assumed that the Reynolds number $Re = 9.2 \cdot 10^5$ is high enough to use this drag coefficient. With these values, the damping generated by the braces is linearised by pyCalmot and added to obtain the damping of the entire floater. The results of the added brace damping can be seen in Figure 4.12. Only the part of the RAO where there is a difference noticeable is plotted in the figure. It can be seen that the peak of the heave RAO is slightly lower, because of the extra damping. This small decrease in heave response is expected because the braces are small compared to the heave plates and columns. So their capability of generating damping is also relatively small.

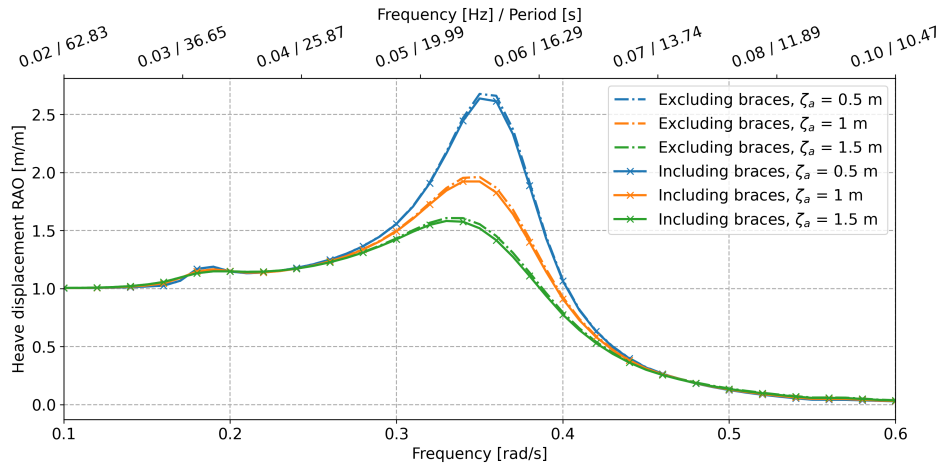


Figure 4.12: Comparison of heave motion RAO excluding and including Tri-Floater braces.

4.2.5. Added Mass Effect

Special attention should be paid to the added mass in very shallow water (DNV-RP-C205). WAMIT takes the shallow water into consideration but is not able to capture non-linear effects due to interaction with the seabed. Experiments are necessary to make a better estimate of the total added mass. The procedure for calculating the added mass based on literature is similar to that of the damping. At the calculated KC numbers, natural frequency, and submergence is the experimental added mass determined, based on the previously mentioned experiments.

As discussed in section 2.2.2, the added mass is unclear for a shallow submergence above a certain critical KC number (Wadhwa and K. P. Thiagarajan 2009). For the Tri-Floater, the KC number does not exceed this critical limit for small wave amplitudes ζ_a . After the interpolations, similar to that of the damping, the total added mass in heave at the natural frequency is obtained from experiments as $3.56 \cdot 10^4$ tonne. Compared to the added mass calculated from the 3D diffraction-radiation model, the result from the literature is approximately 4.8% higher. This will decrease the natural frequency by about 2.3%. It is assumed that the added mass obtained from WAMIT is sufficiently accurate for this research. Hence, no correction for the added mass is applied.

4.3. Characteristic Hub Motions

This modelling step is aimed at obtaining the characteristic hub motions, representing how the hub behaves under a specific sea state. The characteristic displacement and characteristic velocity are of interest for the alignment and mating phase, respectively. The operational limits for these phases are defined differently, hence the approach for calculating the characteristic motions is slightly different. An overview of this modelling step can be seen in Figure 4.13.

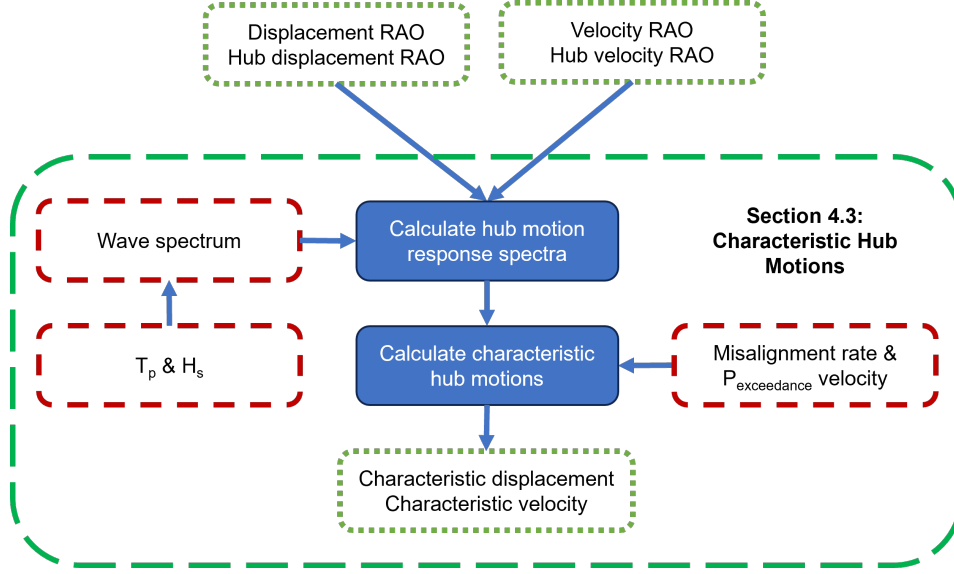


Figure 4.13: Modelling strategy characteristic hub motions.

4.3.1. Hub Motion Response Spectra

For both installation phases, a multitude of sea states are used as input, from which multiple wave spectra ($S_{\zeta\zeta}(\omega, \beta)$) follow. These wave spectra are TMA spectra, as described in section 2.1.1. The displacement and velocity RAOs of the hub are combined with the TMA spectra to arrive at the hub motion response spectra, as given in equation 4.9.

$$S_{\eta\eta}(\omega, \beta) = |RAO(\omega, \beta)|^2 S_{\zeta\zeta}(\omega, \beta) \quad (4.9)$$

So, for every combination of T_p and H_s , response spectra are generated for both axial and radial displacement, as well as for axial and radial velocity. It is assumed that these displacement and velocity responses are Rayleigh distributed, which follows from the same distribution of wave heights in a random sea state. A spectral analysis is performed for the calculated response spectra to obtain the zeroth-order moment (m_0) and zero-crossing period (T_0), by using the following equations:

$$m_i = \int_0^\infty \omega^i S(\omega) d\omega \quad (4.10) \quad T_0 = \sqrt{\frac{m_0}{m_2}} \quad (4.11)$$

4.3.2. Characteristic Hub Motions Calculation

The limits for the alignment phase are expressed in terms of relative displacement and misalignment rate. These two factors are related through the following equation, which is based on the Rayleigh distribution (Journée and Massie 2001):

$$\nu^+ = \frac{T_0}{\exp\left(-\frac{R^2}{2m_0}\right)} \quad (4.12)$$

Where R is the characteristic displacement, T_0 is the zero-crossing period, and m_0 is the zeroth spectral moment or variance of the response spectrum. Rewriting this gives the characteristic displacement as a function of the spectral parameters and desired misalignment rate:

$$R = \sqrt{-2m_0 \ln(T_0 \cdot \nu^+)} \quad (4.13)$$

The limits for the mating phase are expressed in terms of relative velocity and probability of exceedance. The cumulative probability of exceeding a threshold value V_a for a Rayleigh-distributed response is

given by equation 4.14 (Holthuijsen 2007). This threshold value corresponds to the characteristic velocity when p equals the probability of exceedance limit.

$$\Pr\{V_a > V\} = p = 1 - \left(1 - \exp\left(-\frac{V^2}{2m_0}\right)\right)^{\Delta t/T_0} \quad (4.14)$$

Where V and Δt are the characteristic velocity and time interval in seconds, respectively. This equation could be used to find the characteristic velocity for the given probability of exceedance. However, for large duration Δt , or small probability, the extreme value distribution approaches the Gumbel distribution as in equation 4.15 (DNVGL-OTG-13 (2019)).

$$\Pr\{V_a > V\} = p = 1 - \exp(-\exp(-(V - \mu_{gumbel})/\beta_{gumbel})) \quad (4.15)$$

Where μ_{gumbel} and β_{gumbel} are the location and scale parameters of the distribution, respectively. They are dependent on the duration and the spectral parameters m_0 and T_0 as follows:

$$\mu_{gumbel} = \sqrt{2m_0 \ln(\Delta t/T_0)} \quad (4.16) \quad \beta_{gumbel} = \sqrt{\frac{m_0}{2 \ln(\Delta t/T_0)}} \quad (4.17)$$

The limiting probability of exceedance is very low for the mating phase ($p = 1 \cdot 10^{-4}$), hence the Gumbel distribution is better suited for this research. Rewriting this distribution gives an expression for the characteristic velocity based on a given probability of exceedance p , duration Δt , and the spectral parameters:

$$V = \mu_{gumbel} - \beta_{gumbel} \cdot \ln(-\ln(1 - p)) \quad (4.18)$$

The result of this modelling step is the characteristic displacement and characteristic velocity of the hub in the radial and axial direction, for a large range of T_p and H_s combinations.

4.4. Characteristic Blade Motions

In this modelling step, the characteristic blade displacement and velocity are determined in axial and radial directions. These characteristic motions correspond to a specific mean wind speed and direction. First, the blade's EOM are derived and solved with the tagline and blade properties, to obtain the RAOs in two DOFs. These RAOs are combined with wind spectra to arrive at motion response spectra. From these spectra can the characteristic motions be obtained. An overview of this modelling step can be seen in Figure 4.14.

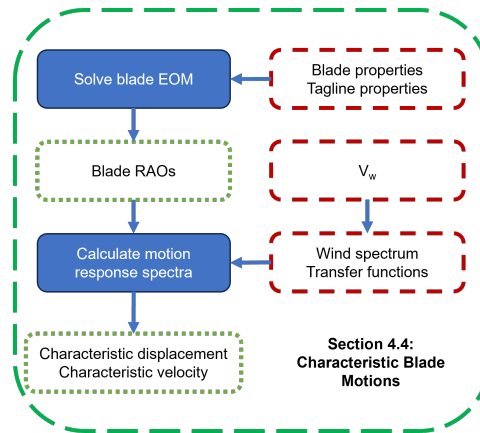


Figure 4.14: Modelling strategy characteristic blade motions.

4.4.1. Solve Blade EOM

To get an estimation of the blade motions, the blade and yoke are simplified to a two DOF pendulum with a point mass that can move in the radial and axial blade direction. The taglines are modelled as spring dampers that provide stiffness and damping in both tension and compression, as explained in section 3.4.4. Furthermore, the drag force, gravity and tagline force are simplified to a point load at the COG of the blade and yoke. This gives the following EOM, which is derived in appendix E, in frequency domain for the blade:

$$-m_b L_{\text{susp}} \omega^2 X_b(i\omega) + i\omega X_b(\omega) L_{\text{susp}} (\rho_{\text{air}} C_d A \overline{V_w} + C_t) + X_b(i\omega) (m_b g + K_t L_{\text{susp}}) = \rho_{\text{air}} C_d A \overline{V_w} V_w = F_w \quad (4.19)$$

Where the other variables:

- X_b : blade motions in radial direction
- m_b : blade and yoke combined mass
- L_{susp} : blade suspension length
- C_t : tagline damping coefficient
- K_t : tagline spring stiffness
- i : imaginary unit

The EOM for the blade motion in the axial direction is the same as for the radial direction. The current modelling step is described based on radial motions for clarity. However, the same approach applies to the axial motions.

The equation can be rearranged to obtain an expression for the blade motions in the radial direction, as in equation 4.20.

$$X_b(i\omega) = \frac{\rho_{\text{air}} C_d A \overline{V_w} V_w}{-m_b L_{\text{susp}} \omega^2 + i\omega L_{\text{susp}} (\rho_{\text{air}} C_d A \overline{V_w} + C_t) + (m_b g + K_t L_{\text{susp}})} \quad (4.20)$$

A displacement RAO that relates blade motions to the external fluctuating wind force is obtained as follows:

$$H_{x_b F_w} = \frac{X_b(i\omega)}{F_w} = \frac{1}{-m_b L_{\text{susp}} \omega^2 + i\omega L_{\text{susp}} (\rho_{\text{air}} C_d A \overline{V_w} + C_t) + (m_b g + K_t L_{\text{susp}})} \quad (4.21)$$

The blade velocity is also of interest because it contributes to the relative velocity between the hub and the blade root. The velocity RAO is the time derivative of the displacement RAO. In the frequency domain, this is calculated as presented in equation 4.22.

$$H_{v_b F_w} = i\omega H_{x_b F_w} = \frac{i\omega}{-m_b L_{\text{susp}} \omega^2 + i\omega L_{\text{susp}} (\rho_{\text{air}} C_d A \overline{V_w} + C_t) + (m_b g + K_t L_{\text{susp}})} \quad (4.22)$$

The pendulum's undamped natural frequency can be obtained from the EOM, as performed in appendix E:

$$\omega_n = \sqrt{\frac{m_b g + K_t L_{\text{susp}}}{m_b L_{\text{susp}}}} \quad (4.23)$$

4.4.2. Calculate Motion Response Spectra

Similar to the floater motions, the aim is to obtain a motion response spectrum from which the characteristic blade motions can be obtained. First, the derivation is shown to relate the wind speed to this response spectrum.

The wind loads on an object are not constant but vary with time, because the wind speed ($V_w(t)$) is a random process. It consists of a mean (\bar{V}) and fluctuating ($v(t)$) term as can be seen in equation 4.24. Here it is assumed that the wind has a horizontal component only.

$$V_w(t) = \bar{V}_w + v(t) \quad (4.24)$$

The wind force is dependent on the squared wind speed and hence should be linearised for a frequency domain analysis. This can be done, under the assumption that the term $v^2(t)$ is small, as follows:

$$V_w^2(t) = \bar{V}_w^2 + v^2(t) + 2\bar{V}_w v(t) \approx \bar{V}_w^2 + 2\bar{V}_w v(t) \quad (4.25)$$

This result can be used to obtain the linearised wind force as in equation 4.26:

$$F_w = \frac{1}{2} \rho_{\text{air}} C_d A V_w^2(t) \approx \frac{1}{2} \rho_{\text{air}} C_d A \bar{V}_w^2 + \rho_{\text{air}} C_d A \bar{V}_w v(t) \quad (4.26)$$

where, ρ_{air} is the air density in kg/m^3 , A the projected area in m^2 perpendicular to the wind. Based on this equation, a transfer function can be obtained that relates the wind force to the fluctuating wind speed:

$$H_{F_w V_w} = \frac{F_w}{V_w} = \rho_{\text{air}} C_d A \bar{V}_w \cos(\beta_{\text{relative}}) \quad (4.27)$$

The effect of the wind's relative direction with respect to the blade is considered by including a cosine term. The definition of this relative wind direction is presented in section 3.3.1. The transfer function for the loads in the axial direction is similar, but it has a sine term to account for the relative wind direction. With this transfer function as a result, the wind-induced force spectrum can be obtained by combining the transfer function, that relates the load to fluctuating wind speed, and a Kaimal wind spectrum. This spectrum is discussed in section 2.3.1.

$$S_{F_w F_w} = |H_{F_w V_w}|^2 S_{\text{kaimal}} \quad (4.28)$$

Similar to the approach for the hub motions, the displacement and velocity RAOs (section 4.4.1) are combined with the wind-induced force spectrum to arrive at the blade motion response spectra. These motion response spectra show the blade's response to various wind frequencies. The displacement and velocity response spectra are given in equations 4.29 and 4.30, respectively.

$$S_{x_b x_b} = |H_{x_b F_w}|^2 S_{F_w F_w} \quad (4.29)$$

$$S_{v_b v_b} = |H_{v_b F_w}|^2 S_{F_w F_w} \quad (4.30)$$

These response spectra are visualised in Figures 4.15a and 4.15b below for mean wind speeds between 2 and 14 m/s, together with the natural frequency. The Kaimal spectrum is used as defined in section 2.3.1.

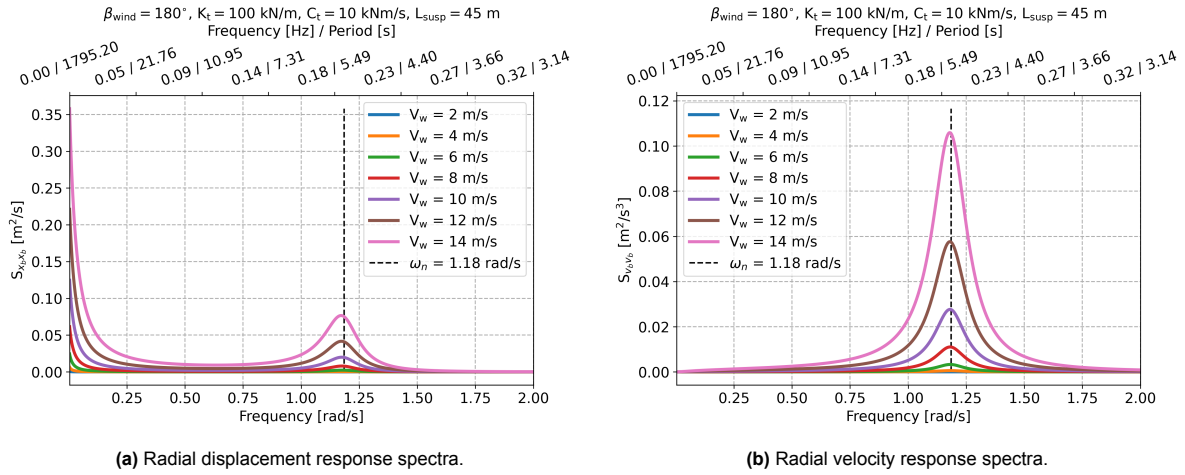


Figure 4.15: Blade radial displacement and velocity response spectra for different wind speeds.

The characteristic blade motions are derived from the motion response spectra. Given that the wind speed follows a Gaussian distribution, it is assumed that the blade motion response also follows a Gaussian distribution with a zero mean. The allowable probability of exceedance for the relative velocity between the blade and hub is small, meaning that the characteristic velocity should correspond to a low probability of exceedance. For a Gaussian-distributed random variable, the probability of exceedance depends on the standard deviation. The characteristic velocity is defined as four times the standard deviation, $V_{blade} = 4\sqrt{m_0}$, where m_0 represents the variance of the velocity response spectrum. This results in a probability of exceedance of $p = 6 \cdot 10^{-5}$, which is slightly more conservative than the probability suggested by DNV.

The probability of exceedance of the relative displacement is not as low as for the velocity. Therefore, the characteristic displacement is taken as two times the standard deviation, $R_{blade} = 2\sqrt{m_0}$. This corresponds to a probability of exceedance of $p = 0.046$.

The result of this modelling step is the characteristic displacement and characteristic velocity of the blade in the radial and axial direction, for all combinations of V_w and β_{wind} .

4.5. Allowable Environmental Conditions

The allowable environmental conditions, under which the blade can be installed, can be obtained with the characteristic hub and blade motions as input for this modelling step. First, the hub motion limits are determined, which are based on the characteristic blade motions and the operational limits. Thereafter, the allowable environmental conditions for the alignment and mating phase are calculated. This modelling step is summarised in Figure 4.16.

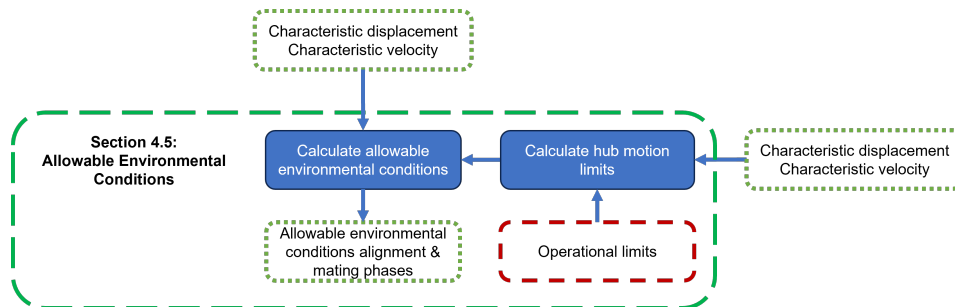


Figure 4.16: Modelling strategy allowable environmental conditions

4.5.1. Hub Motion Limits

The relative motions between the turbine hub and blade must remain within the operational limits, as defined in section 2.4. Both hub and blade motions contribute to these relative motions, which means that blade motions reduce the allowable hub motions. To find the environmental conditions under which the installation can be successfully executed, the allowable sea states are determined for a range of wind speeds. For each wind speed, the allowable hub motion must be calculated. For example, if the relative displacement limit is 0.2 m and the blade displacement at a wind speed of 5 m/s is 0.05 m, then the allowable sea states are based on the allowable hub displacement of 0.15 m.

The relative motions of the blade and hub can be in or out of phase, corresponding to minimum and maximum relative motions, respectively. However, since the relative phase between the blade and hub motions is unknown, a conservative assumption is made that they are always out of phase. Therefore, the allowable hub motions (R_{hub} or V_{hub}) are calculated as the difference between the relative motion (R_{lim} or V_{lim}) limits and the characteristic blade motions. This conservative approach results in the following expressions for the allowable hub displacement and velocity:

$$R_{hub} = R_{lim} - R_{blade} \quad (4.31)$$

$$V_{hub} = V_{lim} - V_{blade} \quad (4.32)$$

With this approach, the allowable hub motions can be calculated for a large range of wind speeds and directions. This result is used to determine the allowable sea states for all these wind conditions.

4.5.2. Calculate Allowable Environmental conditions

The inputs for this calculation are the characteristic floater motions for a range of T_p and H_s combinations (section 4.3.2) and the hub motion limits for a range of wind conditions (section 4.5.1). The characteristic hub motions are compared to the allowable hub displacement for each wind condition. If the characteristic hub motion is larger than the allowable hub motion, the significant wave height corresponding to this characteristic motion is too high.

Because the frequency domain model is linear, the significant wave height is directly proportional to the hub motions. This linearity allows for scaling H_s so that the characteristic hub motions are adjusted to match the allowable hub motion. This results in the allowable significant wave height:

$$H_{s,allowable} = \frac{R_{hub}}{R} \cdot H_s \quad (4.33)$$

$$H_{s,allowable} = \frac{V_{hub}}{V} \cdot H_s \quad (4.34)$$

In this modelling step, the allowable wave heights are calculated for a range of wind conditions, wave directions, and peak periods. These calculations consider both axial and radial displacement and velocity, resulting in the allowable environmental conditions for the alignment and mating phases. These results will be used to calculate the operability, as explained in the next section.

4.6. Operability

In this modelling step, the allowable environmental conditions for both installation phases are used as input in combination with site-specific metocean data. This calculation gives the final operability result. The overview of this modelling step is given in Figure 4.17.

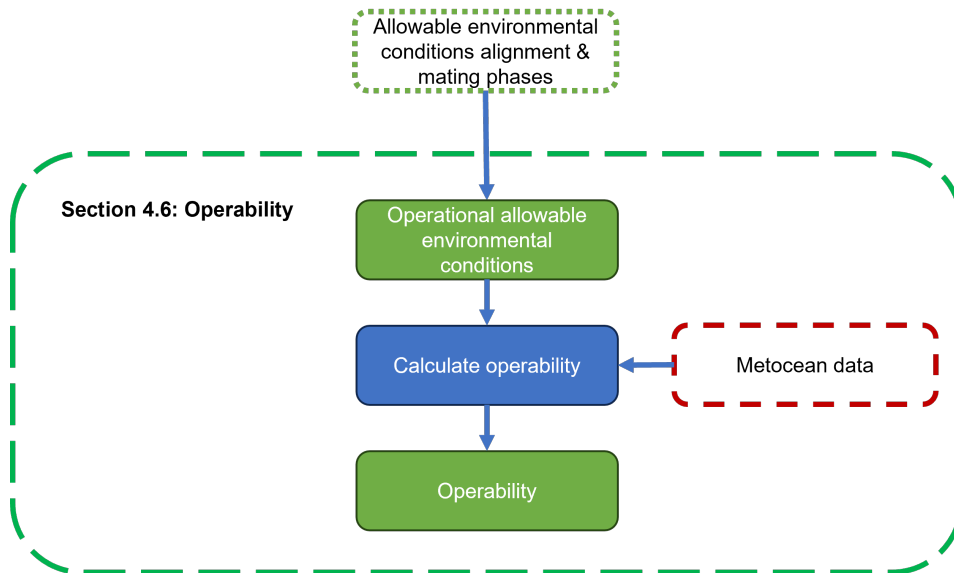


Figure 4.17: Modelling strategy operability.

The results from the previous modelling step provide the allowable environmental conditions for four specific motion components: relative axial displacement, relative radial displacement, relative axial velocity, and relative radial velocity. These results indicate the conditions under which each of these individual motions remains within the operational limits. However, for a successful blade installation, all motion components must simultaneously remain within their limits. Therefore, the overall operational allowable environmental conditions are the lower envelope of these individual conditions.

To ensure successful installation, the operational allowable environmental conditions must be met during the 30-minute installation reference period, T_R . Using historical metocean data, the number of workable weather windows where the environmental conditions are within the allowable environmental conditions can be determined. Thereafter, the operability is calculated as the ratio between these workable weather windows and the maximum possible number of windows within the same period. The result gives the operability of the blade installation.

5

Results

In this chapter are the results of the study presented, where the dynamic model is used with different inputs to analyse the blade installation. Only the mesh convergence study is not repeated, instead, the same mesh size of 1.0 m is used. The blade and floater move independently from each other, and hence they are analysed individually first. Thereafter, the relative motions between the blade and hub are considered and the operability for five different installation strategies is determined. Finally, the importance of wind and waves on the operability is studied.

5.1. Blade Motions

Under the used modelling assumptions, three parameters can be altered to influence the blade motions: suspension length, tagline capacity, and wind alignment. The sensitivity of these parameters is described below.

5.1.1. Suspension Length Sensitivity

During the blade installation, the blade's motions can be lowered by avoiding excitation at its natural frequency. For a pendulum with springs attached to it, the natural frequency can be influenced by changing the mass, pendulum length and spring stiffness. The most easily controllable parameter during blade installation is the suspension length (L_{susp}) between the crane tip and the yoke. As explained in section 3.4.3, the suspension length varies between 40 and 50 m. The sensitivity of the blade displacement and velocity in the radial direction, for this change in suspension length, can be seen in Figure 5.1. A wind speed up to 10 m/s is used, as this is assumed to be the maximum wind speed for which wind turbine blades can be installed. The stiffness and damping of the taglines are constant and the wind is perpendicular to the blade ($\beta_{wind} = 180^\circ$). Similar figures for the axial motions are presented in Appendix F.1.

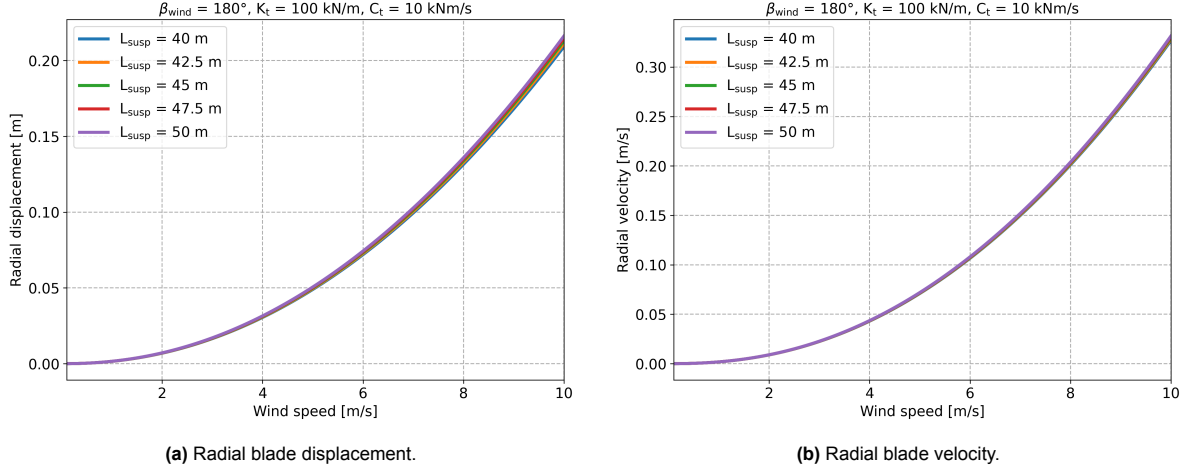


Figure 5.1: Effect of the suspension length on the radial displacement and velocity for different wind speeds.

It can be seen that a shorter pendulum length reduces the blade's motions, which becomes most noticeable at higher wind speeds. The maximum motions, at the highest and lowest suspension lengths, are given in Table 5.1 for a wind speed of 10 m/s. The reduction in pendulum length of 20%, results in a small decrease in the motions which is also given in the table. For the axial motions, the sensitivity is larger compared to the radial motions, but the absolute values are small. Hence, the sensitivity is sufficiently low to ignore the variation in suspension length for the rest of this research. The average length of 45 m will be used.

Table 5.1: Suspension length sensitivity at 10 m/s wind speed.

Motion	$L_{susp} = 50 \text{ m}$	$L_{susp} = 40 \text{ m}$	Motion reduction
Radial displacement	0.22 m	0.21 m	3%
Radial velocity	0.33 m/s	0.33 m/s	1%
Axial displacement	0.02 m	0.01 m	12%
Axial velocity	0.02 m/s	0.02 m/s	5%

5.1.2. Tagline Diameter Sensitivity

The second controllable parameter that influences the blade motions is the capacity of the tagline system to restore and dampen these motions. For this research, Dyneema taglines are considered, which are commonly available in diameters up to 16 mm (Ropes 2024). The influence of different tagline diameters (D_t) on the radial blade motions is presented in Figure 5.2. Increasing the line diameter results in a squared increase in stiffness (K_t) since line stiffness depends on the material, length, and cross-sectional area. For this sensitivity study, the damping ratio (ζ_{damp}) is kept constant with respect to the 16 mm tagline. Therefore, the damping coefficient is calculated as in equation 5.1.

$$C_t = 2\zeta_{damp}m_b\omega_n \quad (5.1)$$

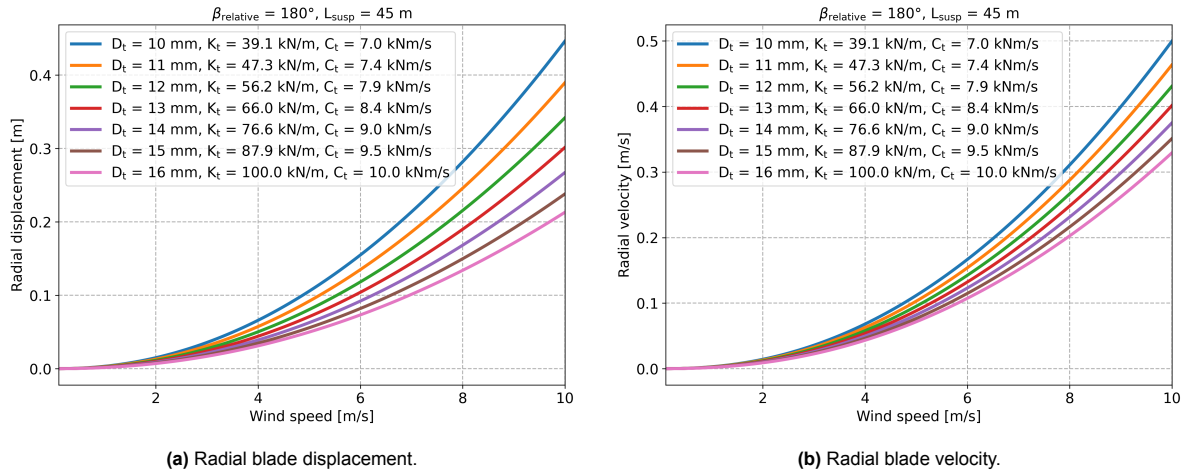


Figure 5.2: Effect of the tagline stiffness on the radial displacement and velocity for different wind speeds.

It can be seen that the tagline diameter significantly influences the blade radial motions, especially the displacement. The maximum motions, for the smallest and largest diameters, are given in Table 5.2 for a wind speed of 10 m/s. The increase in line diameter of 60% results in a large decrease in the motions, which is also given in the table. For the axial motions is the sensitivity lower compared to the radial motions, because the taglines exert a force mainly in the radial direction of the blade. The high diameter sensitively indicated that it is beneficial to use a large diameter tagline that has a high stiffness. Hence, for the rest of this research will the 16 mm tagline be used.

Table 5.2: Tagline stiffness sensitivity at 10 m/s wind speed.

Motion	$D_t = 10\text{mm}$	$D_t = 16\text{mm}$	Motion reduction
Radial displacement	0.45 m	0.21 m	52%
Radial velocity	0.50 m/s	0.33 m/s	34%
Axial displacement	0.02 m	0.01 m	32%
Axial velocity	0.02 m/s	0.02 m/s	24%

5.1.3. Blade Orientation Sensitivity

The third parameter that influences the blade motions is the orientation of the blade with respect to the wind. For example, it can be oriented such that the wind is perpendicular ($\beta_{\text{relative}} = 180^\circ$) or parallel ($\beta_{\text{relative}} = 90^\circ$) to the blade. In Figure 5.3a are the radial and axial displacement shown for different wind speeds and directions with respect to the blade. A more detailed view of these graphs can be seen in Figure 5.3b. Similar figures for the blade velocity are presented in Appendix F.3.

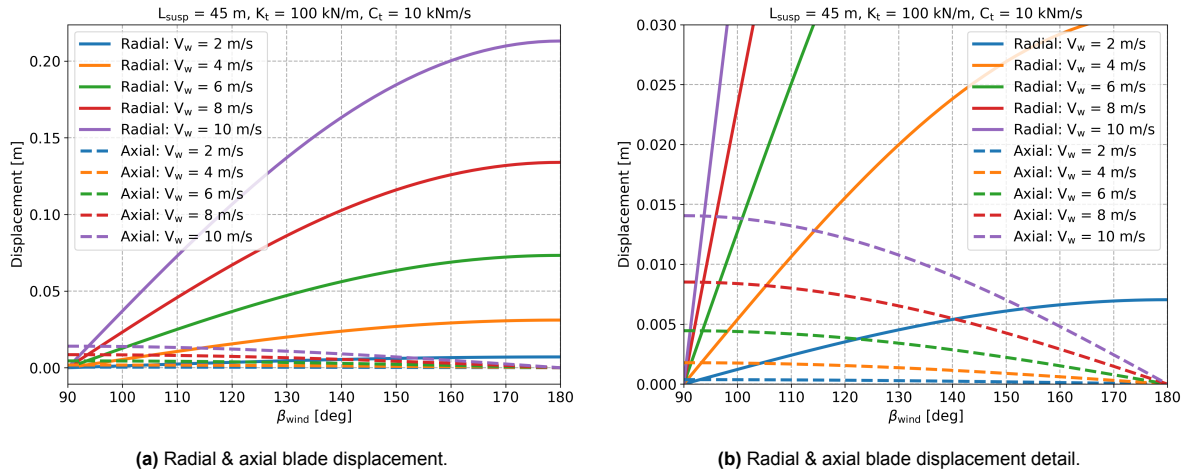


Figure 5.3: Effect of the blade orientation with respect to the wind on the displacement for different wind speeds.

It can be seen that the overall motions are lowest when the wind is parallel to the blade. When the wind inflow is more perpendicular to the blade, the radial displacement and velocity increase more than the axial motions decrease. The blade orientation during the installation will also depend on the hub motions, but based on this sensitivity study, it is likely to be beneficial to orient the blade parallel to the wind.

5.2. Floater Motions

Alongside the blade motions, the floater motions are of relevance for the blade installation. There is one parameter that can be controlled under the assumption that the floater's orientation and draft are constant. In this section, the quayside distance is varied, to study its effect on the floater motions and the allowable sea states. Furthermore, the critical hub motions for this floater location will be identified.

5.2.1. Quayside Distance Sensitivity

To get a better understanding of the effect of quayside distance, the floater's displacement RAOs are analysed in more detail. Figure 5.4 shows the displacement RAOs in surge, sway, and heave, at the COG for five different quayside distances within the feasible distance range for installation. A wave direction of 135° is considered to see a response in all DOFs. A similar figure for the RAO in roll, pitch, and yaw are presented in Appendix F.4.

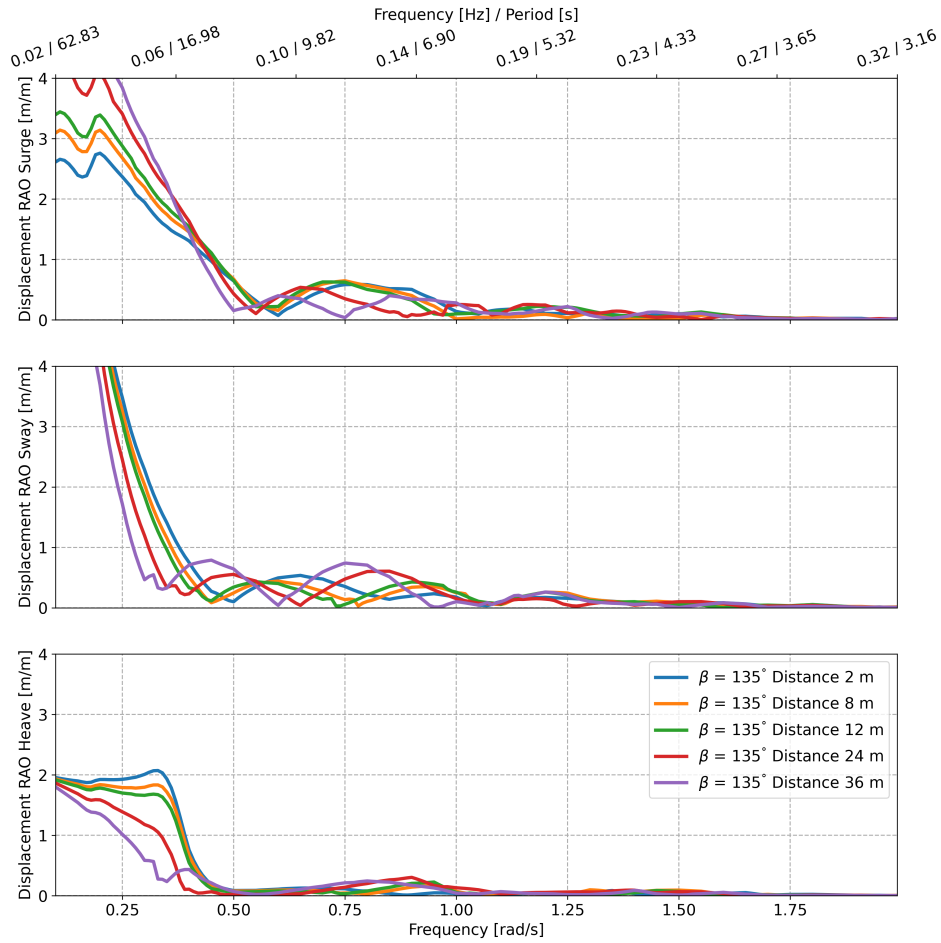


Figure 5.4: Quayside distance dependent displacement RAOs for surge, sway, and heave.

In this figure, it can be observed that there is a large variety in the response for different quayside distances. Particularly in the frequency range of 0.5 to 1 rad/s. At one specific frequency, a particular quayside distance may result in no response, while another distance might produce the largest response, and vice versa. A similar effect is noticeable in the other DOFs, but the difference in roll and pitch is smaller. This effect is likely to be caused by the complex wave field that arises due to the quayside. Furthermore, the response is similar for all the distances at low frequencies. Only the magnitude of the response is considerably different.

The effect of quayside distance on floater motions in different sea states will be analysed. This sensitivity study will be performed based on characteristic hub motions and allowable significant wave heights.

Characteristic hub motions

The characteristic hub displacement and velocity provide insight into the response of the floating structure to different wave conditions. The effect of different quaysides is analysed based on the hub displacement since the results are qualitatively very similar to the hub velocity. The figures for the velocity are presented in Appendix F.4. Figure 5.5 shows the radial characteristic displacement of the hub for different distances to the quayside and wave directions, where a lower displacement is better. The nacelle is not rotated ($\psi_{\text{nacelle}} = 0^\circ$), and the motions are based on a 2 m significant wave height.

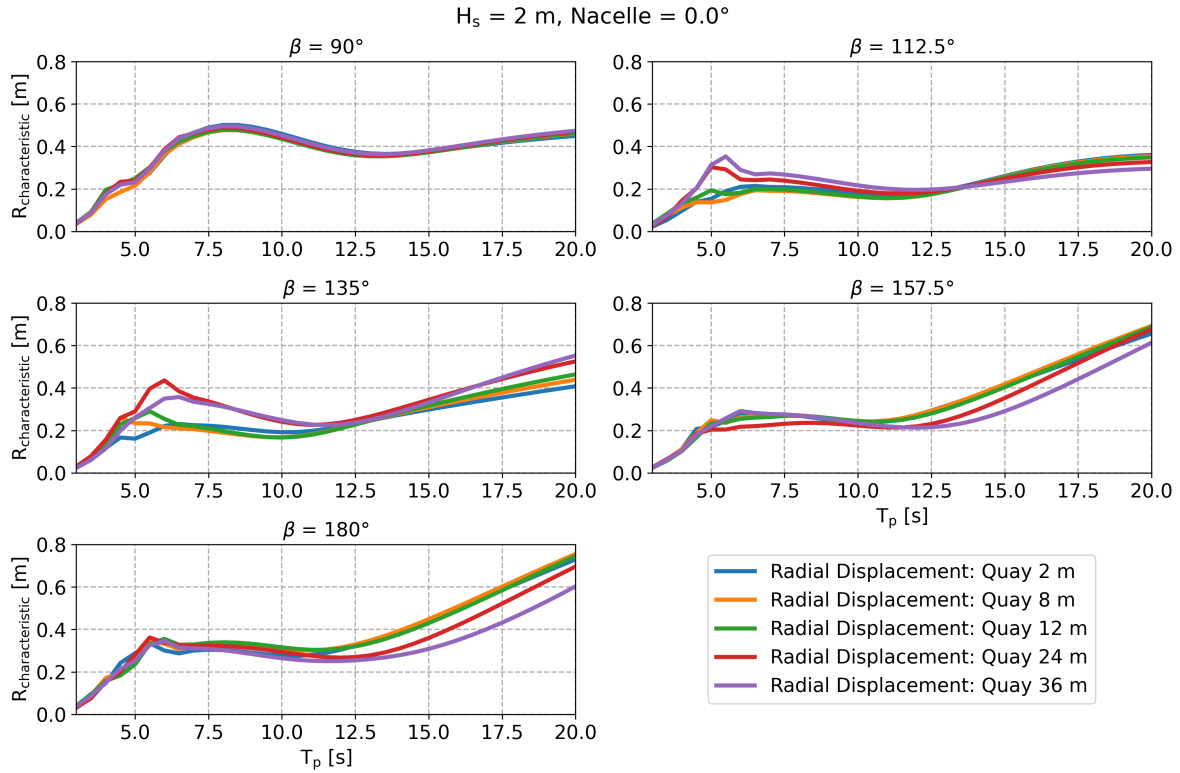


Figure 5.5: Characteristic radial displacement for multiple quayside distances and wave directions.

Firstly, it can be seen that the radial hub motions are significantly dependent on the wave period. For the different wave directions, the trend shows that the displacement increases up to a peak period of approximately 6-7 seconds. For higher periods it remains constant or declines slightly. Thereafter, it increases again for even higher peak periods.

Secondly, the figure shows that the quayside distance has a wave direction dependent influence on the motions. For example, a large quayside distance (24–36 m) leads to increased motions when the wave direction is 135° . However, when the waves are more perpendicular to the quayside, the motions become lower for these larger distances. This is likely caused by the position of the floater with respect to the different reflective waves, as explained in section 2.1.2. When the waves are parallel to the quayside ($\beta = 90^\circ$), there is almost no influence of the quayside distance, because waves are not reflecting from the quayside.

The axial motions show a similar trend compared to the radial motions, as can be seen in Figure 5.6. However, the axial component is larger than the radial motion for most wave directions. It is remarkable that there is a large variation between the quayside distances for a wave direction of 112.5° , whereas there is almost no difference when the wave direction is 157.5° . Lastly, there is almost no axial motion for waves perpendicular to the quayside, which can be explained by the fact that there are almost no sway, roll, and yaw motions of the floater for this wave direction.

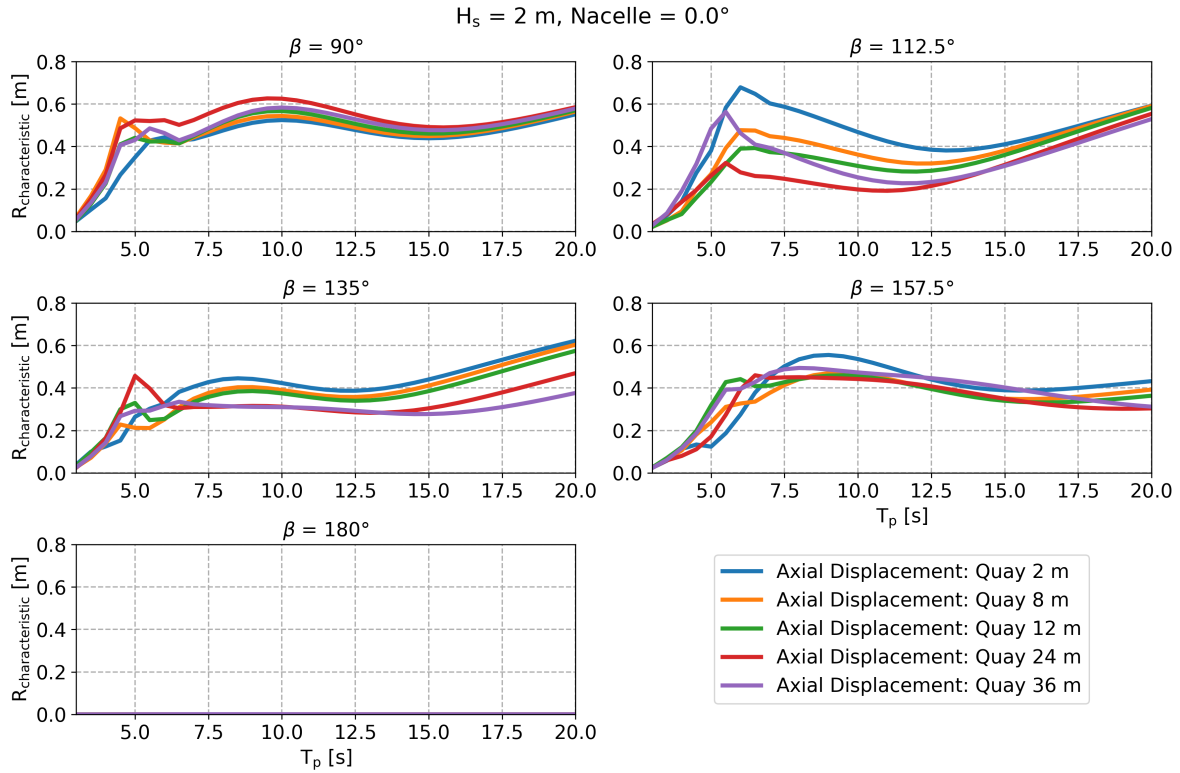


Figure 5.6: Characteristic axial displacement for multiple quayside distances and wave directions.

Allowable significant wave height

The previous figures demonstrate that the motions for different quayside distances are strongly influenced by the peak period and wave direction. To gain better insight into how these environmental conditions affect the workable conditions for various quayside distances, the allowable significant wave heights are studied.

The allowable limits for each motion are obtained for the situation where there are no blade motions ($V_w = 0 \text{ m/s}$) and the nacelle is not rotated. To obtain the overall allowable wave height for all the installation phases, the lower limit of the radial and axial displacement and velocity is used. Figure 5.7 shows the allowable H_s against the peak period for different wave directions and quayside distances, where a higher allowable wave height is better.

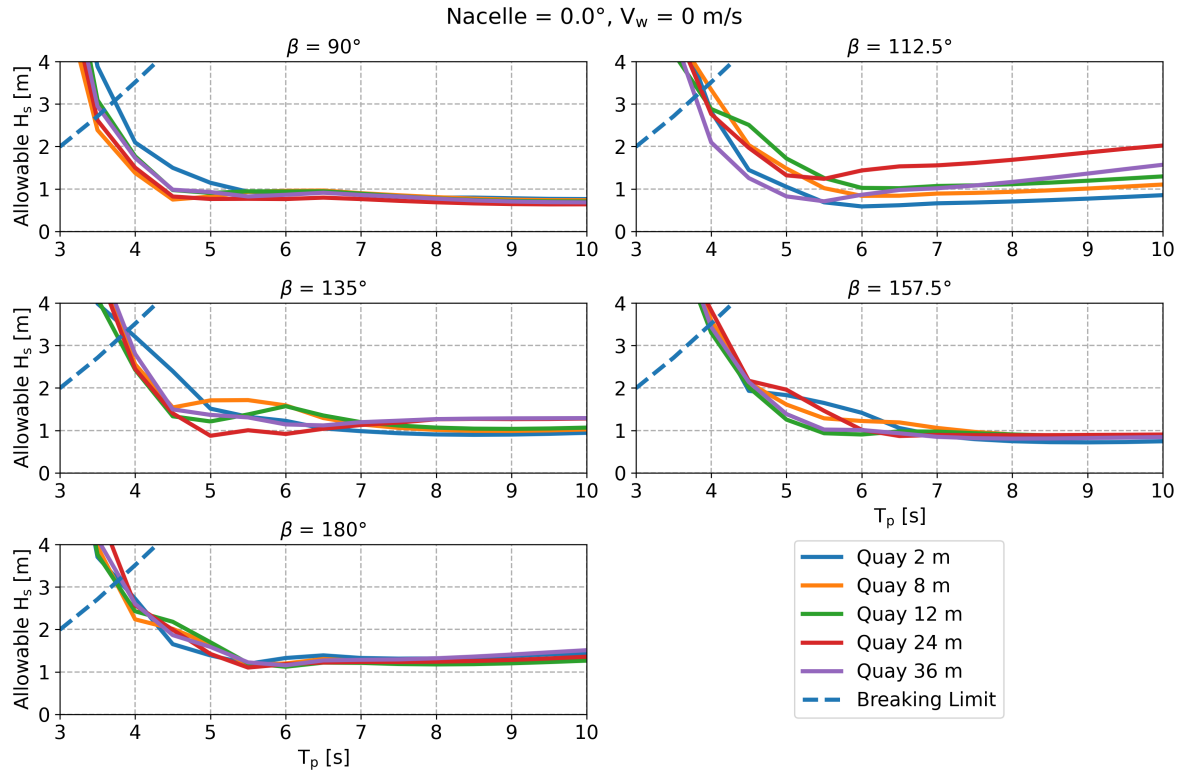


Figure 5.7: Allowable H_s vs. peak period for multiple quayside distances and wave directions.

It can be seen that, similar to the individual motion components, the overall allowable wave height is significantly influenced by the quay distance for certain combinations of wave direction and peak period. Especially for $\beta = 112.5^\circ$, where the allowable wave height can be twice as high for a different quay distance. In Appendix F.4, similar plots for more wave directions are given.

To gain more insight into the effect of wave direction on the allowable wave height, Figure 5.8 shows the allowable wave height against the wave direction for different quayside distances and peak periods.

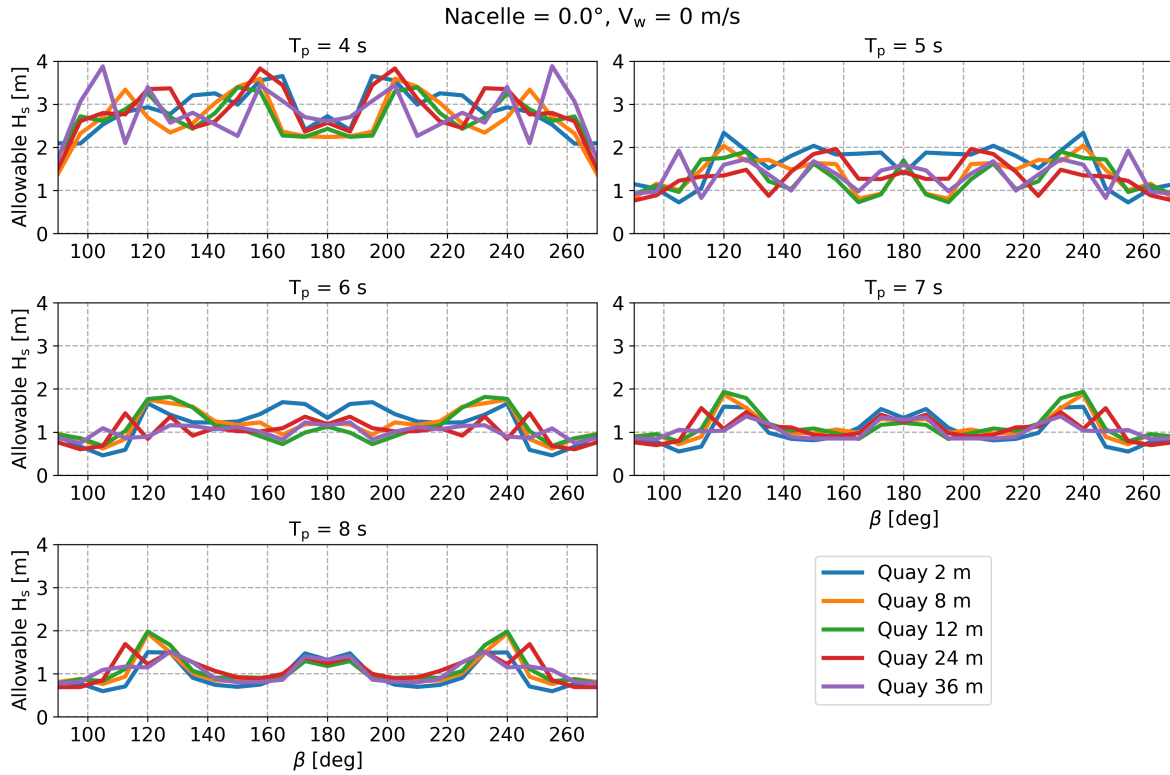


Figure 5.8: Allowable H_s vs. wave direction for different peak periods and quayside distances.

The figure confirms that the allowable wave height considerably depends on the combination of wave length and direction. Moreover, there are not many wide ranges of wave directions where one quayside distance is more suited than others. This can for example be seen in the plot for $T_p = 4$ s, where a quay distance of 36 m has a significantly higher limit for a 105° wave direction. A small change in direction to 112.5° results in the lowest performance. Only the 2 m distance excels for 160° - 200° waves with a peak period between 5 and 7 seconds. Other than that, the optimal distance fluctuates considerably. On the contrary to this fluctuating behaviour, there are no exceptional combinations of environmental conditions for which the allowable wave height is extremely low. Hence, there are no distances that should definitely be avoided.

Theoretically, it would be best to change the floater's location to the optimum location based on the conditions at the moment of installation. However, in practice, it is not convenient to relocate the floater when the environmental conditions change. Therefore, a suited quayside distance should be found to install the blade under a variety of wave conditions. Figure 5.9 shows the minimum allowable significant wave height for every wave period. In other words, it gives the allowable wave height for each quayside distance for its most critical wave direction.

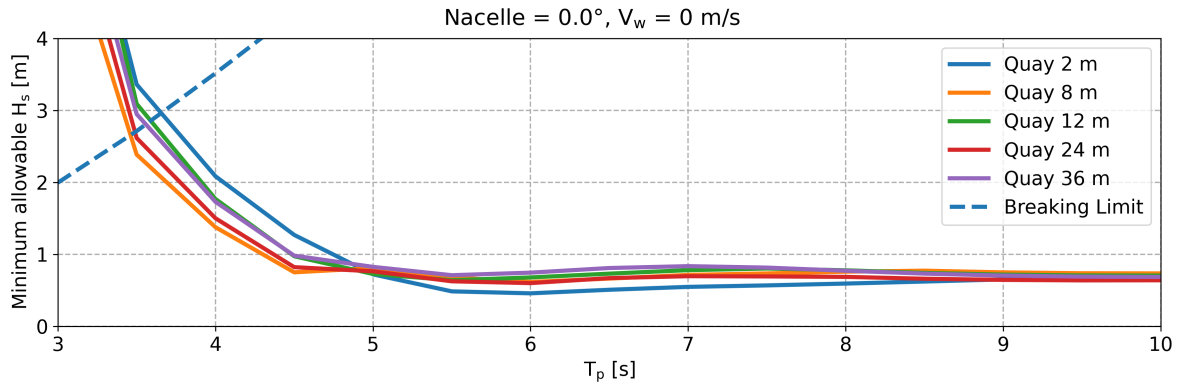


Figure 5.9: Minimum allowable H_s vs. peak period for multiple quayside distances.

It can be observed that for low peak periods, the 2 m distance is the optimal value. However, when the period is higher than 5 s, this is the worst performing distance. The 8 and 24 m locations are not the optimal choices, since for shorter waves they are significantly worse than the other options. The 12 and 36 m distances have the best performance on average over the entire T_p range. It is more practical to have the floater closer to the quayside, so a 12 m distance is most suited for the Tri-Floater. This distance will be used for further analysis in this thesis.

5.2.2. Critical Hub Motions

It is relevant to identify the most critical motions during the operation. Based on these motions, potential improvements can be explored. Figure 5.10 shows the allowable H_s for each motion during the alignment and mating phases. Moreover, the lower limit of these motions, which also has been used in the previous sensitivity study, can be seen in the plots. Here, only the hub motions are considered for a quayside distance of 12 m. Five different wave directions are considered. In Appendix F.5 more wave directions are considered, where similar behaviour can be observed.

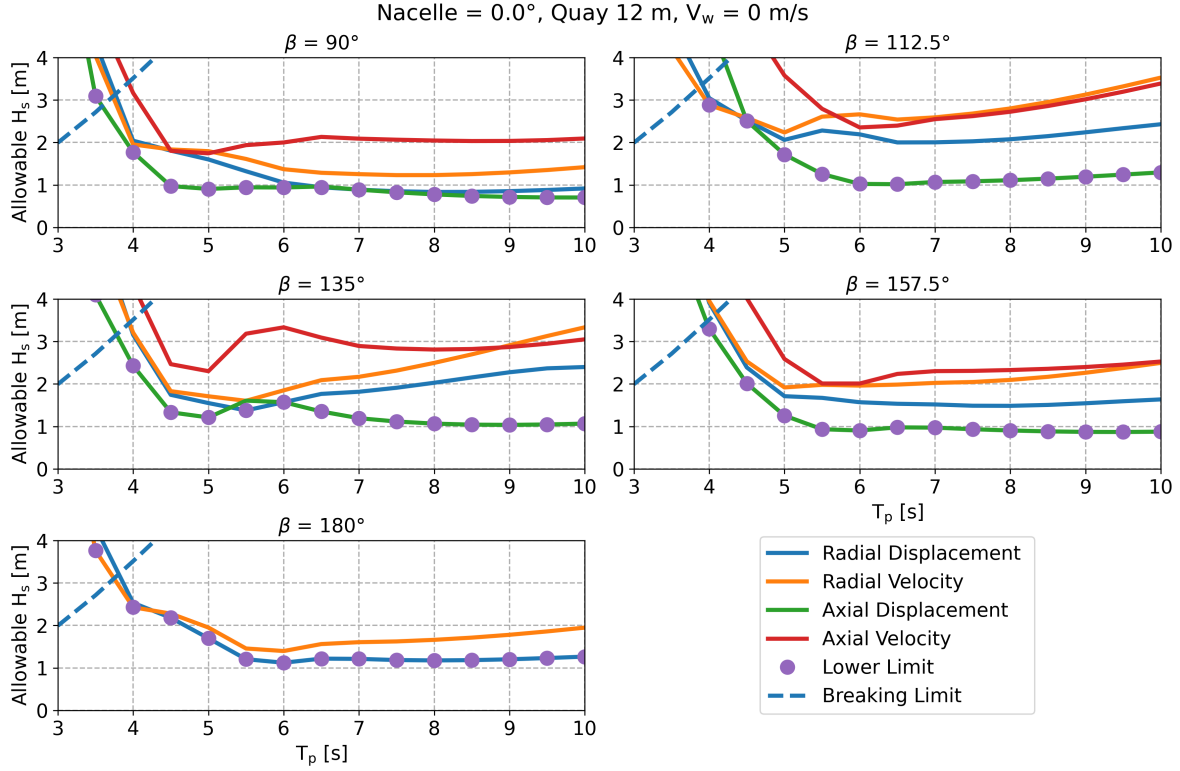


Figure 5.10: Limiting floater motions for different wave directions and peak periods.

In this figure, it can be seen that the axial displacement for most wave conditions is the limiting motion. There are a few exceptions where the radial velocity and radial displacement are more limiting. The axial velocity is under almost all conditions the least critical motion. Based on this result, it becomes clear that the blade displacement in axial direction should be minimised, while the other motion components could be slightly higher. This will give the highest chance of a successful installation.

5.3. Relative Motions

With the individual motions of the blade and hub analysed, now the relative motions will be considered. First, the sensitivity of the fourth controllable parameter, nacelle rotation, is studied. After that, the optimal nacelle heading is studied.

For easier comparison between different nacelle and blade rotations, these rotations are expressed in terms of relative nacelle and blade heading with respect to the aligned wind and wave directions. Since the nacelle and blade maintain the same orientation relative to each other during the installation, they are conveniently referred to as ‘relative blade heading’ or ‘relative nacelle heading’.

5.3.1. Nacelle Heading Sensitivity

As explained in section 3.3, the nacelle heading can be altered, which makes it possible to reduce the critical motions of the floater. Furthermore, the orientation can be based on the most favourable blade and hub orientation to minimise these critical motions. Figure 5.11 shows how rotating the nacelle can alter the allowable H_s , caused by a change in critical motion. In this figure, the allowable significant wave height for the four limiting motions is shown against the relative heading (β_{relative}) for multiple wind and wave directions (β). It shows that the optimal heading is dependent on this wind/wave direction. For example, if the waves and wind are incoming at $\beta = 157.5^\circ$, the allowable H_s can be increased by rotating the nacelle and blade to achieve a relative nacelle heading of approximately $\beta_{\text{relative}} = 265^\circ$. For this relative direction, both the axial and radial displacement are limiting. This heading is not performing well for $\beta = 90^\circ$. For this wind and wave direction is $\beta_{\text{relative}} = 230^\circ$ more suited.

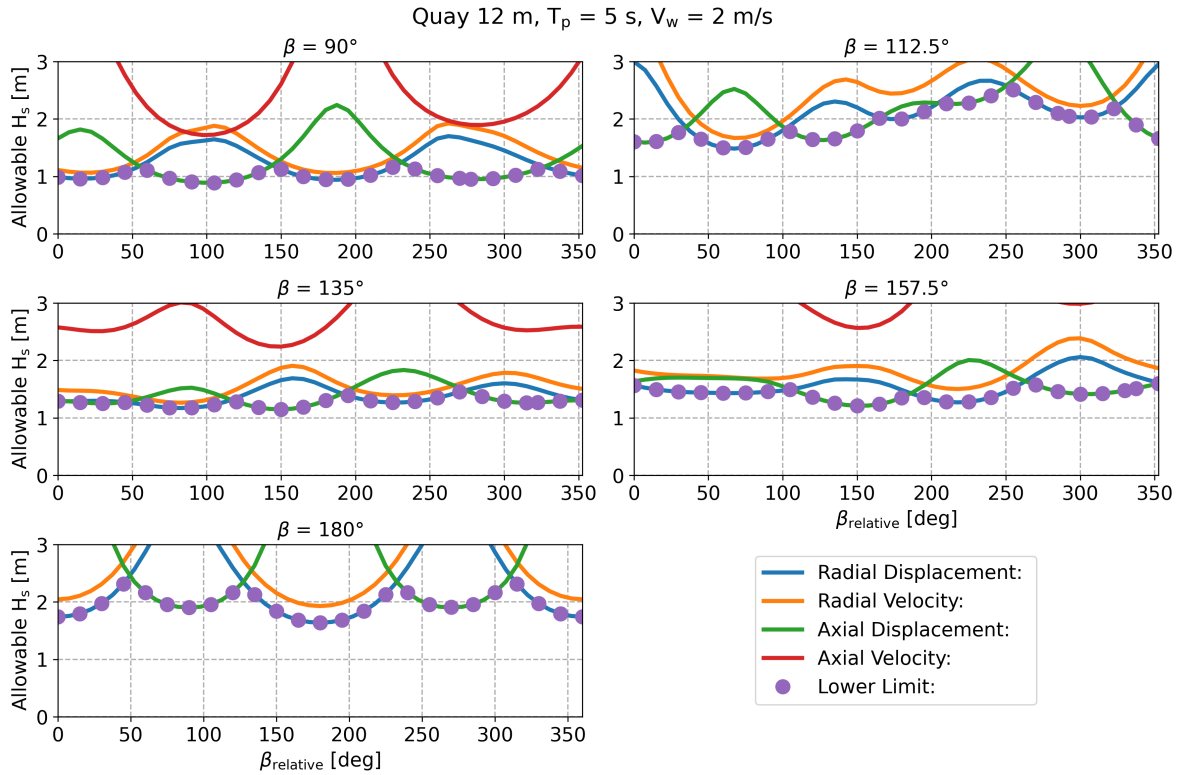


Figure 5.11: Limiting floater motions vs. relative nacelle heading for multiple wind and wave directions.

The figure above shows the effect of alternating the nacelle heading for one peak period and one wind speed. The effect of these variables, as well as the wind and wave direction, are considered to find the optimal nacelle and blade heading.

The effect of the peak period effect is analysed based on the wind/wave directions between $\beta = 90^\circ$ and $\beta = 180^\circ$. The effect is the same for the other half of the directions ($\beta = 180^\circ - \beta = 270^\circ$), as it is symmetric with respect to the $\beta = 180^\circ$ direction. These relevant plots are given in Appendix F.6.

Figure 5.12 shows the allowable H_s against the relative nacelle heading for a low wind speed ($V_w = 2$ m/s). A range of peak periods between 5 and 10 seconds are considered to study the effect it has. The optimal β_{relative} corresponds to the point where the graph reaches its maximum. It can be observed that for a low wind speed, the optimal relative heading varies with the peak period. For example, at $\beta = 112.5^\circ$, the optimum is 250° when the wave period is 5 s. For longer waves, there is a higher accordance in allowable wave height, but there still is a difference in the peak height. For a peak period of 10 s, the optimum heading is 225° . While for the other periods, this is 280° , approximately. The difference between peak periods is also noticeable for the other wind/wave directions.

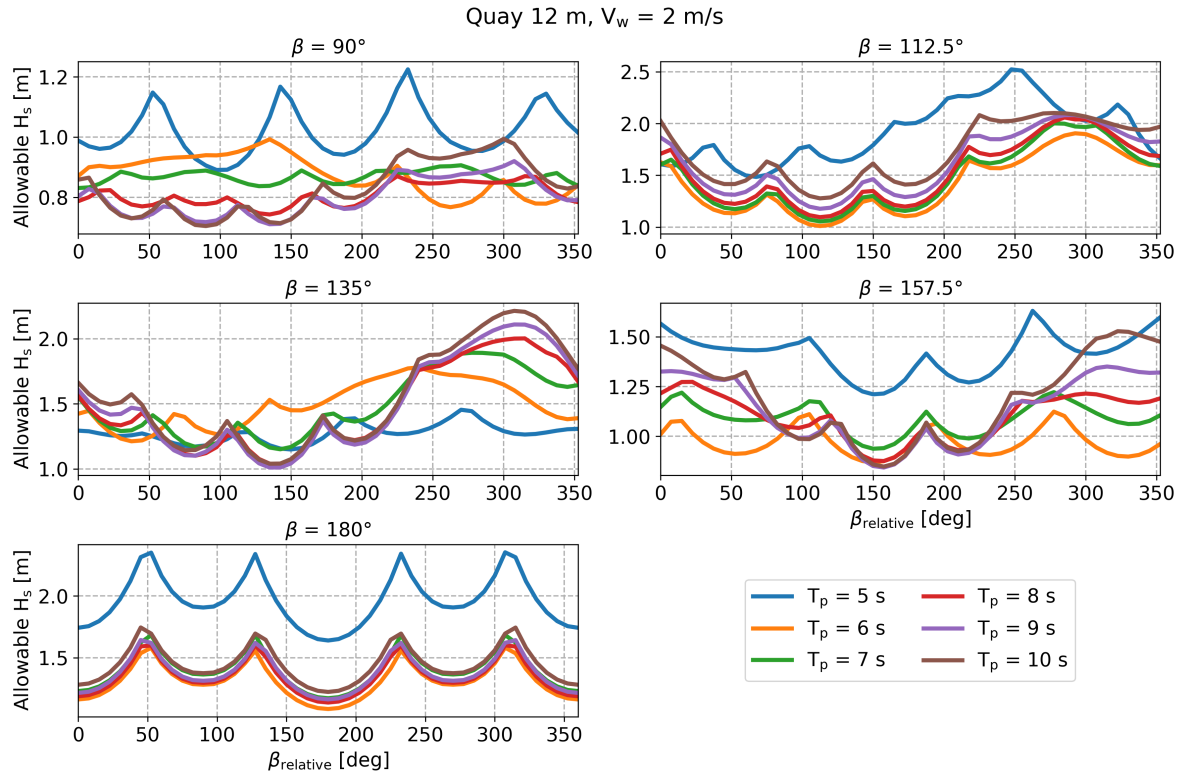


Figure 5.12: Relative nacelle heading dependent allowable H_s for different T_s and environmental directions at $V_w = 2$ m/s.

Figure 5.13 shows similar graphs as above, but for a higher wind speed ($V_w = 8$ m/s). The same range of peak periods is considered. It can be seen that for this higher wind speed, there is a higher accordance for the optimal relative heading between the different wave periods. The graphs have a more similar shape, and the peaks lie at the same relative heading. There are still small differences, especially for the waves with a peak period of 5 s that are parallel to the quay. For this case, the allowable wave height is significantly higher.

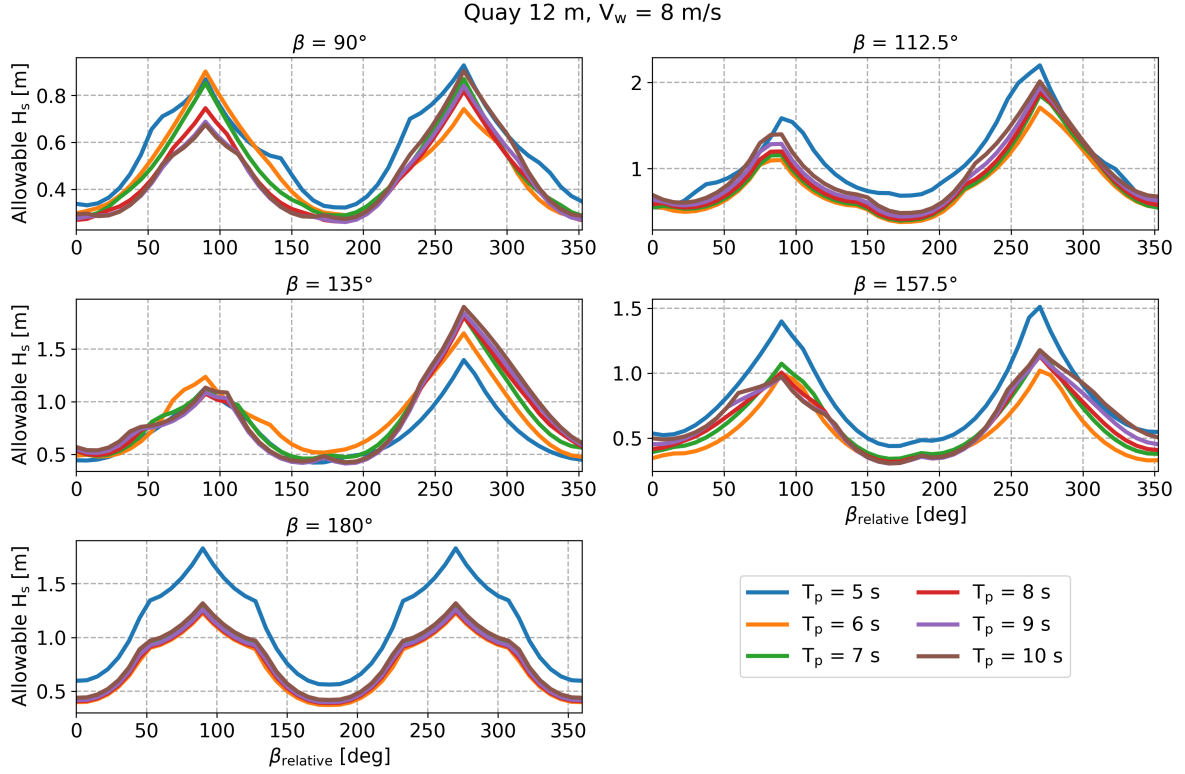


Figure 5.13: Relative nacelle heading dependent allowable H_s for different T_p and environmental directions at $V_w = 8$ m/s.

More details on the optimal relative nacelle heading are presented in Figure 5.14. These optimum headings correspond to the values where the allowable wave height peaks, as presented in Figures 5.12 and 5.13. These optimal values are presented on the vertical axis against the peak period for multiple wind speeds. A wind/wave direction of 135° is considered for this analysis. Similar results for other directions are presented in Appendix F.6.

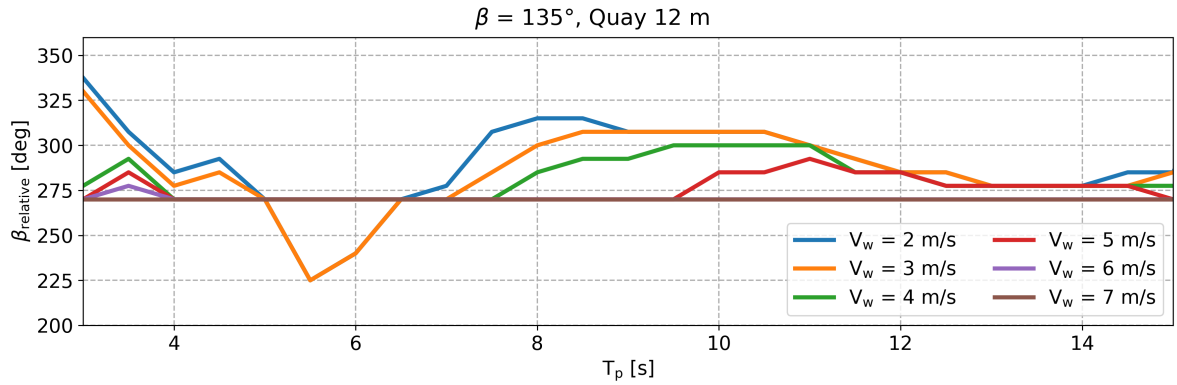


Figure 5.14: Optimal nacelle heading vs. T_p for different wind speeds.

It can be seen that for low wind speeds, the optimal nacelle heading fluctuates considerably for different peak periods. Hence, the optimal β_{relative} is strongly dependent on the peak period. For wind speeds of $V_w = 2$ m/s and $V_w = 3$ m/s, the optimum varies between 340° and 225° , approximately. The dependence on T_p reduces as the wind speed increases, which can be seen by the smaller fluctuations for the wind speeds between $V_w = 4$ m/s and $V_w = 6$ m/s. For this specific wind/wave direction, the optimal heading remains consistent across different wave periods when the wind speed exceeds

approximately 7 m/s, as indicated by the horizontal line. This is also true for most directions that are presented in the appendix. A few specific wave directions above 180° form an exception. Here, the optimal nacelle heading is independent of the wave period for wind speeds above 8 m/s.

5.3.2. Optimal Blade & Nacelle Heading

As explained before, the variables that influence the optimal heading of the blade and nacelle are wind speed, wind and wave direction, and peak period. To reduce the complexity, a blade and nacelle orientation should be found that ensures good and consistent performance across all peak periods. A blade orientation that is optimal for one peak period may perform poorly during another. Therefore, the optimal relative headings are determined for each combination of wind speed, wind/wave direction, and peak period. These individual optimal headings are then compared with each other, and the heading that performs the best across all peak periods is considered the overall optimum.

In Figure 5.15 are these optimum relative headings presented against the wind speed for multiple wind/wave directions. The continuous lines correspond to the wind and waves from one half of the environmental directions between $\beta = 90^\circ$ and $\beta = 180^\circ$. The dashed lines correspond to the other half of environmental directions between $\beta = 180^\circ$ and $\beta = 270^\circ$.

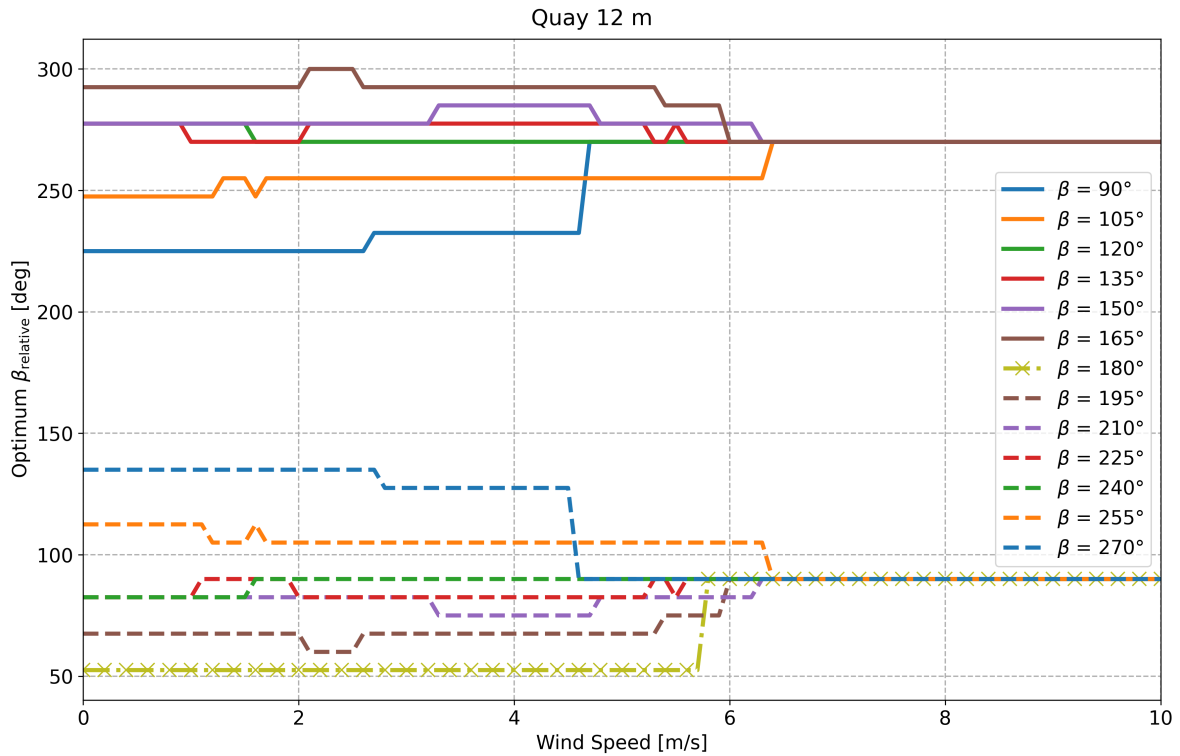


Figure 5.15: Optimal nacelle heading vs. V_w for different wind/wave directions.

In this figure, it can be noticed that the optimal values are mirrored with respect to the $\beta = 180^\circ$ relative heading. For low wind speeds, the optimal nacelle heading is governed by the waves and is highly dependent on the wind and wave direction. This can be seen by the large variation between the different wind/wave directions. When the wind speed increases, the optimal heading converges towards a single orientation for all conditions. From this follows that the contribution of the floater motions to the limiting motions reduces, as the blade motions become more dominant. When the wind speed exceeds 6.5 m/s, the optimal headings for all wind and wave directions have converged to $\beta_{\text{relative}} = 270^\circ$ and $\beta_{\text{relative}} = 90^\circ$. This indicates that the blade should be aligned with the wind and wave direction, with the blade root and blade tip positioned upwind, respectively. Two examples of this blade alignment for high wind speeds can be seen in the figure below. Figures 5.16a and 5.16b show the relative heading of 270° and 90° for two wind and wave directions, respectively.

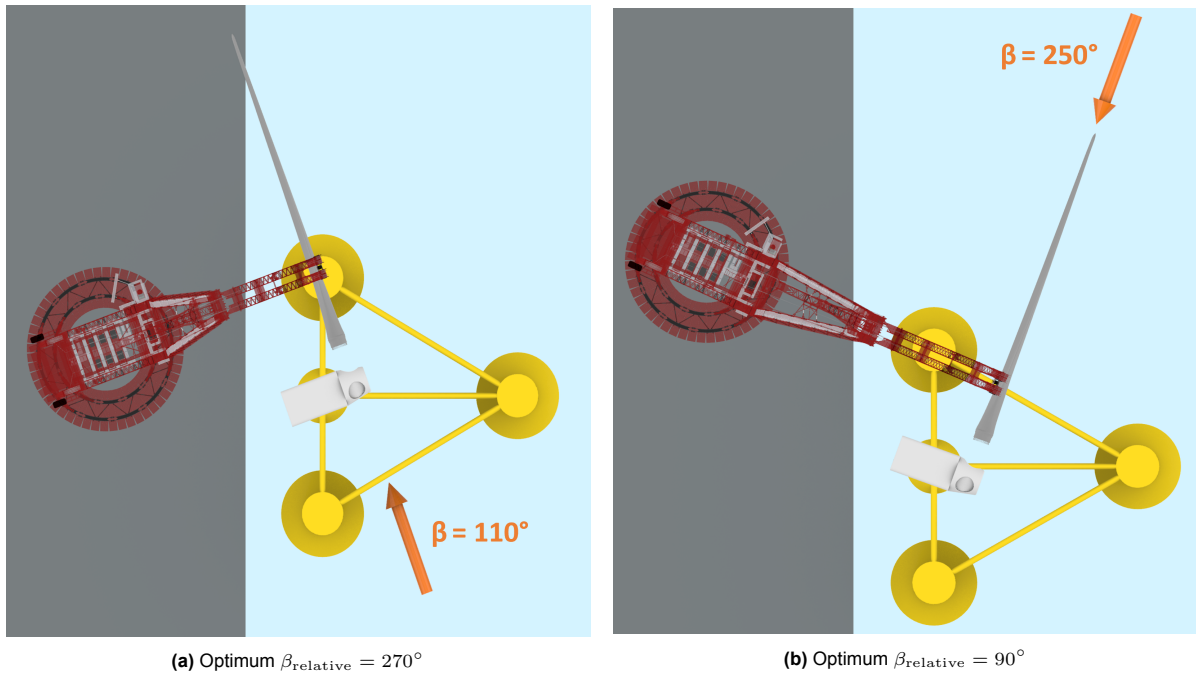


Figure 5.16: High wind speed blade installation heading for optimum $\beta_{\text{relative}} = 270^\circ$ and $\beta_{\text{relative}} = 90^\circ$.

It can be observed that it is advantageous to install the blade when the hub is rotated toward the floater's centre. This brings the hub closer to the COG of the floater and reduces the hub motions. This explains the difference between the optimum relative headings of $\beta_{\text{relative}} = 270^\circ$ and $\beta_{\text{relative}} = 90^\circ$ for the different wind and wave directions.

5.4. Operability

The results of the operability calculations are presented in this section. First, the allowable sea states for a large range of wind speeds and nacelle headings are calculated, similar to the previous section. The lower limit of all the individual relative motion components is used as the overall operational allowable environmental conditions. These conditions, as well as the maximum wind speed of 10 m/s, should be met during the 30 minutes installation time. The number of workable weather windows is determined based on the metocean data, described in section 3.5. The ratio between these workable weather windows and the maximum possible number of windows within the same period is the operability. This is split up into months for a better insight into the seasonal trends. Five different installation strategies are considered to study the effect these strategies have on the operability.

- Strategy 1: Fixed nacelle heading with the blade parallel to the quayside;
- Strategy 2: Fixed nacelle heading with the blade perpendicular to the quayside;
- Strategy 3: Fixed nacelle heading optimised for dominant wind/wave direction and low wind speeds;
- Strategy 4: Fixed nacelle heading optimised for dominant wind/wave direction and high wind speeds;
- Strategy 5: Alternating nacelle heading optimised for each environmental condition during installation.

5.4.1. Strategy 1: Fixed Nacelle Heading 0°

The first installation strategy is characterised by the nacelle that is not rotated. Hence, the blade is parallel to the quayside, as can be seen in Figure 5.17b. In this figure, the orange arrow indicates the dominant wind and wave direction for this location. The distance to the quayside is 12 m. This results in the operability, as presented in Figure 5.17a, for the exposed and sheltered locations.

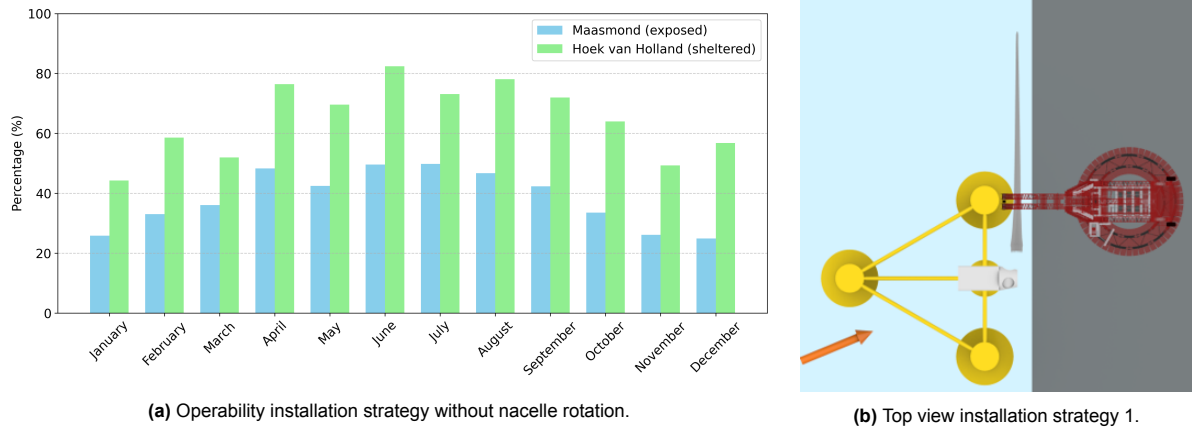


Figure 5.17: Operability & top view installation for strategy 1.

It can be seen that there is a significant difference between the exposed and sheltered locations. From this follows that the waves have an important contribution to the overall operability, as the wind conditions at both sites are almost the same. Moreover, it is clearly visible that the operability is highest in the summer months and lowest in the winter.

5.4.2. Strategy 2: Fixed Nacelle Heading -90°

The second installation strategy is characterised by the nacelle that is fixed with the blade perpendicular to the quayside. It is positioned above the quay, and the floater's distance to the quay is 12 m, as can be seen in Figure 5.18b. The operability for this installation strategy can be seen in Figure 5.18a.

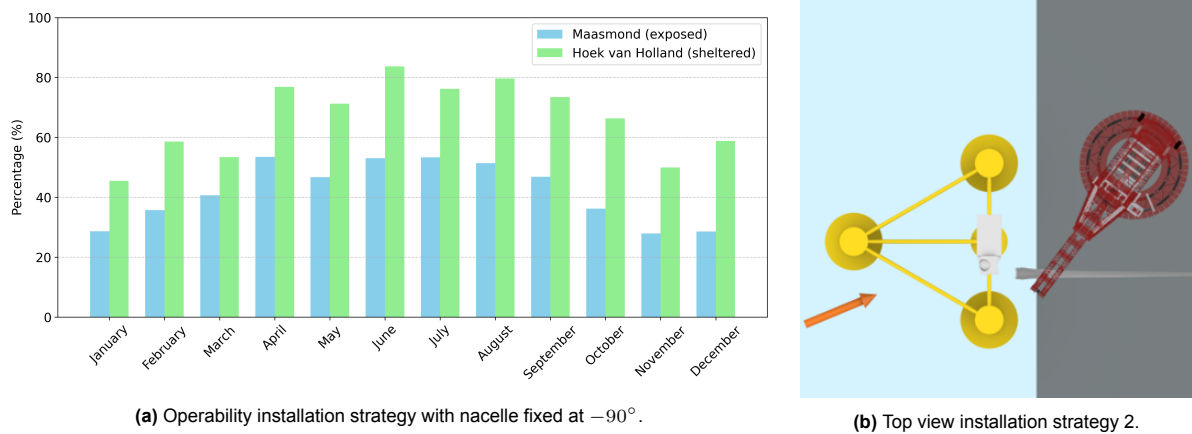


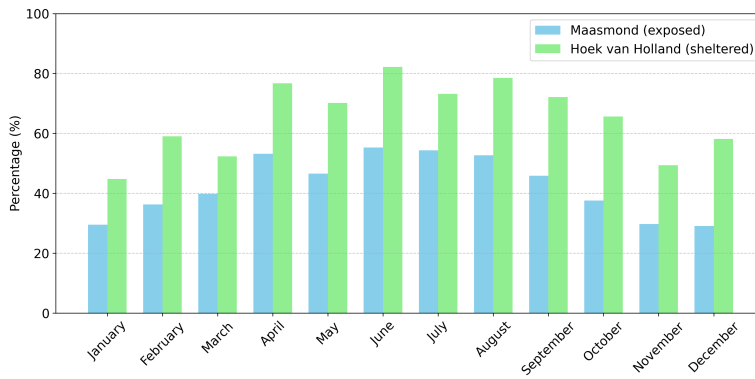
Figure 5.18: Operability & top view installation for strategy 2.

There is not a significant change in operability compared to the first strategy. A more detailed comparison between the strategies is presented in section 5.4.6.

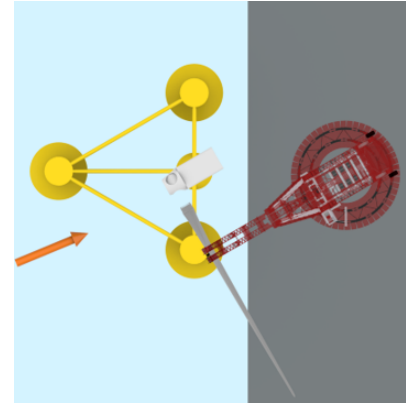
5.4.3. Strategy 3: Fixed Nacelle Heading Optimised for Low Wind Speeds

The third installation strategy involves the nacelle being fixed in a position optimised for low wind speeds that come from the dominant wind/wave direction. For both locations is west-southwest the dominant direction. As discussed in section 5.3.1, the optimal relative nacelle heading for all peak periods is dependent on the wind/wave direction for low wind speeds. For the dominant wind direction at this location, this corresponds to $\beta_{\text{relative}} = 352.5^\circ$. This is the optimum for low wind speeds up to 2.5 m/s, approximately. In combination with the dominant wind and wave direction, is the fixed nacelle heading $\psi_{\text{nacelle}} = -150^\circ$. Here the quayside distance is 12 m. An overview of this strategy is shown in combination with the dominant wind/wave direction in Figure 5.19b. This strategy results in the

operability as presented in Figure 5.19a. Similar to the previous strategies, there is not a significant change in operability for this strategy.



(a) Operability installation strategy optimised for low wind speeds.

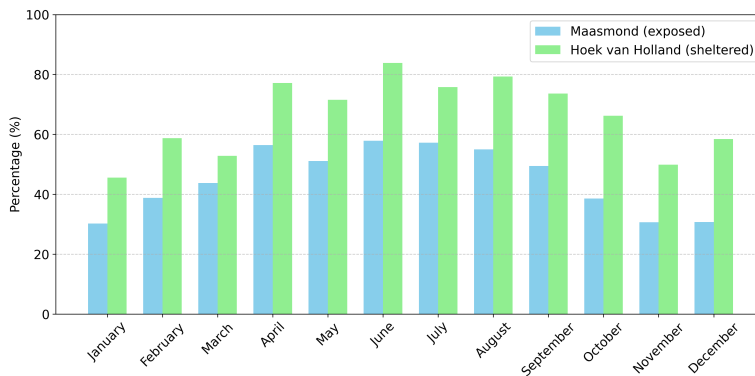


(b) Top view installation strategy 3.

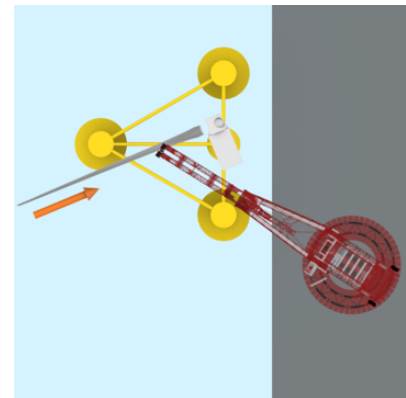
Figure 5.19: Operability & top view installation for strategy 3.

5.4.4. Strategy 4: Fixed Nacelle Heading Optimised for High Wind Speeds

The fourth installation strategy is similar to the previous strategy. The nacelle has a fixed orientation that is optimised for high wind speeds from the dominant wind/wave direction. For high wind speeds, the optimal relative nacelle heading for all peak periods is 90° . This results in an optimal nacelle heading of $\psi_{\text{nacelle}} = 112.5^\circ$, as can be seen in Figure 5.20a. For the quayside distance of 12 m, the operability for the exposed and sheltered locations is presented in Figure 5.20a. There is a small increase in operability noticeable, especially for the exposed location.



(a) Operability installation strategy optimised for high wind speeds.



(b) Top view installation strategy 4.

Figure 5.20: Operability & top view installation for strategy 4.

5.4.5. Strategy 5: Alternating Nacelle Heading

The fifth installation strategy is a more theoretical strategy compared to the previous strategies. It assumes that the nacelle and blade can change its orientation to the optimal heading for the present environmental conditions. For example, if the wind speed increases or the wave direction suddenly changes, the nacelle can be rotated to the optimal heading for the new conditions. This is not realistic in practice, because installation procedures are not that flexible. Furthermore, the nacelle might not be powered during the blade installation, which makes it impossible to change the heading frequently. However, it is useful to know what the theoretical maximum operability for this installation is. Moreover, it can be compared to the other strategies to see how they perform. The operability for this strategy, with a quayside distance of 12 m, can be seen in Figure 5.21.

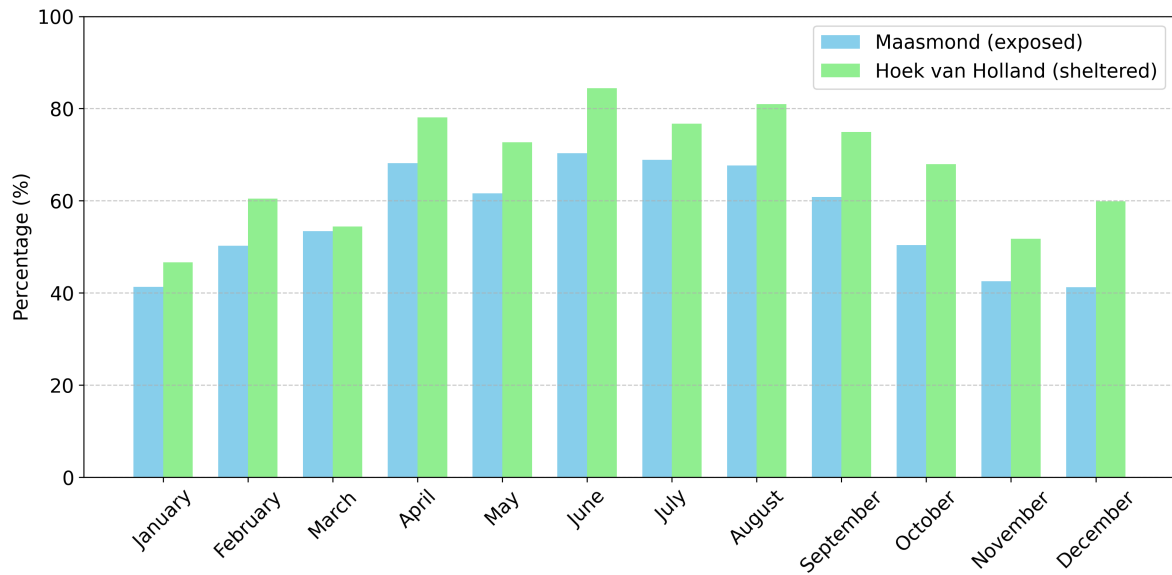


Figure 5.21: Operability installation strategy with rotating nacelle heading.

5.4.6. Installation Strategy Comparison

The operability results for the different installation strategies can be compared for the sheltered and exposed location, as shown in Figures 5.22 and 5.23, respectively.

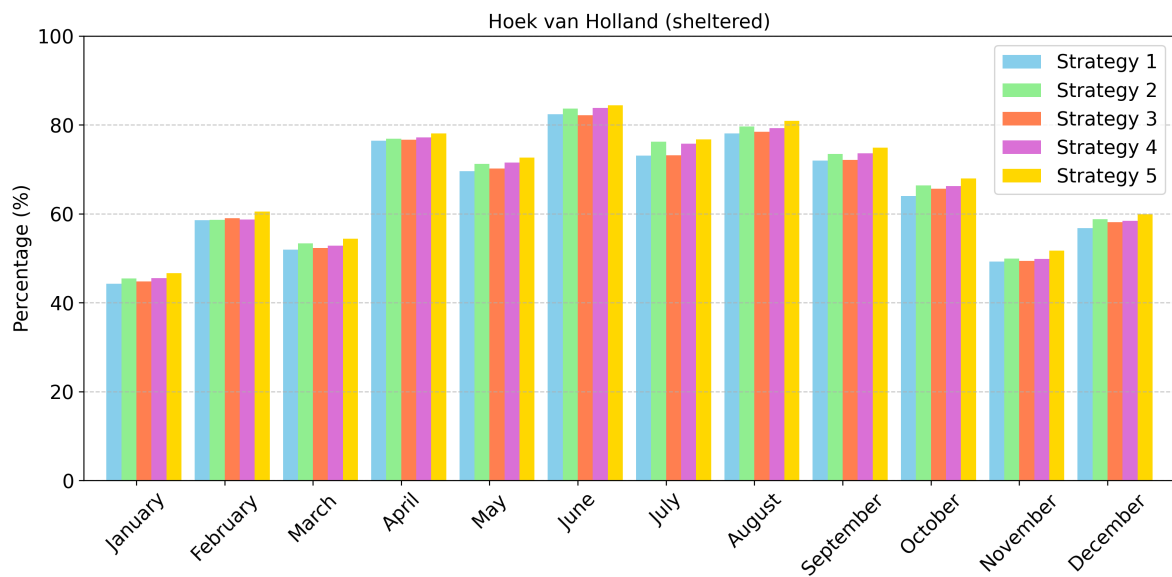
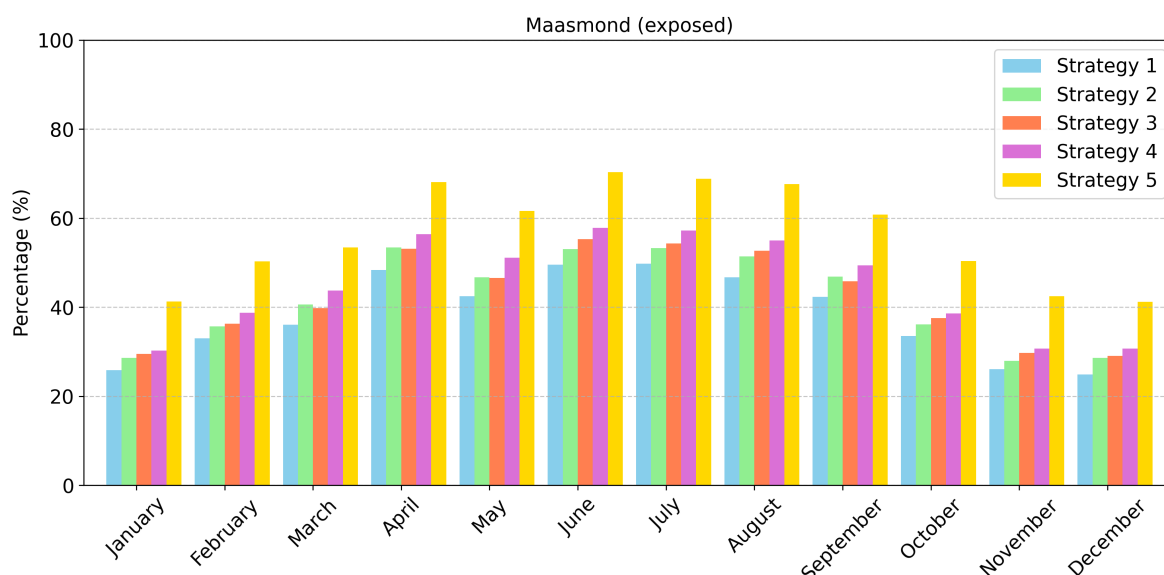


Figure 5.22: Comparison of operability for five strategies at the sheltered site.

At the sheltered location, it can be seen that strategy 1 ($\psi_{\text{nacelle}} = 0^\circ$) is the worst performing strategy. However, the difference between all the strategies is small. Table 5.3 gives the average operability over a year for the two locations and the installation strategies. This indicates that the gap between the theoretical maximum and the worst-performing strategy is just 2 percentage points. For the exposed location, the differences between the strategies are more significant, namely 18 percentage points. The operability comparison at the exposed location can be seen in Figure 5.23.

Table 5.3: Comparison of yearly operability for five strategies

Strategy	Sheltered location	Exposed location
Strategy 1	65%	38%
Strategy 2	66%	42%
Strategy 3	65%	43%
Strategy 4	66%	45%
Strategy 5	67%	56%

**Figure 5.23:** Comparison of operability for five strategies at the exposed site.

It can be observed that the four practicable strategies result in a considerably lower operability than what is theoretically possible with strategy 5. Furthermore, strategy 1 is the worst performing strategy. Based on these results, it can be concluded that strategy 4, where the blade heading is optimised for high wind speed, is the best-performing strategy that is applicable in practice.

5.4.7. Effect Quayside Distance on Operability

Based on the sensitivity study performed in section 5.2.1, it was found that the distance of 12 m has the best overall performance in terms of allowable wave height. To see how this distance influences the operability of the operation, the operability of the different quayside distances is compared. Installation strategy 4 is used for this comparison, as it is the best-performing strategy that is applicable in practice. Figure 5.24 shows the operability at the exposed location for the five quayside distances as considered before.

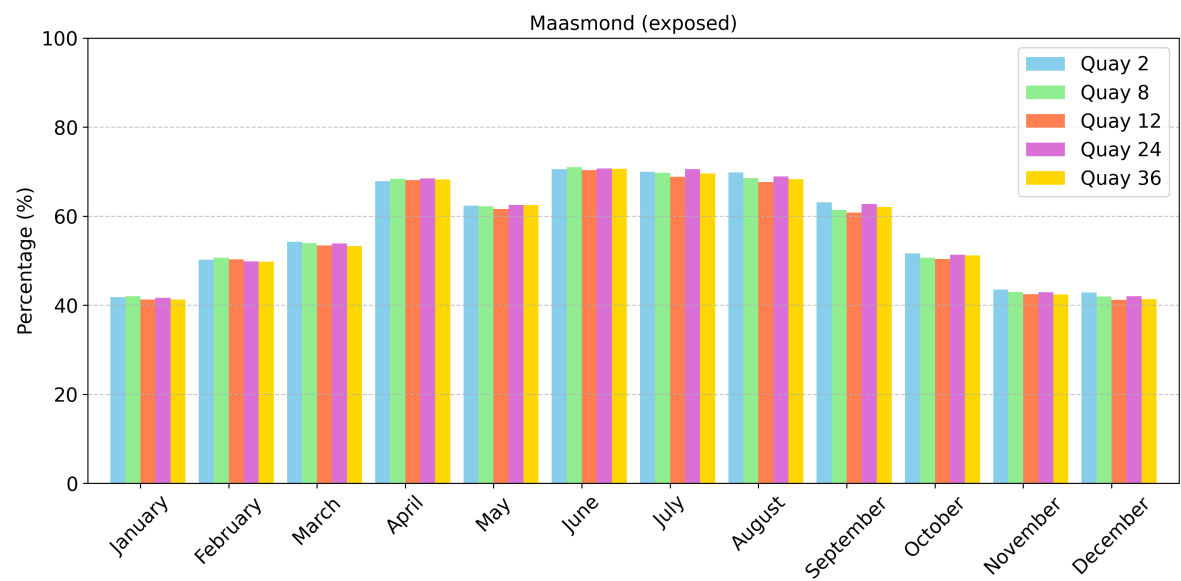


Figure 5.24: Comparison of operability for five quayside distances at the exposed site.

It can be observed that there are no significant variations between the different distances, as concluded earlier. However, the small differences that do exist indicate that the 12 m distance is not the best-performing distance. Instead, the closest floater at 2 m has a slight advantage over the others for most months. This can be explained by the fact that the majority of the waves at this location have a low peak period. For these shorter waves, the smaller quayside distance performs better than the others, as demonstrated in Figure 5.9. This result indicates that the distance to the quayside has no significant impact on operability, allowing it to be determined based on other factors, such as crane size.

5.4.8. Wind & Waves Importance

It is interesting to understand the relative importance of the different environmental conditions on the operability. These insights can improve the forecasting of installation windows, which results in better planning. To find the relative importance of the significant wave height, peak period, and wind speed, the sensitivity of the operability to these variables is studied. Each of these variables is decreased and increased in the range of -20% to 20% , while the others remain constant. The results can be seen in Figure 5.25. For these calculations is installation strategy 4 used. Each line represents the change of an environmental condition as they are at the two locations.

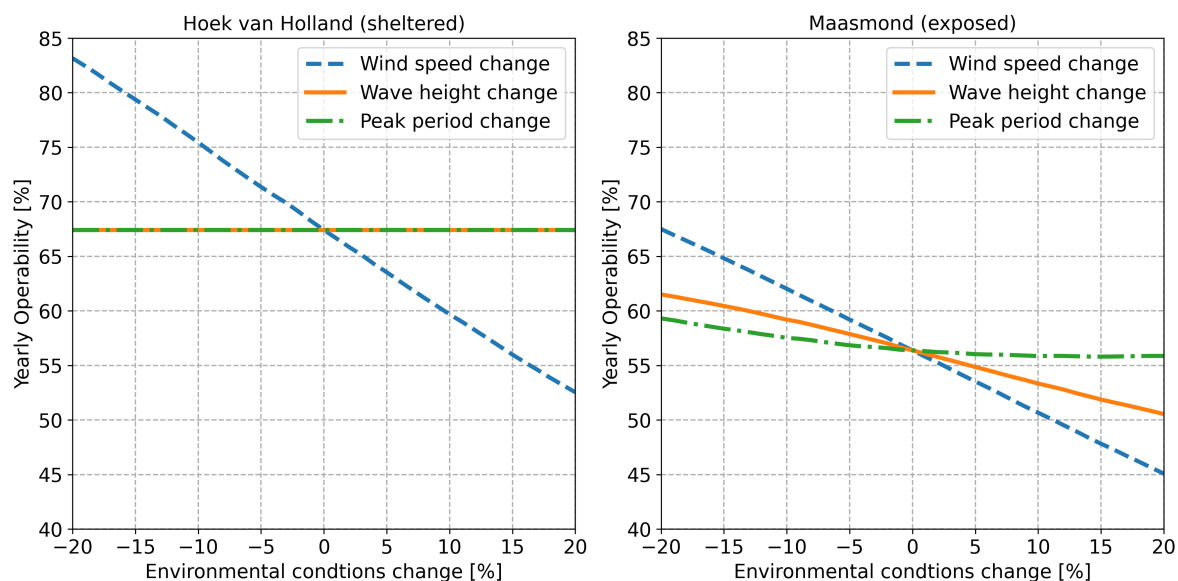


Figure 5.25: Sensitivity of operability to environmental conditions.

It can be observed that at the sheltered location, the yearly operability does not change if the significant wave height or the peak period increases or decreases. It does change when the wind speed is altered, which means that at this location the wind speed is governing the operability. At the exposed location, there is a change in operability when the wave conditions change. Especially, the significant wave height has an effect. However, similar to the sheltered location, the wind speed is the dominating factor that determines the operability.

Conclusions & Recommendations

6.1. Conclusions

This research studies, in the frequency domain, the operability of a wind turbine blade installation on a semi-submersible floating wind foundation using a quayside crane. It focuses on the critical alignment and mating phases of the single-blade installation method. Multiple aspects have been studied to find the operability of the installation.

Firstly, the operational limits imposed by environmental conditions during the wind turbine blade installation are expressed in terms of relative motions. The relative distance and velocity between the blade root and turbine hub should remain within a cylindrical safety boundary. This safety boundary is composed of a radial boundary as a circle around the hub and an axial boundary perpendicular to the hub. For the alignment phase, the limits are defined in terms of relative displacements and the misalignment rate. During the mating phase, the limits are described by the relative velocity and the probability of exceeding a critical impact velocity.

Secondly, the motions of the semi-submersible foundation and the blade are moving independently from each other, so they can be studied separately. The floater motions next to a quayside can be modelled by performing a wave diffraction-radiation analysis with a 3D panel model that includes a vertical wall. This yields the hydrodynamic properties which can be used, in combination with additional linearised viscous damping, to solve the equations of motion. It is important to take the shallow draft effect into account while determining the additional damping. The obtained response amplitude operator is combined with a shallow water TMA spectrum to arrive at the motion response spectrum. Thereafter, the corresponding spectral parameters are used to find the characteristic displacement and velocity that correspond to a specific sea state.

Alongside the floater motions, the blade motions contribute to the relative motions. Although a detailed analysis of the blade is beyond the scope of this research, its wind-induced motions can be estimated by modelling the blade as a pendulum system with two DOFs that are attached to a fixed crane. In this simplified model, the blade and yoke are represented as a point mass, to which the taglines are attached as spring-damper systems that help reduce the blade's motions. A spectral analysis can be conducted to obtain the characteristic blade motions that correspond to specific wind conditions.

The blade's contribution to the relative motions lowers the allowable sea states where combined motions stay within operational limits. The largest blade motions occur in the radial direction when the wind is perpendicular to the blade. When the blade is aligned with the wind, the axial motions become dominant, but they remain small. On the floater side, the limiting motion component, mostly the axial displacement, is determined by the wave direction and peak period. The distance to the quayside has minimal effect on these limiting motions. However, the nacelle and blade heading relative to wind and waves significantly affect the allowable environmental conditions. These conditions can be increased by optimising the nacelle heading. For low wind speeds, the optimum relative heading is dependent on the wind and wave direction. Whereas for high wind speeds, the blade motions become more dominant

which favours the alignment of the blade with the wind direction.

Improvements in operability can be made by changing this relative heading of the nacelle and blade. The best practical applicable installation strategy is to select a heading that is optimal for high wind speeds from the dominant wind direction. In these conditions, the optimal blade orientation is aligned with the wind. Additionally, rotating the nacelle towards the floater's COG helps in reducing the hub motions. Furthermore, the operability is highly influenced by the installation site's location. For the sheltered and exposed areas in the Port of Rotterdam considered in this study, the sheltered harbour shows a 20 percentage point advantage due to calmer wave conditions. However, wind speed has an even greater impact on operability, as it is the dominant factor determining successful installation.

In conclusion, a wind turbine blade installation on a semi-submersible floating wind foundation is a wind-governed operation for which the operability is greatly impacted by the location of the installation site. For a location with sufficient shelter, a yearly operability in the order of 65% could be achieved. For a more exposed location, this reduces to approximately 45%. This is achieved by utilising an installation strategy where the blade is aligned with the dominant wind direction. These operability results are specified for two specific locations and obtained with a simplified model, especially for the blade motions. So these results cannot be used for every installation, but they give a good insight into the operability and the governing environmental conditions.

6.2. Recommendations

In this research, multiple assumptions were made to simplify the problem. However, this gives the opportunity for follow-up research to study the influence of these assumptions and shortcomings.

The frequency domain approach, used in this research, is computationally efficient and suitable for preliminary studies. However, it has limitations in capturing nonlinear effects. For a better understanding of the blade installation process, a time domain simulation would be beneficial. This would allow for taking nonlinear behaviour into account, such as slow-drift motions. It would also enable the study of transient effects and extreme events during the installation. As an example, wind gusts are a rapid change in wind speed that could be captured with a time domain simulation.

The simplified pendulum model used for the blade motions in this research provides a basic understanding of the blade's dynamic response. However, a more detailed blade model should be considered to gain more insight into the motions. This could involve considering the blade's yaw motion and flexibility because this changes the wind inflow and as a result the motions. Furthermore, the interaction between the blade and the turbine hub caused by wind flowing across the turbine, which directly influences the blade's motions, could also be studied. Additionally, an active tagline control system could help in reducing the blade motions during the critical installation phases. Since these are complex calculations, a time domain simulation is a more suited modelling strategy.

For the floater motions, the mooring loads are not considered in this study. It is recommended to study the effect of different mooring layouts, to see whether this has a significant effect on the floater motions. Incorporating a mooring system into the model would provide a more realistic representation of the installation conditions.

It is also recommended to include the environment loads in more detail in the model. Only wave loads are considered for the floating structure in this study. However, wind is also acting on the floater and wind turbine. Especially, when the first and second blades are already installed, the wind loads are expected to be significant. Additionally, at locations with a high tidal range, strong currents can rise close to a harbour access. For an installation in these conditions, the current should also be included in the model.

Finally, all the installation equipment and the turbine-floater connection are assumed to be rigid. It should be studied whether this is a valid assumption for each of the components. For example, the crane is expected to oscillate due to wind loads, which gives more degrees of freedom to the system.

By addressing these recommendations, a better insight into the details of blade installation on a semi-submersible foundation can be obtained. Some of these enhancements, such as applying wind loads to the floater, can be explored using the frequency domain model presented in this thesis. However, for

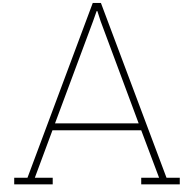
a more detailed motion analysis, a time domain simulation is more suitable. This enables estimating a more accurate operability for a specific location and with a defined installation strategy based on the findings of this study.

References

- Acero, Wilson Guachamin et al. (2016). "Methodology for assessment of the operational limits and operability of marine operations". In: *Ocean Engineering* 125, pp. 308–327.
- Aerospaceweb (2024). *Drag of Cylinders & Cones*. URL: <https://aerospaceweb.org/question/aerodynamics/q0231.shtml> (visited on Aug. 7, 2024).
- An, Song and Odd M. Faltinsen (2013). "An experimental and numerical study of heave added mass and damping of horizontally submerged and perforated rectangular plates". In: *Journal of Fluids and Structures* 39, pp. 87–101.
- Barooni, Mohammad et al. (2022). "Floating Offshore Wind Turbines: Current Status and Future Prospects". In: *Energies* 16.1, p. 2.
- Brunel (2021). *The pros and cons of onshore & offshore wind*. URL: <https://www.brunel.net/en/blog/renewable-energy/onshore-offshore-wind> (visited on Aug. 7, 2024).
- BVG-Associates (2023). *Guide to a Floating Offshore Wind Farm*.
- DNV-OS-H101 (2011). *Marine Operations, General*. DNV Oslo, Norway.
- DNV-RP-C205 (2021). *Environmental conditions and environmental loads*. DNV Oslo, Norway.
- DNVGL-OTG-13 (2019). *Prediction of air gap for column stabilised units*. DNV Oslo, Norway.
- DNVGL-ST-N001 (2018). *Marine Operations*. DNV Oslo, Norway.
- Enel-Green-Power (23). *How is wind formed?* URL: <https://www.enelgreenpower.com/learning-hub/gigawhat/search-articles/articles/2023/05/wind-formation> (visited on Aug. 7, 2024).
- Equinor (2023). *The world's largest floating offshore wind farm officially opened*. URL: <https://www.equinor.com/news/20230823-hywind-tampen-officially-opened> (visited on Aug. 7, 2024).
- Faltinsen, Odd (1993). *Sea loads on ships and offshore structures*. Vol. 1. Cambridge university press.
- Gaertner, Evan et al. (2020). *IEA wind TCP task 37: definition of the IEA 15-megawatt offshore reference wind turbine*. Tech. rep. National Renewable Energy Lab.(NREL), Golden, CO (United States).
- Github (2024). *IEA-15-240-RWT*. URL: https://github.com/IEAWindTask37/IEA-15-240-RWT/blob/master/Documentation/IEA-15-240-RWT_tabular.xlsx (visited on Aug. 7, 2024).
- GustoMSC (2024). *Tri-Floater Floating Offshore Wind Turbine Foundation*. URL: <https://www.nov.com/products/tri-floater-floating-offshore-wind-turbine-foundation> (visited on Aug. 7, 2024).
- Heerema (2022). *Floating to Floating offshore wind installation method*. URL: <https://www.heerema.com/insights/floating-to-floating-installation-method> (visited on Aug. 7, 2024).
- Holthuijsen, L.H. (2007). *Waves in Oceanic and Coastal Waters*. Delft: Cambridge University Press.
- Ideol, BW (2024). *From Concept to Reality, Our Assets, Our Projects*. URL: <https://www.bw-ideol.com/en/our-projects> (visited on Aug. 7, 2024).
- ITTC - Recommended Procedures and Guidelines (2011). *Numerical Estimation of Roll Damping*. Tech. rep. 7.5-02-07-04.5. ITTC, pp. 1–33. URL: <https://ittc.info/media/5748/75-02-07-045.pdf>.
- Jiang, Zhiyu (2018). "The impact of a passive tuned mass damper on offshore single-blade installation". In: *Journal of Wind Engineering and Industrial Aerodynamics* 176, pp. 65–77.
- (2021). "Installation of offshore wind turbines: A technical review". In: *Renewable and Sustainable Energy Reviews* 139.
- Journée, J.M.J. and W.W. Massie (2001). "Offshore hydromechanics". In: *Delft University of Technology*.
- Kuijken, L (2015). "Single Blade Installation for Large Wind Turbines in Extreme Wind Conditions". In: Lee, C-H and JN Newman (2005). "Computation Of Wave Effects Using The Panel Method". In: *WIT Transactions on State-of-the-art in Science and Engineering* 18.
- Lee, C-H, JN Newman, and X Zhu (1996). "An extended boundary integral equation method for the removal of irregular frequency effects". In: *International Journal for Numerical Methods in Fluids* 23.7, pp. 637–660.
- Leeuw, Koen de (2019). *Single lift blade alignment for large offshore wind turbines*.

- Liftra (2024). *LT975 - Blade Dragon*. URL: <https://liftra.com/products/lt975-blade-dragon> (visited on Aug. 7, 2024).
- Longridge, Kent (2023). *Floating wind: what are the mooring options?* <https://acteon.com/blog/floating-wind-mooring-options/>.
- Lopez-Pavon, Carlos and Antonio Souto-Iglesias (2015). "Hydrodynamic coefficients and pressure loads on heave plates for semi-submersible floating offshore wind turbines: A comparative analysis using large scale models". In: *Renewable Energy* 81, pp. 864–881.
- Mammoet (2024). *Mammoet - PTC 140 DS Ring Crane*. URL: <https://www.mammoet.com/equipment/cranes/ring-cranes/ptc-140-ds/>.
- Mei, Xuan and Min Xiong (2021). "Effects of second-order hydrodynamics on the dynamic responses and fatigue damage of a 15 mw floating offshore wind turbine". In: *Journal of Marine Science and Engineering* 9.11.
- Molin, Bernard, Fabien Remy, and Thierry Rippol (Sept. 2007). "Experimental study of the heave added mass and damping of solid and perforated disks close to the free surface". In: *Proceedings of the 12th International Maritime Association of the Mediterranean (IMAM) 2007*. Varna, Bulgaria. URL: <https://hal.archives-ouvertes.fr/hal-00456812>.
- Municipality of Rotterdam (2014). *Topographical Map Port of Rotterdam*. Map. Created by the Municipality of Rotterdam.
- NES-Fircroft (2022). *A Brief History Of Wind Power*. URL: <https://www.nesfircroft.com/resources/blog/a-brief-history-of-wind-power/> (visited on Aug. 7, 2024).
- NEWA (2024). *New European Wind Atlas*. URL: <https://map.neweuropeanwindatlas.eu> (visited on July 3, 2024).
- Ørsted (2024). *Making green energy affordable*. URL: <https://orsted.com/en/insights/white-papers/making-green-energy-affordable/1991-to-2001-the-first-offshore-wind-farms> (visited on Aug. 7, 2024).
- PMI-Industries (2016). *Pros and Cons of Floating Platforms in Marine Renewable Energy*. URL: <https://pmiind.com/pros-cons-floating-platforms-marine-renewable-energy/> (visited on Aug. 7, 2024).
- Principle-Power (2021). *KOWL: World's largest floating windfarm fully operational*. URL: <https://www.principlepower.com/news/kowl-worlds-largest-floating-windfarm-fully-operational> (visited on Aug. 7, 2024).
- Ren, Zhengru et al. (2023). "Underactuated control and analysis of single blade installation using a jackup installation vessel and active tugger line force control". In: *Marine Structures* 88, p. 103338.
- Rijkswaterstaat (2024). *Nieuwe Waterweg*. URL: <https://www.rijkswaterstaat.nl/water/vaarweg/enoverzicht/nieuwe-waterweg> (visited on Aug. 7, 2024).
- Ropes, Dynamica (2024). *Dynamica Taglines*. URL: <https://dynamica-ropes.com/products/taglines/> (visited on Aug. 7, 2024).
- Sarpkaya, T., M. Isaacson, and J. V. Wehausen (June 1982). "Mechanics of Wave Forces on Offshore Structures". In: *Journal of Applied Mechanics* 49.2, pp. 466–467.
- Somoano, M et al. (2021). "Influence of turbulence models on the dynamic response of a semi-submersible floating offshore wind platform". In: *Ocean Engineering* 237.
- Tacx, Jochem (2019). *Floating Wind Structures and Mooring Types*. URL: <https://www.energyfacts.eu/floating-wind-structures-and-mooring-types/> (visited on Aug. 7, 2024).
- Tao, Longbin and Shunqing Cai (2004). "Heave motion suppression of a Spar with a heave plate". In: *Ocean engineering* 31.5-6, pp. 669–692.
- Tao, Longbin, Bernard Molin, et al. (2007). "Spacing effects on hydrodynamics of heave plates on offshore structures". In: *Journal of Fluids and Structures* 23.8, pp. 1119–1136.
- Tao, Longbin and Krish Thiagarajan (2003). "Low KC flow regimes of oscillating sharp edges. II. Hydrodynamic forces". In: *Applied ocean research* 25.2, pp. 53–62.
- Ummels, Bart (2024). personal communication.
- UNFCCC (2024). *The Paris Agreement*. URL: <https://unfccc.int/process-and-meetings/the-paris-agreement> (visited on Aug. 7, 2024).
- Veritas, Det Norske (2023). *Energy Transition Outlook 2023*.
- Verma, Amrit Shankar, Zhiyu Jiang, Zhengru Ren, et al. (2019). "Response-based assessment of operational limits for mating blades on monopile-type offshore wind turbines". In: *Energies* 12.10, p. 1867.

- Verma, Amrit Shankar, Zhiyu Jiang, Nils Petter Vedvik, et al. (2019). "Impact assessment of a wind turbine blade root during an offshore mating process". In: *Engineering Structures* 180, pp. 205–222.
- Vu, Ky H, Benoit Chenu, and Krish P Thiagarajan (2004). "Hydrodynamic damping due to porous plates". In: *Proceedings of the WSEAS international conference on fluid mechanics, Corfu*. Citeseer, pp. 17–19.
- Wadhwa, Hemlata and Krish P Thiagarajan (2009). "Experimental assessment of hydrodynamic coefficients of disks oscillating near a free surface". In: *International Conference on Offshore Mechanics and Arctic Engineering*. Vol. 43444, pp. 435–441.
- Wind, X1 (2024). *NextFloat Project: pre-commercial unit in the French Mediterranean Sea*. URL: <https://www.x1wind.com/projects/nextfloat-project-pre-commercial-unit-in-the-french-mediterranean-sea/> (visited on Aug. 7, 2024).
- WindEurope (2023). *Floating wind is making great strides*. URL: <https://windeurope.org/newsroom/news/floating-wind-is-making-great-strides/> (visited on Aug. 7, 2024).
- Zhang, Lixian et al. (2023). "Experimental investigation on the hydrodynamic effects of heave plates used in floating offshore wind turbines". In: *Ocean Engineering* 267.
- Zhao, Yuna (2019). *Numerical Modelling and Dynamic Analysis of Offshore Wind Turbine Blade Installation*.



Irregular Frequencies

A well-known issue could arise when the boundary-integral equations are solved using the free-surface Green function. For a certain set of discrete frequencies, there is no solution or a non-unique solution to the problem. These so-called irregular frequencies occur due to the continuation of the outer fluid field into the imaginary inner fluid field of the floating body. The eigenfrequencies of the inner fluid correspond to the irregular frequencies. Since this is caused by the imaginary inner fluid, it is not associated with a physical problem. It is a mathematical and numerical technicality. In most applications, these irregular frequencies are out of the frequency range of interest, which limits the impact. However, since the numerical result is unreliable, it should be handled correctly to avoid modelling errors. Lee, Newman, and Zhu (1996) describe a methodology to remove the irregular frequency effect. WAMIT also includes a function for the removal of this effect. Figure A.1 shows the wave radiation damping of the Tri-Floater in shallow water. This figure is aimed at visualising the effect of irregular frequency removal by WAMIT that is used throughout this research. It can be seen that the peak around 1.8 rad/s in heave, roll, and pitch is no longer present when the irregular frequencies are removed by WAMIT.

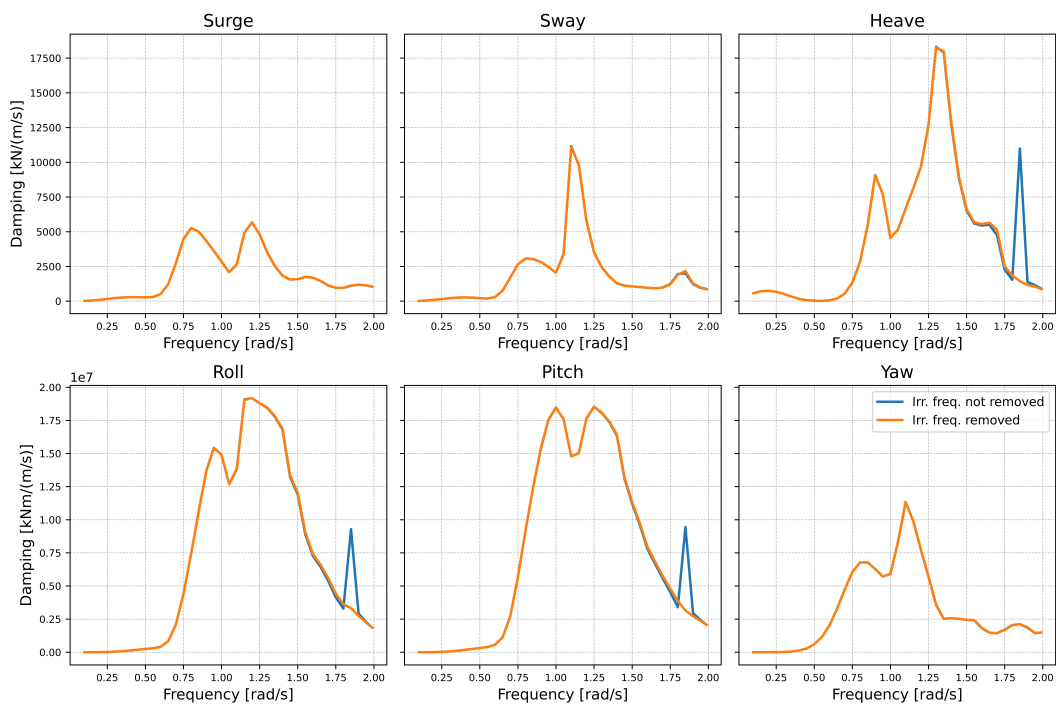


Figure A.1: Effect of irregular frequency removal on the wave radiation damping.

B

Floater Meshes

B.1. Triangular & Quad Mesh Elements

In a preliminary study, it was found that a mesh with triangular elements require more elements, and therefore computational time, to obtain the same level of accuracy as meshes with quad elements. Three mesh sizes (coarse, medium, fine) with approximately the same amount of elements were used for both the triangular and quad mesh elements. The Tri-Floater without quayside has been used to study this effect. The results for the added mass in pitch can be seen in figure B.1. It can be noted that the quad meshes converge faster to the most accurate results of the finest mesh, while the triangular meshes needs a fine mesh to approach this level of accuracy.

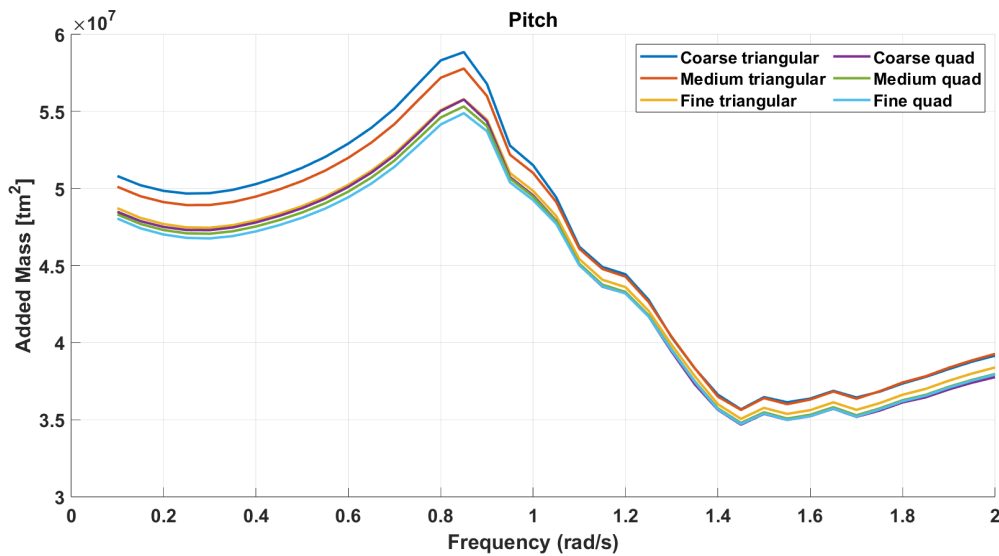
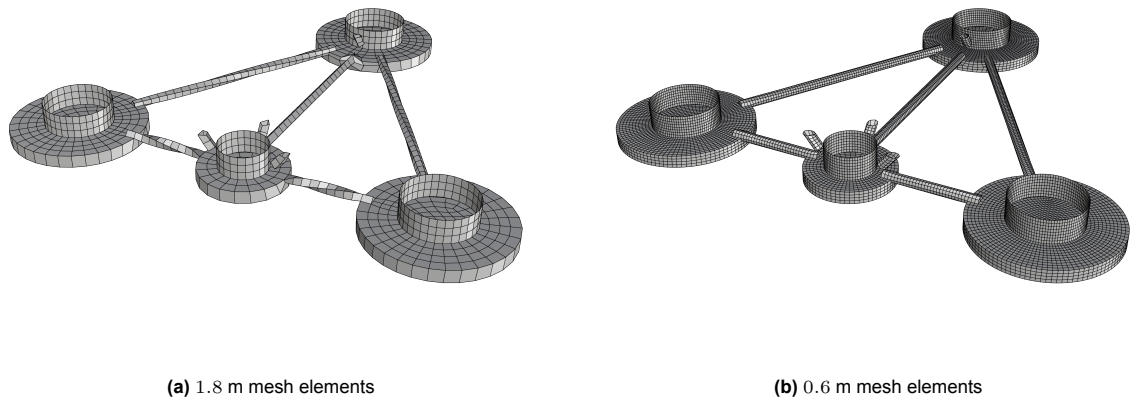


Figure B.1: Added mass for meshes with triangular and quad mesh elements

B.2. Mesh Convergence Study

Different mesh element sizes have been used for the mesh convergence study as discussed in section 4.1.3. The meshes with the largest (1.8 m) and smallest (0.6 m) mesh element sizes can be seen in figure B.2.

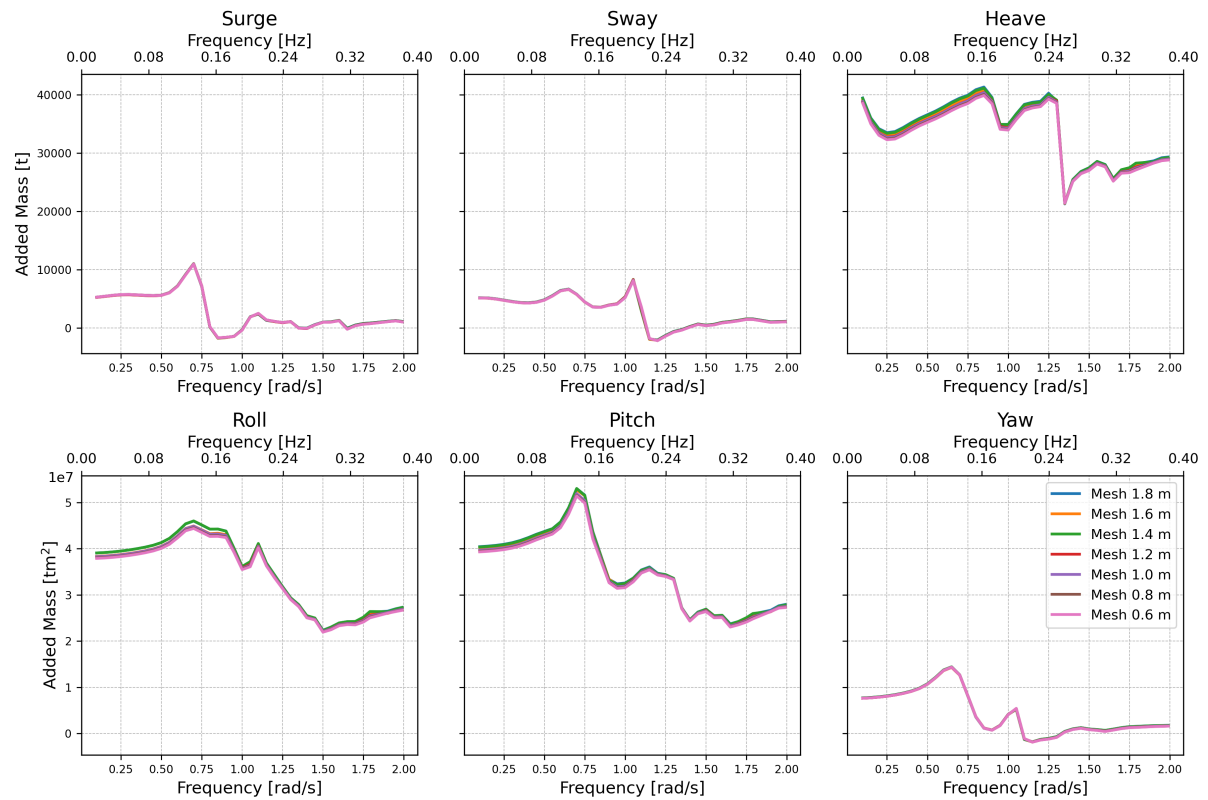


(a) 1.8 m mesh elements

(b) 0.6 m mesh elements

Figure B.2: Submerged Tri-Floater meshes with 1.8 m and 0.6 m mesh element sizes.

The figures below show the added mass, potential damping and wave force RAO for the different mesh sizes as described in section 4.1.3.

**Figure B.3:** Added mass in six DOF for seven meshes

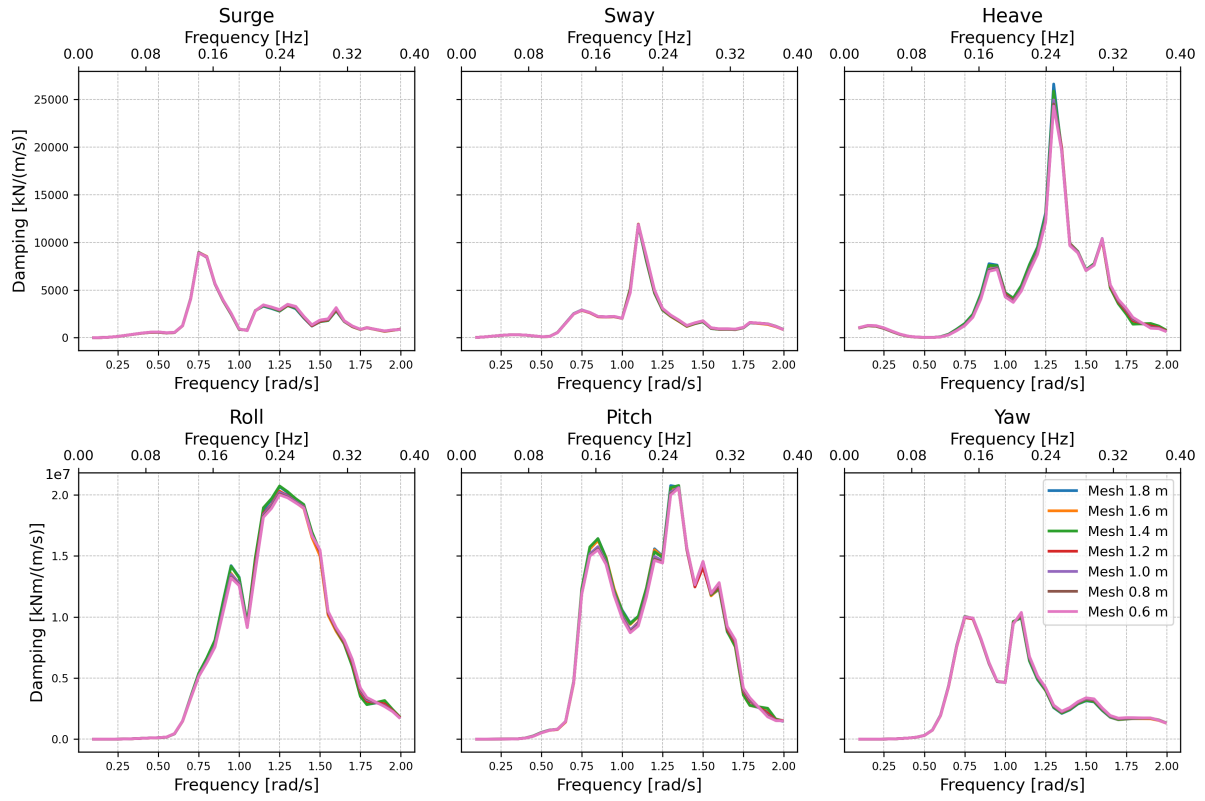


Figure B.4: Potential damping in six DOF for seven meshes

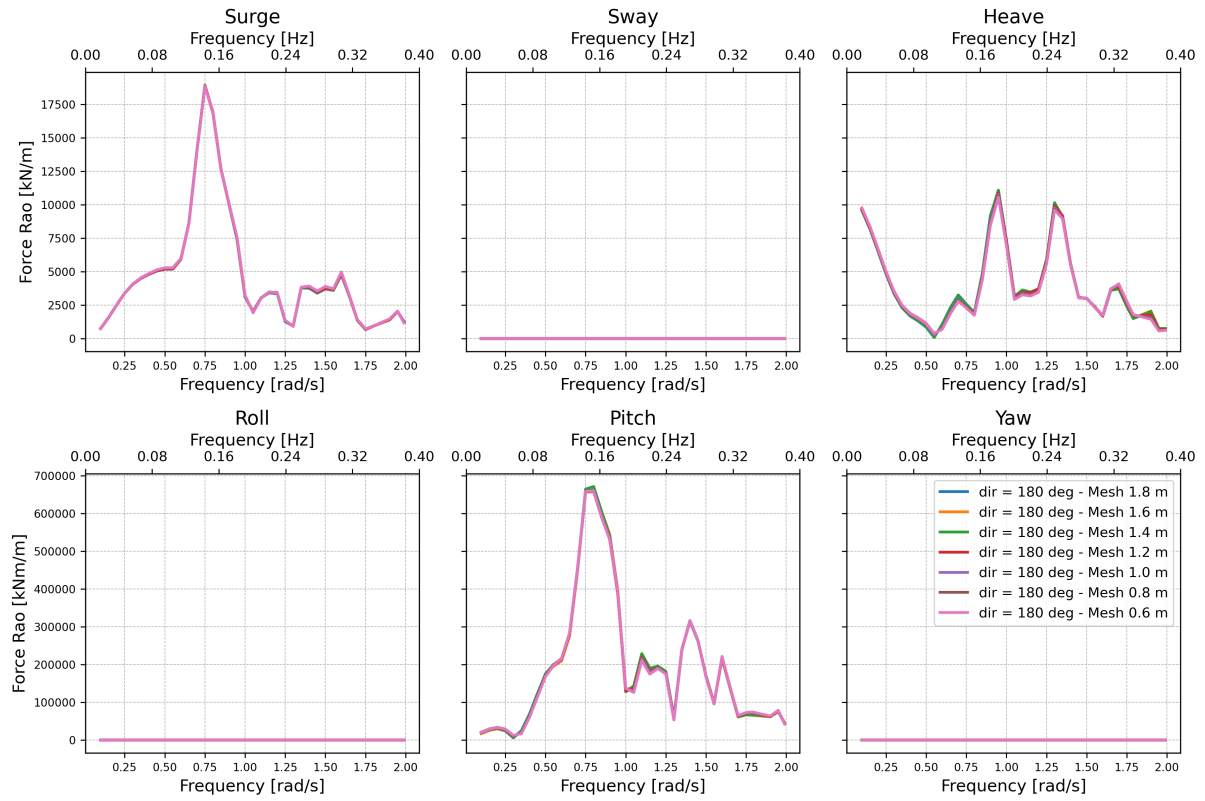
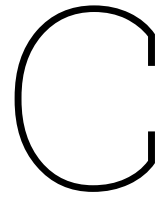


Figure B.5: Wave force RAO in six DOF for seven meshes



Heave Plate Experiments

For obtaining the non-dimensional damping, the experiments from two studies have been used. Zhang et al. (2023) and Wadhwa and K. P. Thiagarajan (2009). The experiments done by Zhang et al. (2023) are based on the Froude scaled WindFloat semi-submersible FOWT foundation. This foundation consists of three columns that are connected by braces. The scaled model represents the oscillation amplitudes and frequencies that are presented in table C.1.

Table C.1: Oscillation amplitudes and frequencies used in experiments

Amplitude (m)	Frequency (rad/s)	Period (s)
0.63, 1.26, 1.89, 2.52, 3.15, 3.77	0.32, 0.40, 0.53, 0.79, 1.13	19.83, 15.86, 11.90, 7.93, 5.55

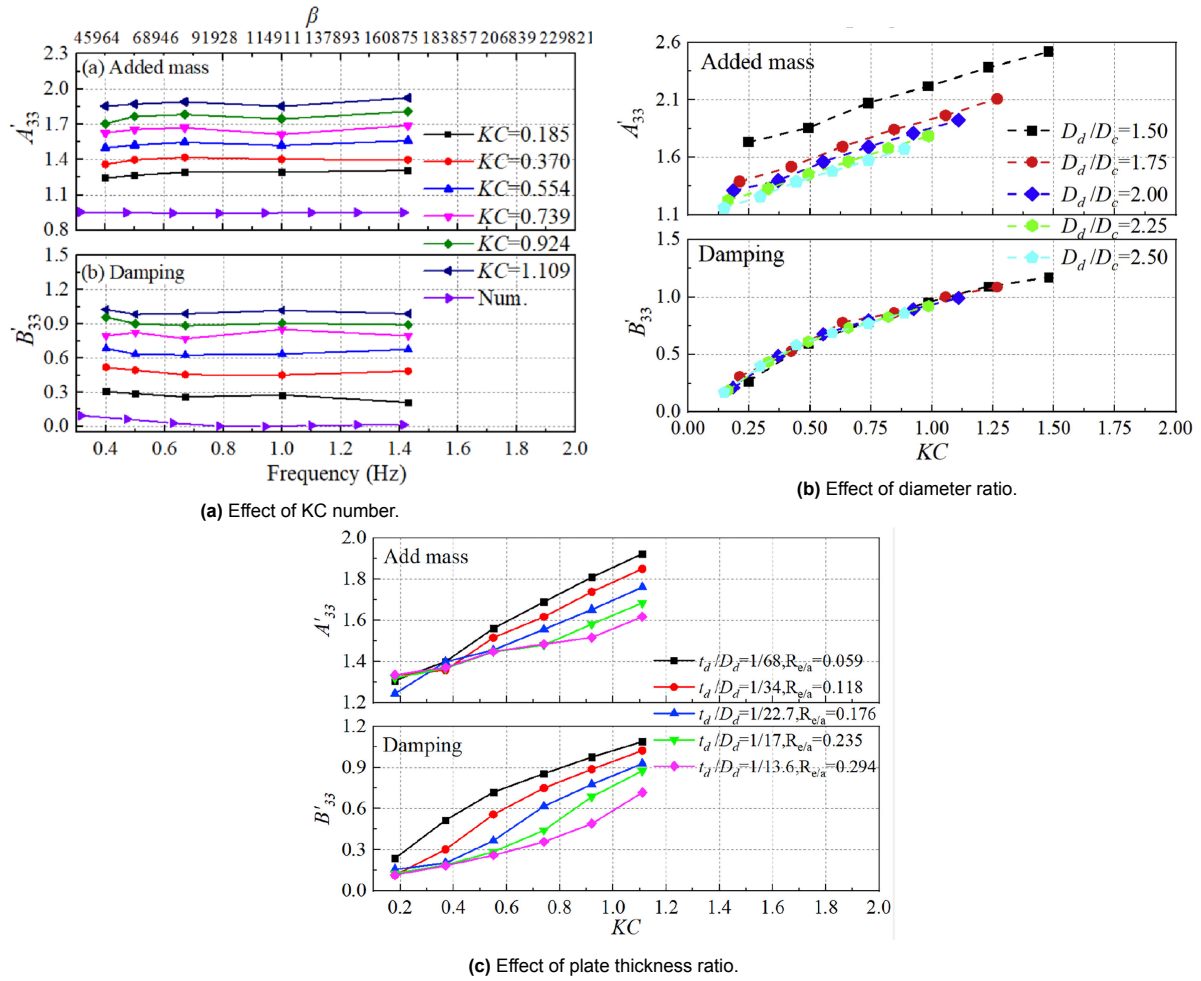


Figure C.1: Variation of non-dimensional added mass and damping for different KC numbers, diameter ratios, and thickness ratios.

Source: Zhang et al. 2023

The effect of heave plates near the free surface is studied by Wadhwa and K. P. Thiagarajan. The experimental results are expressed as submergence-plate radius ratio (S/a), and can be seen in figure C.2. Here, the deeply submerged plate is represented by the $S/2.0$ line, which indicates that the submergence is twice the heave plate radius. This value is compared to different shallow submergence levels. It can be noted that the damping increases for shallower submergence.

Figure C.3 shows the effect of submergence on the non-dimensional added mass. The dotted line connects the critical KC numbers for varying submergence levels, where the linear trend is broken. Beyond this line is the behaviour unclear, and the results could be incorrect (Wadhwa and K. P. Thiagarajan 2009).

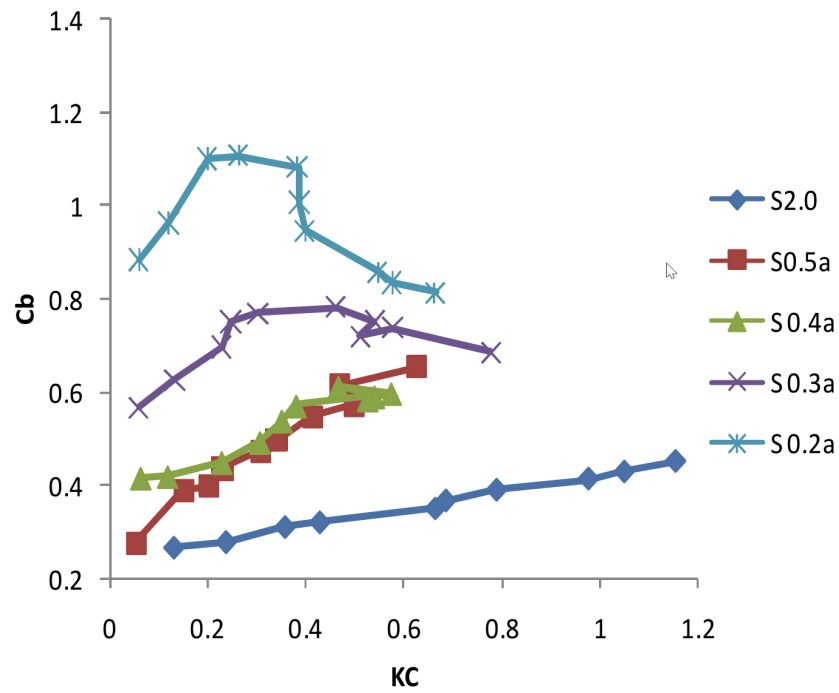


Figure C.2: Plate submergence effect on non-dimensional damping C_b .

Source: Wadhwa and K. P. Thiagarajan 2009

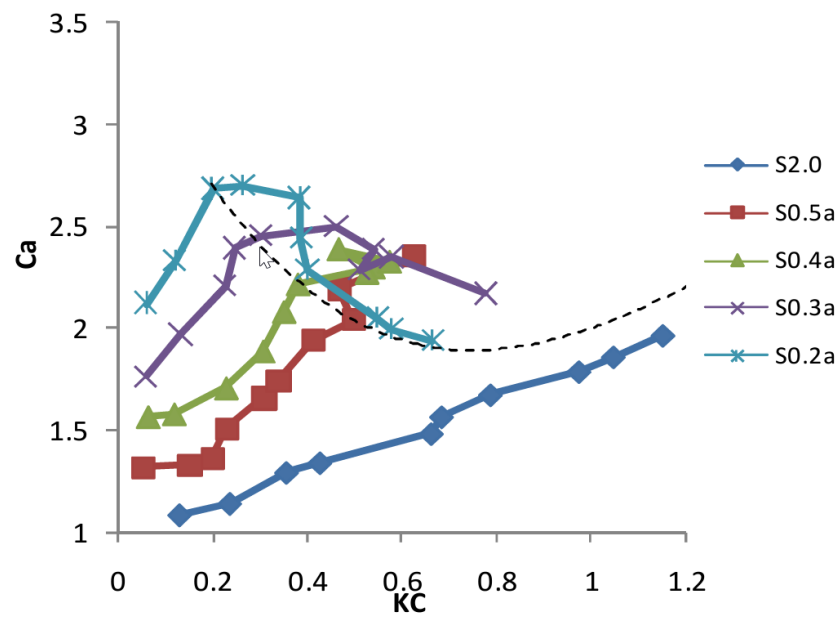


Figure C.3: Plate submergence effect on non-dimensional added mass C_a .

Source: Wadhwa and K. P. Thiagarajan 2009

D

Blade Properties

Here are the blade properties presented as well as the drag coefficients for cones.

Table D.1: Airfoils with drag coefficient along blade span.

Source: Github 2024

Spanwise position [r/R]	Airfoil name	C_d 90° [-]
0.000	circular	0.350
0.020	circular	0.350
0.150	SNL-FFA-W3-500	1.271
0.245	FFA-W3-360	1.300
0.329	FFA-W3-330blend	1.300
0.439	FFA-W3-301	1.300
0.538	FFA-W3-270blend	1.400
0.638	FFA-W3-241	1.500
0.772	FFA-W3-211	1.500
1.000	FFA-W3-211	1.500

Table D.2: Blade dimensions and drag coefficients along blade span.

Source: Github 2024

Position [r/R]	Chord [m]	Twist [rad]	Span [m]	Prebend [m]	C_d 90°	A [m ²]	$C_d A$ [m ²]
0.000	5.200	0.272	0.000	0.000	0.350	0.000	0.000
0.020	5.209	0.272	2.388	-0.018	0.350	12.427	4.349
0.041	5.238	0.269	4.776	-0.042	0.503	12.472	6.279
0.061	5.293	0.261	7.163	-0.071	0.657	12.573	8.259
0.082	5.367	0.249	9.551	-0.104	0.810	12.728	10.314
0.102	5.452	0.234	11.939	-0.137	0.964	12.917	12.449
0.122	5.540	0.217	14.327	-0.169	1.117	13.123	14.662
0.143	5.622	0.199	16.714	-0.199	1.271	13.326	16.933
0.163	5.693	0.181	19.102	-0.223	1.277	13.508	17.244
0.184	5.743	0.164	21.490	-0.241	1.282	13.652	17.508
0.204	5.765	0.149	23.878	-0.249	1.288	13.738	17.699
0.224	5.756	0.137	26.265	-0.250	1.294	13.755	17.800
0.245	5.703	0.126	28.653	-0.249	1.300	13.681	17.785
0.265	5.605	0.114	31.041	-0.248	1.300	13.500	17.550
0.286	5.472	0.104	33.429	-0.245	1.300	13.224	17.191
0.306	5.323	0.093	35.816	-0.241	1.300	12.887	16.753
0.327	5.166	0.084	38.204	-0.237	1.300	12.523	16.280
0.347	5.019	0.075	40.592	-0.232	1.300	12.161	15.809
0.367	4.886	0.067	42.980	-0.225	1.300	11.826	15.373
0.388	4.768	0.060	45.367	-0.211	1.300	11.525	14.983
0.408	4.655	0.054	47.755	-0.186	1.300	11.249	14.624
0.429	4.541	0.048	50.143	-0.148	1.300	10.978	14.272
0.449	4.428	0.042	52.531	-0.098	1.320	10.708	14.135
0.469	4.317	0.037	54.918	-0.041	1.340	10.441	13.990
0.490	4.208	0.032	57.306	0.022	1.360	10.178	13.842
0.510	4.102	0.027	59.694	0.089	1.380	9.921	13.690
0.531	3.999	0.023	62.082	0.159	1.400	9.671	13.539
0.551	3.899	0.019	64.469	0.241	1.420	9.429	13.390
0.571	3.803	0.015	66.857	0.337	1.440	9.196	13.242
0.592	3.709	0.011	69.245	0.447	1.460	8.969	13.095
0.612	3.617	0.008	71.633	0.568	1.480	8.747	12.945
0.633	3.526	0.004	74.020	0.698	1.500	8.528	12.791
0.653	3.434	0.001	76.408	0.832	1.500	8.309	12.464
0.673	3.342	-0.003	78.796	0.970	1.500	8.090	12.135
0.694	3.249	-0.007	81.184	1.109	1.500	7.868	11.803
0.714	3.156	-0.012	83.571	1.255	1.500	7.647	11.470
0.735	3.065	-0.017	85.959	1.410	1.500	7.427	11.140
0.755	2.973	-0.023	88.347	1.573	1.500	7.208	10.812
0.776	2.881	-0.028	90.735	1.743	1.500	6.989	10.483
0.796	2.787	-0.033	93.122	1.919	1.500	6.767	10.150
0.816	2.691	-0.036	95.510	2.100	1.500	6.540	9.810
0.837	2.592	-0.038	97.898	2.286	1.500	6.307	9.461
0.857	2.489	-0.038	100.286	2.476	1.500	6.066	9.100
0.878	2.384	-0.038	102.673	2.673	1.500	5.818	8.727
0.898	2.276	-0.037	105.061	2.878	1.500	5.563	8.345
0.918	2.165	-0.035	107.449	3.090	1.500	5.302	7.954
0.939	2.053	-0.033	109.837	3.308	1.500	5.036	7.554
0.959	1.938	-0.030	112.224	3.534	1.500	4.764	7.146
0.980	1.820	-0.026	114.612	3.764	1.500	4.486	6.729
0.985	1.780	-0.025	115.245	3.826	1.500	1.139	1.708
0.990	1.708	-0.024	115.830	3.884	1.500	1.020	1.530
0.995	1.472	-0.023	116.415	3.942	1.500	0.930	1.395
1.000	0.500	-0.022	117.000	4.000	1.500	0.577	0.865
Total					1.277	477.413	609.557

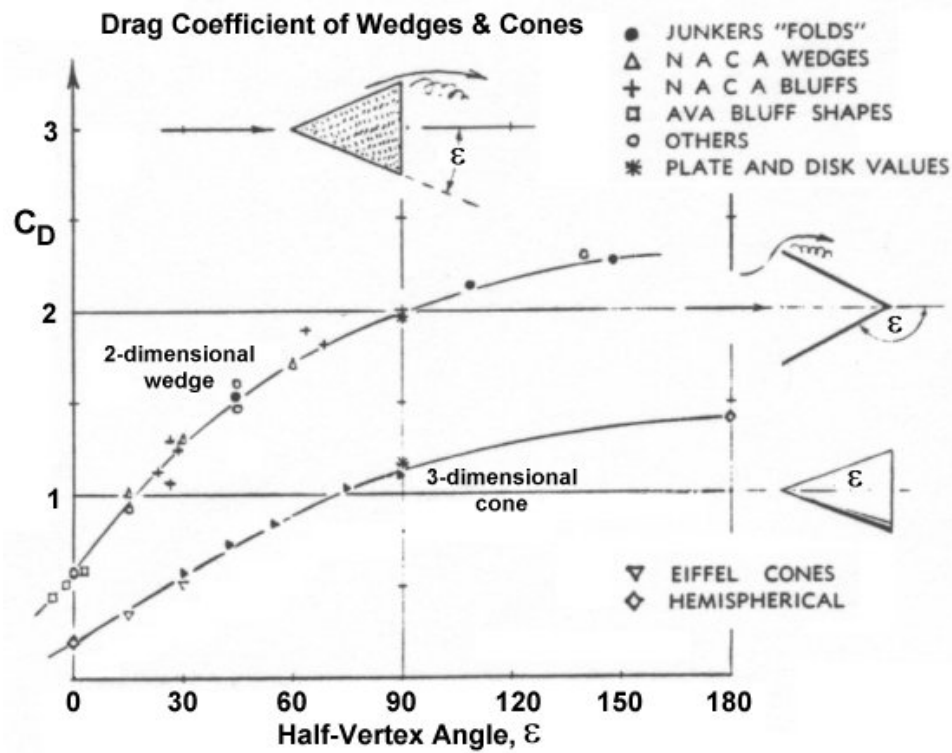
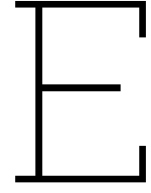


Figure D.1: Drag coefficient of wedges and cones vs. half-vertex angle

Source: Aerospaceweb 2024



Blade Equations Of Motion

The derivation of the blade EOM is given in this section.

Aerodynamic load:

$$F_w = \frac{1}{2} \rho_{\text{air}} C_d A V_w'(t)^2 \quad (\text{E.1})$$

Where V_w' is the relative wind speed with respect to the blade.

$$V_w'(t) = \overline{V_w} + V_w(t) - \dot{x}_b \quad (\text{E.2})$$

where $\overline{V_w}$ is the mean wind speed, $V_w(t)$ is the fluctuating wind speed, and \dot{x}_b is the blade velocity in x direction.

The aerodynamic force can be split into an excitation and damping force.

$$F_w = F_w^e - F_w^d = \frac{1}{2} \rho_{\text{air}} C_d A \overline{V_w}^2 + \rho_{\text{air}} C_d A \overline{V_w} V_w - \rho_{\text{air}} C_d A \overline{V_w} \dot{x}_b \quad (\text{E.3})$$

The first term is the mean force, the second term is the fluctuating force and the third term is the damping term due to the blade's velocity.

Lagrange method:

$$\frac{\partial}{\partial t} \left(\frac{\partial T(\theta)}{\partial \dot{\theta}} \right) - \frac{\partial T(\theta)}{\partial \theta} + \frac{\partial R(\theta)}{\partial \dot{\theta}} + \frac{\partial U(\theta)}{\partial \theta} = Q \quad (\text{E.4})$$

position vector of blade:

$$\vec{p}_b = l_c \left(\sin \theta \vec{\mathbf{i}} + (1 - \cos \theta) \vec{\mathbf{k}} \right) \quad (\text{E.5})$$

$$\dot{\vec{p}}_b = l_c \left(\dot{\theta} \cos \theta \vec{\mathbf{i}} + \dot{\theta} \sin \theta \vec{\mathbf{k}} \right) \quad (\text{E.6})$$

System energies have to be defined for the Lagrange method.

Kinetic energy:

$$T = \frac{1}{2} m \dot{p}^2 = \frac{1}{2} m (l_c \dot{\theta})^2 \quad (\text{E.7})$$

$$\frac{\partial}{\partial t} \left(\frac{\partial T(\theta)}{\partial \dot{\theta}} \right) = ml_c^2 \ddot{\theta} \quad (\text{E.8})$$

$$\frac{\partial T(\theta)}{\partial \theta} = 0 \quad (\text{E.9})$$

Dissipation energy due to aerodynamic damping and tagline damping: Substitute $\dot{x}_b = l_c \dot{\theta} \cos \theta$

$$R = R_a + R_t = \frac{1}{2} \rho_{\text{air}} C_d A \overline{V_w} (l_c \dot{\theta} \cos \theta)^2 + \frac{1}{2} C_t (l_c \dot{\theta} \cos \theta)^2 \quad (\text{E.10})$$

$$\frac{\partial R(\theta)}{\partial \dot{\theta}} = \rho_{\text{air}} C_d A \overline{V_w} \dot{\theta} (l_c \cos \theta)^2 + C_t \dot{\theta} (l_c \cos \theta)^2 = (\rho_{\text{air}} C_d A \overline{V_w} + C_t) \dot{\theta} (l_c \cos \theta)^2 \quad (\text{E.11})$$

Potential energy can be split in gravitational potential energy and elastic energy from the taglines.

$$U_{\text{tot}} = U_g + U_t = mgl_c - mgl_c \cos \theta + \frac{1}{2} K_t l_c^2 \sin^2 \theta \quad (\text{E.12})$$

$$\frac{\partial U(\theta)}{\partial \theta} = mgl_c \sin \theta + K_t l_c^2 \sin \theta \cos \theta \quad (\text{E.13})$$

External loading:

$$Q = \rho_{\text{air}} C_d A \overline{V_w} V_w l_c \quad (\text{E.14})$$

Under the small angle assumption $\cos \theta \approx 1$ and $\sin \theta \approx \theta$, all the terms can be substituted and the expression simplified:

$$ml_c^2 \ddot{\theta} + (\rho_{\text{air}} C_d A \overline{V_w} + C_t) \dot{\theta} l_c^2 + l_c \theta (mg + K_t l_c) = \rho_{\text{air}} C_d A \overline{V_w} V_w l_c \quad (\text{E.15})$$

Convert to frequency domain:

$$\theta = X(i\omega) e^{i\omega t} \quad (\text{E.16})$$

$$\dot{\theta} = i\omega X(i\omega) e^{i\omega t} \quad (\text{E.17})$$

$$\ddot{\theta} = -\omega^2 X(i\omega) e^{i\omega t} \quad (\text{E.18})$$

Substitute in the original equation:

$$\begin{aligned} ml_c^2 (-\omega^2 X(i\omega) e^{i\omega t}) + (\rho_{\text{air}} C_d A \overline{V_w} + C_t) (i\omega X(i\omega) e^{i\omega t}) l_c^2 + l_c (X(i\omega) e^{i\omega t}) (mg + K_t l_c) = \\ = \rho_{\text{air}} C_d A l_c \overline{V_w} V_w e^{i\omega t} \end{aligned} \quad (\text{E.19})$$

Factor out the $e^{i\omega t}$ term:

$$-ml_c^2 \omega^2 X(i\omega) + i\omega X(i\omega) l_c^2 (\rho_{\text{air}} C_d A \overline{V_w} + C_t) + X(i\omega) l_c (mg + K_t l_c) = \rho_{\text{air}} C_d A l_c \overline{V_w} V_w \quad (\text{E.20})$$

Rearranging to collect all terms that involve $X(i\omega)$, and factor it out:

$$X(i\omega) (-ml_c^2\omega^2 + i\omega l_c^2(\rho_{\text{air}}C_d A \overline{V_w} + C_t) + l_c(mg + K_t l_c)) = \rho_{\text{air}}C_d A l_c \overline{V_w} V_w \quad (\text{E.21})$$

The undamped natural frequency ω_n can be obtained by solving the homogeneous equation with zero damping:

$$-ml_c^2\omega^2 + l_c(mg + K_t l_c) = 0 \quad (\text{E.22})$$

$$\omega_n = \sqrt{\frac{mg + K_t l_c}{ml_c}} \quad (\text{E.23})$$

F

Results

This appendix shows the relevant figures to complement the results in the main report. It contains results for the blade motions, floater motions, and relative motions.

F.1. Suspension Length

Figure F.1 shows the sensitivity of the blade motions in axial direction due to changing the blade's suspension length.

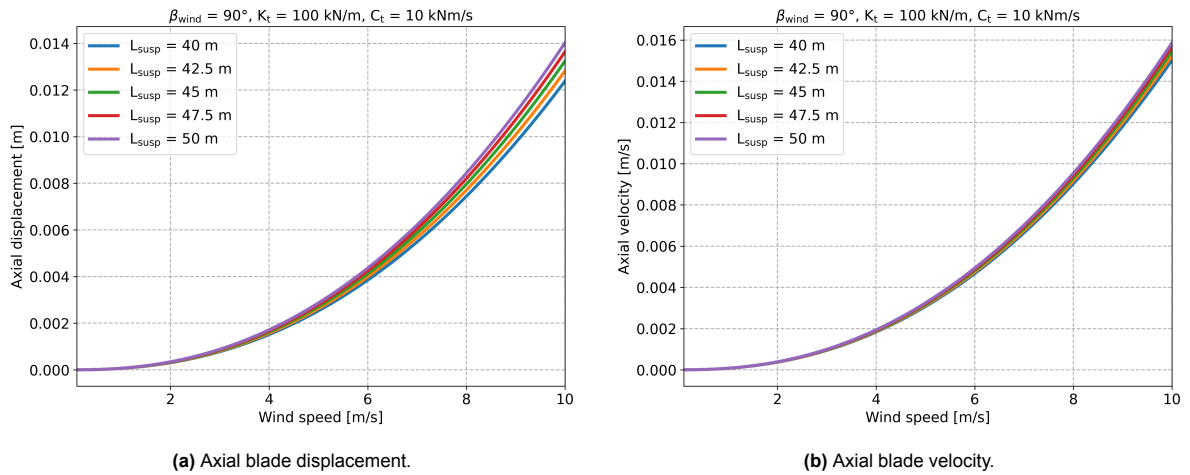


Figure F.1: Effect of the suspension length on the axial displacement and velocity for different wind speeds.

F.2. Tagline Diameter

Figure F.1 shows the sensitivity of the blade motions in axial direction due to changing the tagline diameter.

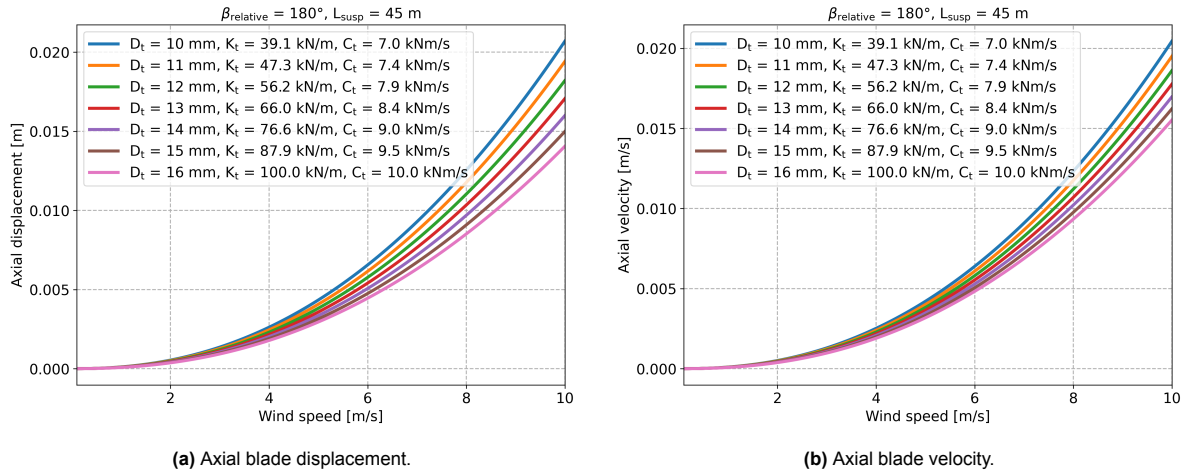


Figure F.2: Effect of the tagline stiffness on the axial displacement and velocity for different wind speeds.

F.3. Blade Orientation

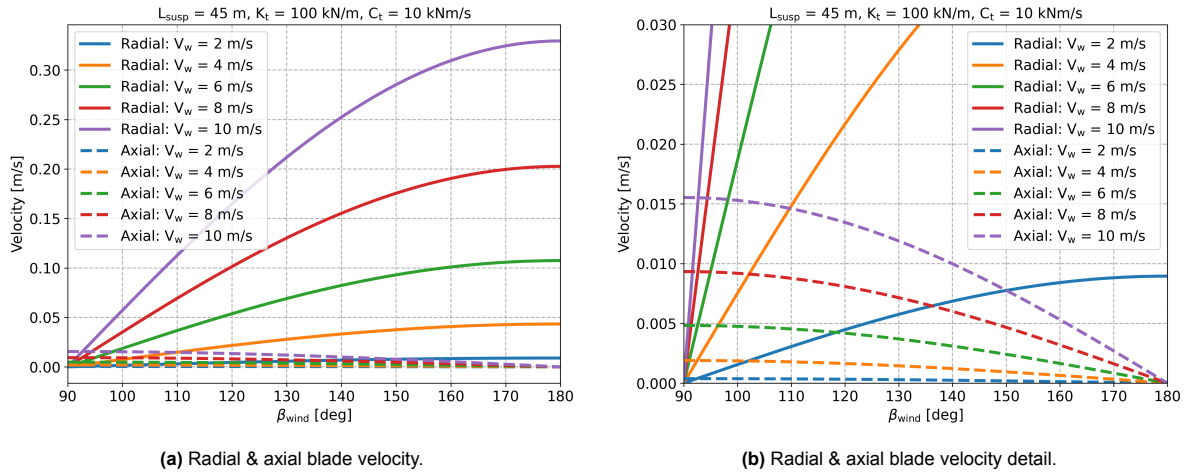


Figure F.3: Effect of the blade orientation with respect to the wind on the velocity for different wind speeds.

F.4. Quayside Distance

Figure F.4 shows the displacement RAOs in roll, pitch, and yaw, at the COG for five different quayside distances within the feasible distance range for installation. A wave direction of 135° is considered.

Displacement RAOs

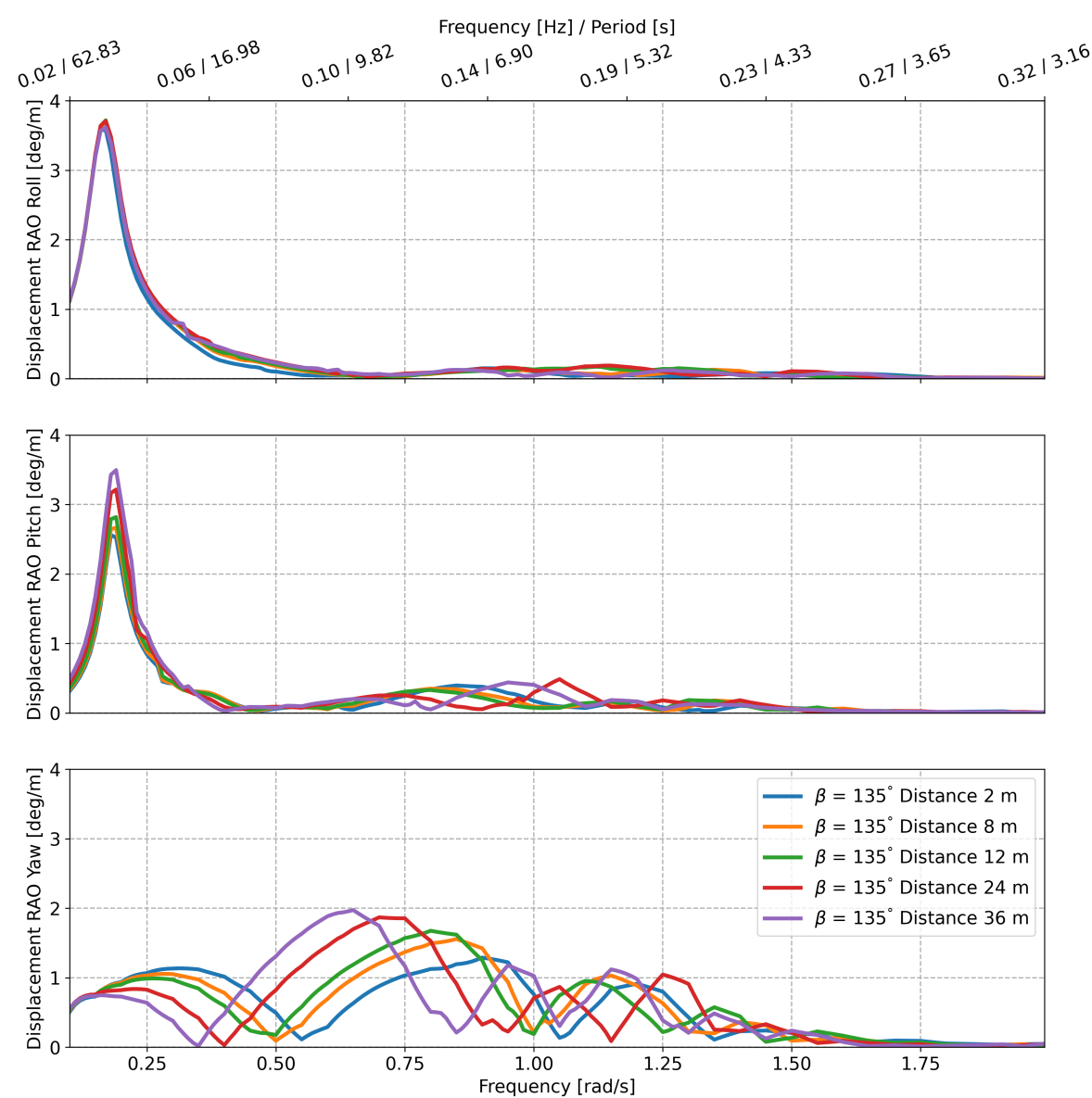


Figure F.4: Quayside distance dependent displacement RAOs for roll, pitch, and yaw.

Figures F.5 and F.6 show the characteristic radial and axial velocity for different quayside distances.

Characteristic Velocity

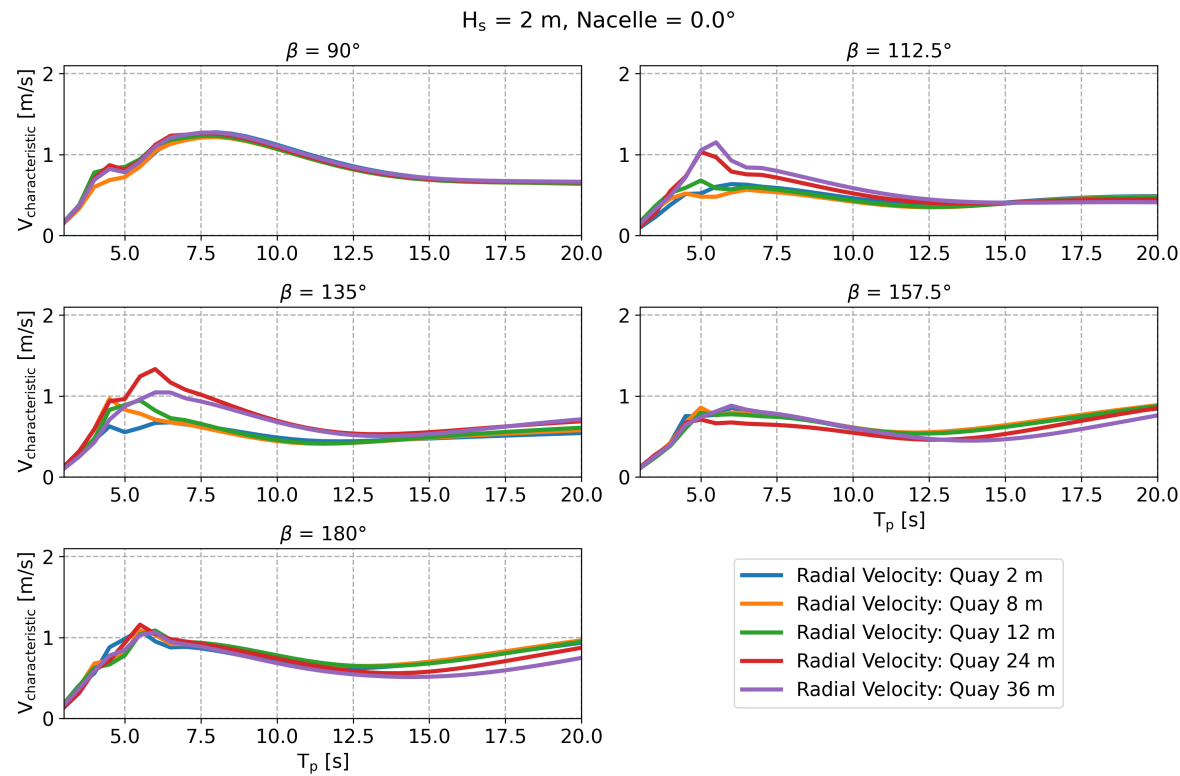


Figure F.5: Characteristic radial velocity for multiple quayside distances and wave directions.

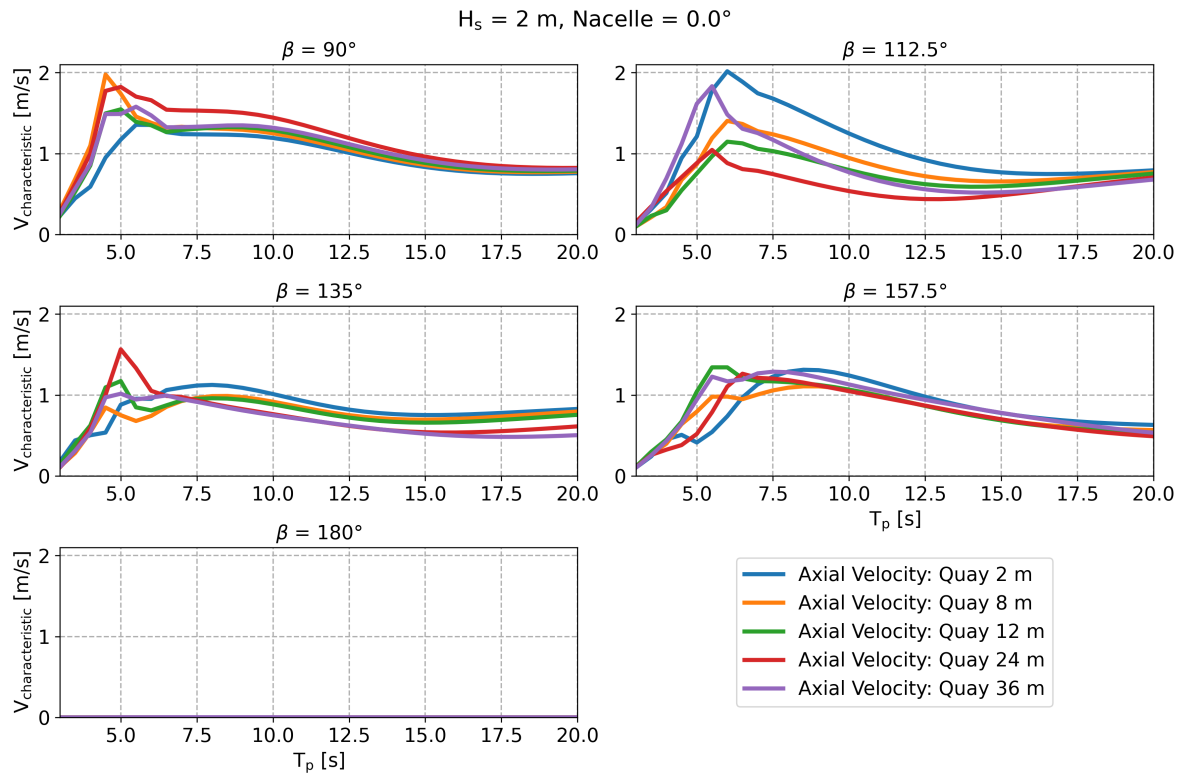


Figure F.6: Characteristic axial velocity for multiple quayside distances and wave directions.

Quayside Distance Sensitive Allowable H_s

Figure F.7 shows the allowable H_s against the peak period for different wave directions and quayside distances.

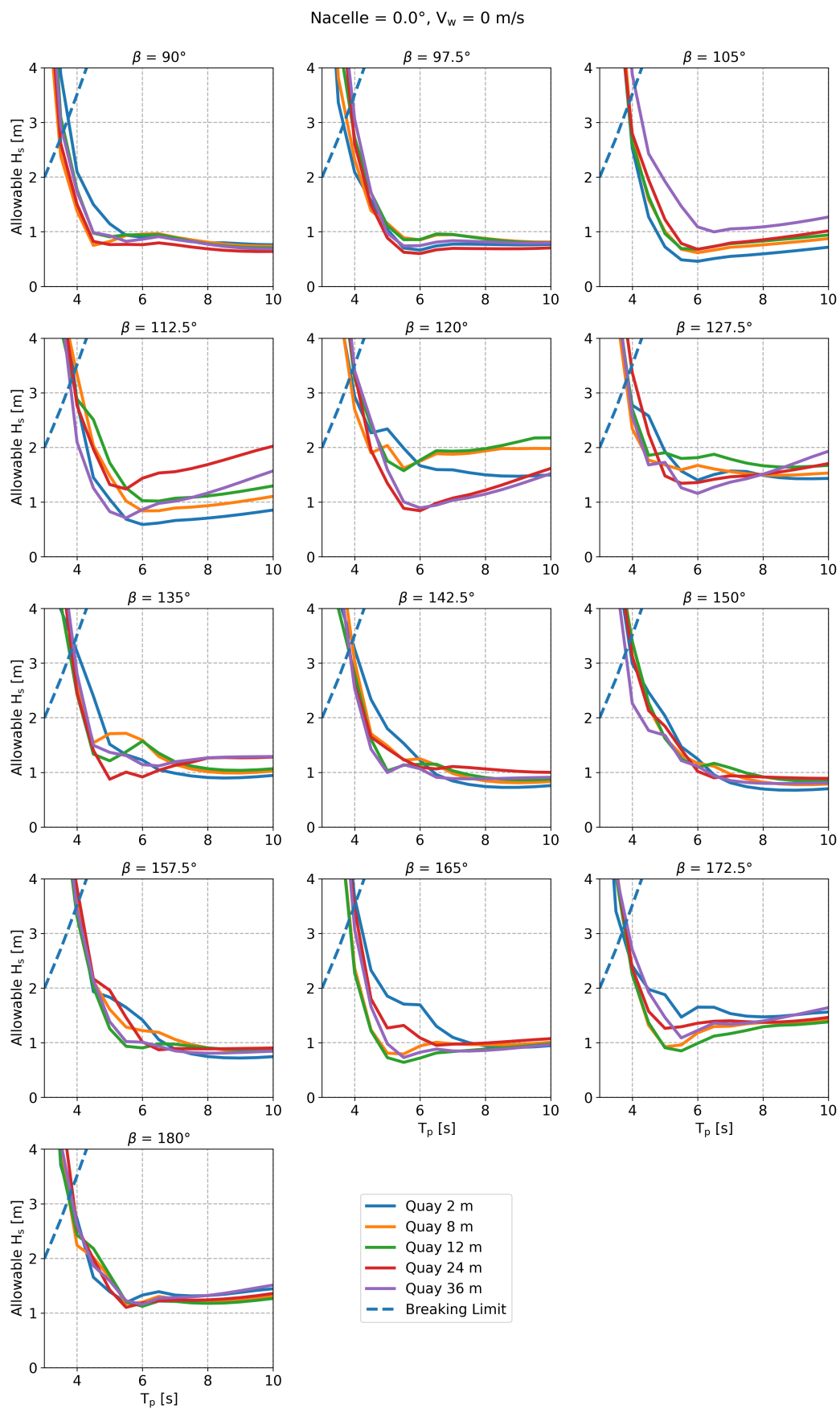


Figure F.7: Allowable H_s vs. peak period for multiple quayside distances and wave directions.

F.5. Limiting Floater Motions

Figure F.8 shows the allowable H_s for each motion during the alignment and mating phases for thirteen wave directions.

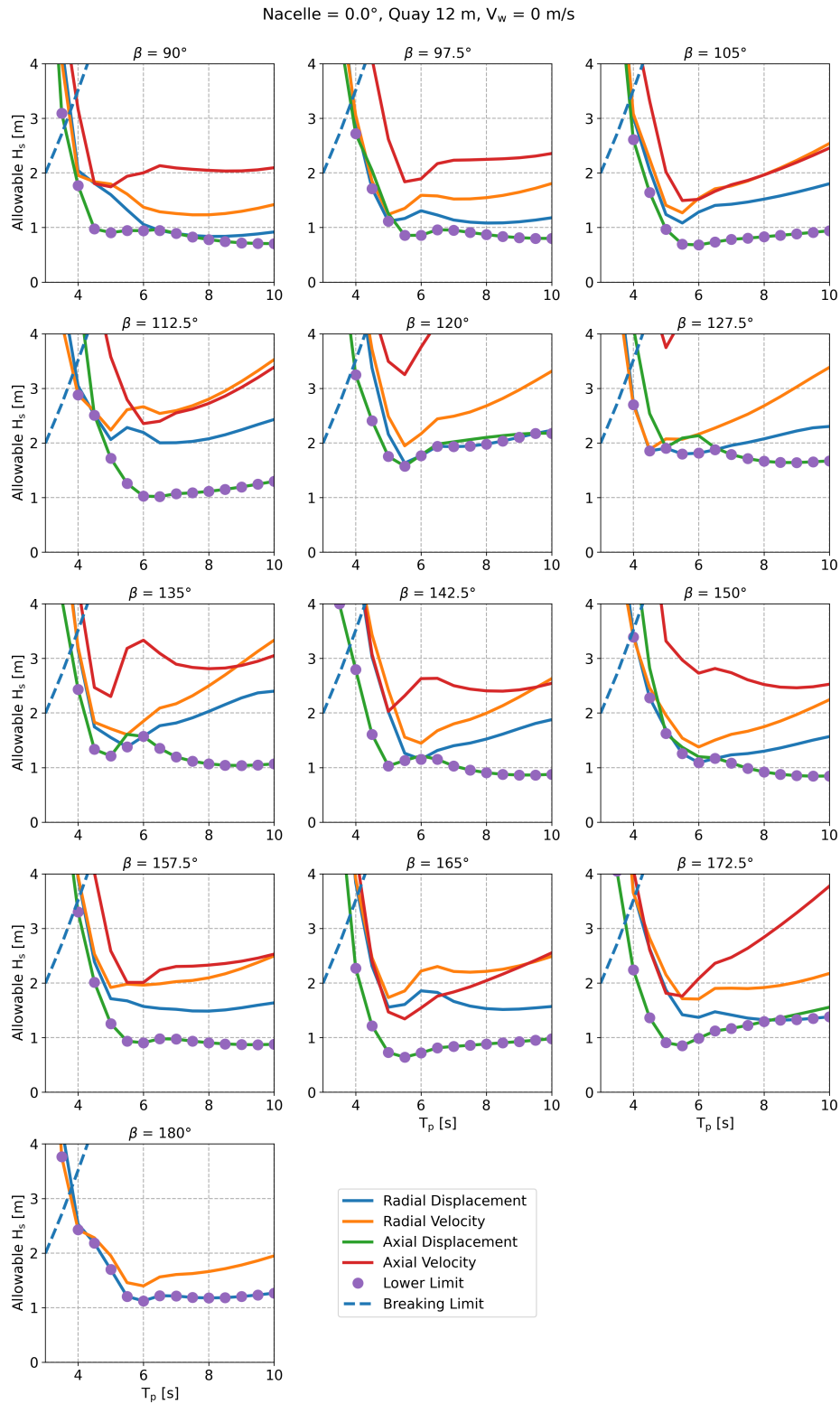


Figure F.8: Limiting floater motions for thirteen different wave directions and peak periods.

F.6. Nacelle Rotation

Figures F.9 and F.10 show the allowable H_s against the relative nacelle heading for a low ($V_w = 2$ m/s) and high wind speed ($V_w = 8$ m/s). Wind/wave directions between $\beta = 180^\circ$ and $\beta = 270^\circ$ are considered for peak periods between 5 and 10 seconds.

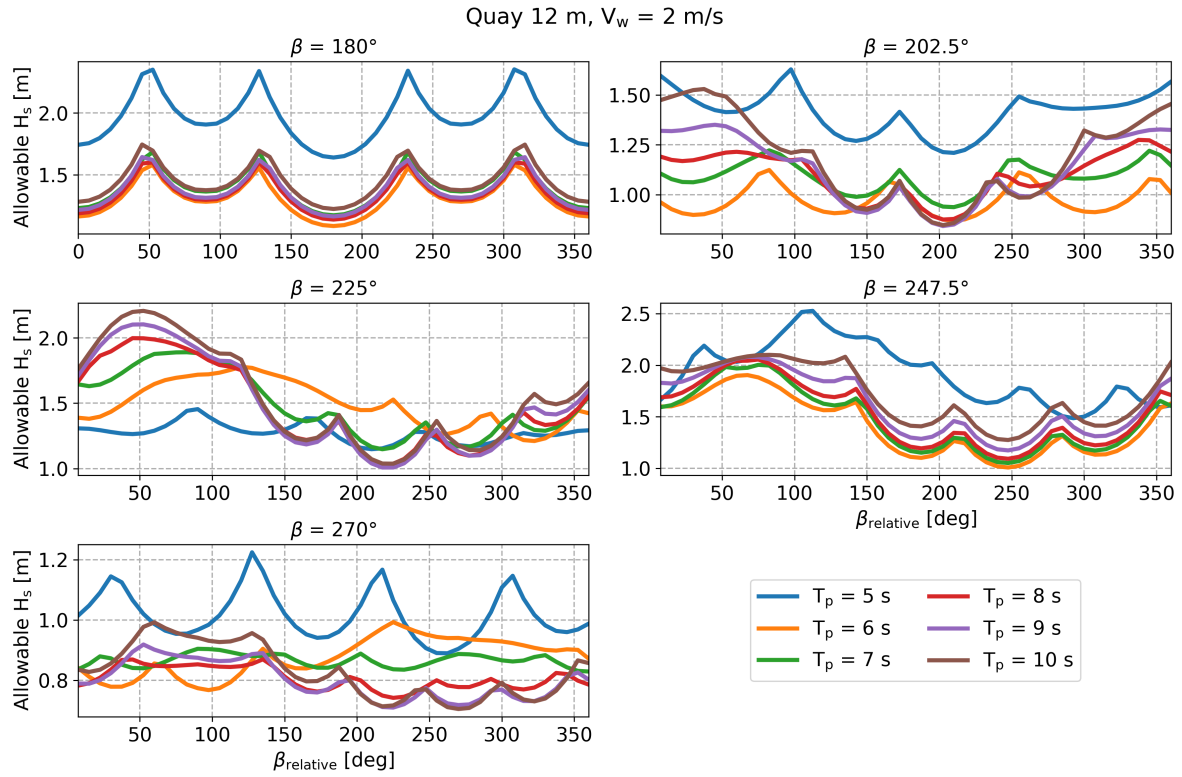


Figure F.9: Relative nacelle heading dependent allowable H_s for different T_s and environmental directions at $V_w = 2$ m/s.

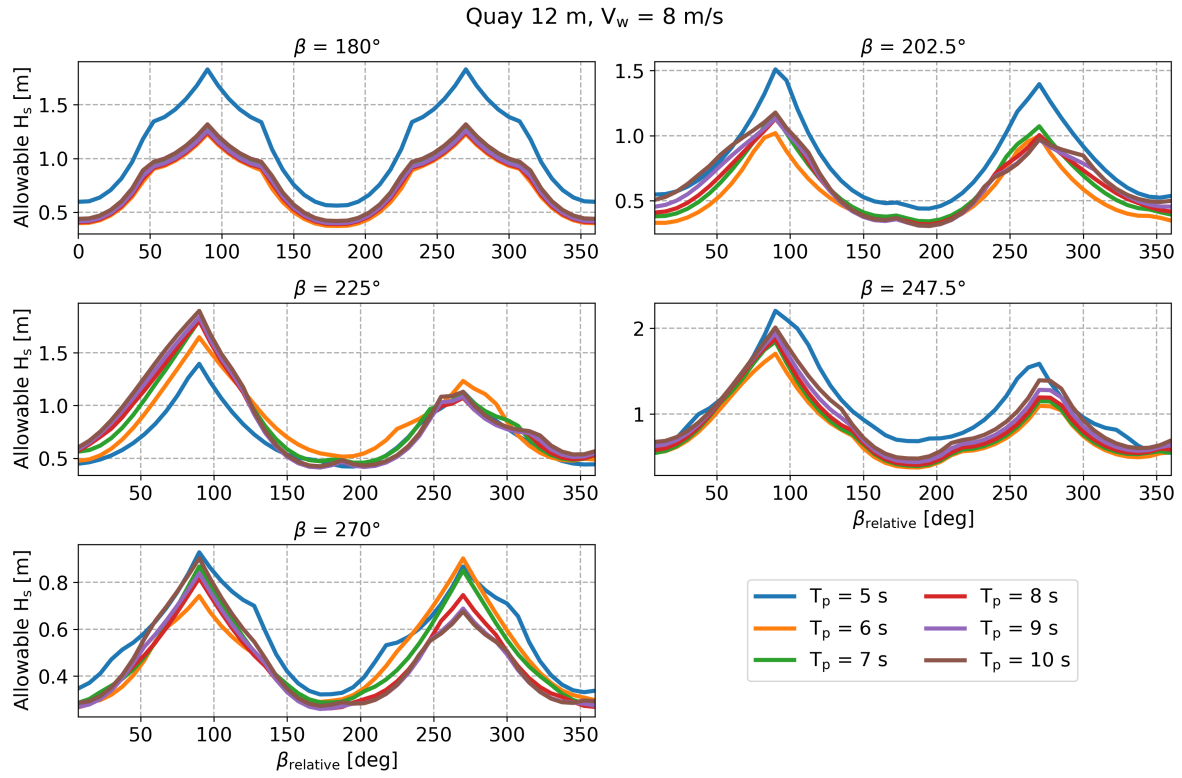


Figure F.10: Relative nacelle heading dependent allowable H_s for different T_p and environmental directions at $V_w = 8$ m/s.

Figure F.11 shows the optimal relative nacelle heading on the vertical axis against the peak period for multiple wind speeds. Multiple wind/wave directions between $\beta = 90^\circ$ and $\beta = 270^\circ$ are considered.

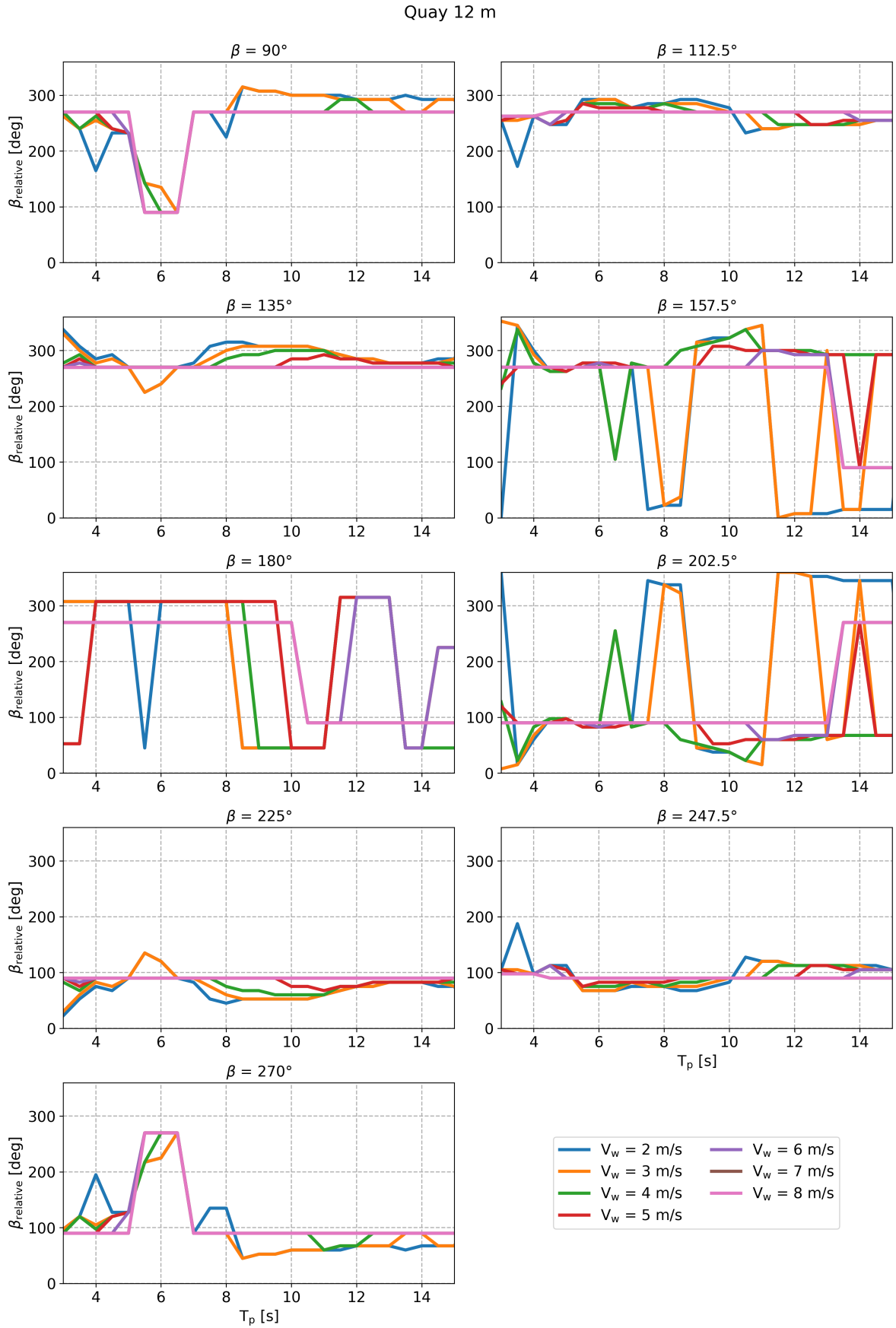


Figure F.11: Optimal nacelle heading vs. T_p for different wind speeds and directions.